

Regulation of presynaptic Ca²⁺ channel abundance at active zones through a balance of delivery and turnover

Karen L Cunningham, Chad W Sauvola, Sara Tavana, J Troy Littleton*

The Picower Institute for Learning and Memory, Department of Biology, Department of Brain and Cognitive Sciences, Massachusetts Institute of Technology, Cambridge, United States

Abstract Voltage-gated Ca²⁺ channels (VGCCs) mediate Ca²⁺ influx to trigger neurotransmitter release at specialized presynaptic sites termed active zones (AZs). The abundance of VGCCs at AZs regulates neurotransmitter release probability (*Pr*), a key presynaptic determinant of synaptic strength. Although biosynthesis, delivery, and recycling cooperate to establish AZ VGCC abundance, experimentally isolating these distinct regulatory processes has been difficult. Here, we describe how the AZ levels of cacophony (*Cac*), the sole VGCC-mediating synaptic transmission in *Drosophila*, are determined. We also analyzed the relationship between *Cac*, the conserved VGCC regulatory subunit $\alpha 2\delta$, and the core AZ scaffold protein Bruchpilot (BRP) in establishing a functional AZ. We find that *Cac* and BRP are independently regulated at growing AZs, as *Cac* is dispensable for AZ formation and structural maturation, and BRP abundance is not limiting for *Cac* accumulation. Additionally, AZs stop accumulating *Cac* after an initial growth phase, whereas BRP levels continue to increase given extended developmental time. AZ *Cac* is also buffered against moderate increases or decreases in biosynthesis, whereas BRP lacks this buffering. To probe mechanisms that determine AZ *Cac* abundance, intravital FRAP and *Cac* photoconversion were used to separately measure delivery and turnover at individual AZs over a multi-day period. *Cac* delivery occurs broadly across the AZ population, correlates with AZ size, and is rate-limited by $\alpha 2\delta$. Although *Cac* does not undergo significant lateral transfer between neighboring AZs over the course of development, *Cac* removal from AZs does occur and is promoted by new *Cac* delivery, generating a cap on *Cac* accumulation at mature AZs. Together, these findings reveal how *Cac* biosynthesis, synaptic delivery, and recycling set the abundance of VGCCs at individual AZs throughout synapse development and maintenance.

*For correspondence:
troy@mit.edu

Competing interest: The authors declare that no competing interests exist.

Funding: See page 24

Received: 15 March 2022

Preprinted: 16 March 2022

Accepted: 13 July 2022

Published: 14 July 2022

Reviewing Editor: P Robin Hiesinger, Institute for Biology Free University Berlin, Germany

© Copyright Cunningham et al. This article is distributed under the terms of the [Creative Commons Attribution License](https://creativecommons.org/licenses/by/4.0/), which permits unrestricted use and redistribution provided that the original author and source are credited.

Editor's evaluation

This paper will be of interest to a broad range of neurophysiologists as it provides insights into the regulation of presynaptic voltage-gated calcium channel abundance which largely determines presynaptic strength. The findings demonstrate that while VGCC biosynthesis does not play a major role in regulating VGCC abundance at AZs, both trafficking and recycling at active zones are important regulatory steps.

Introduction

Voltage-gated Ca²⁺ channels (VGCCs) convert electrical signals to chemical signals (Ca²⁺ influx) at the presynaptic membrane to trigger synaptic vesicle (SV) release. VGCCs are located at presynaptic active zones (AZs), specialized lipid and protein domains that cluster SVs near VGCCs and in apposition to postsynaptic neurotransmitter receptors (*Catterall and Few, 2008; Bucurenciu et al., 2008;*

Eggermann et al., 2011; Fouquet et al., 2009; Kawasaki et al., 2004; Wang et al., 2008; Chen et al., 2015; Nakamura et al., 2015). The strength of a synaptic connection is steeply dependent on the level of presynaptic Ca^{2+} influx at AZs, highlighting that tight regulation of VGCCs is important for determining synaptic strength (**Augustine et al., 1985; Borst and Sakmann, 1996; Sheng et al., 2012**). Specifically, VGCC regulation controls neurotransmitter release probability (P_r ; the likelihood of SV fusion following an action potential), a fundamental presynaptic component of synaptic strength. P_r can vary dramatically between closely neighboring AZs, indicating local AZ mechanisms control P_r (**Atwood and Karunanithi, 2002; Branco and Staras, 2009; Melom et al., 2013; Peled and Isacoff, 2011; Ariel et al., 2012; Akbergenova et al., 2018; Newman et al., 2022**). The molecular composition of the AZ represents a convergence of pathways that govern protein biosynthesis, trafficking, incorporation, and recycling of VGCCs and AZ scaffold proteins (**Petzoldt et al., 2016**). Experimentally isolating how these separate levels of regulation contribute to VGCC and AZ scaffold abundance is important for understanding how P_r is established.

Multiple proteins are implicated in controlling VGCC abundance and function (**Kittel et al., 2006; Graf et al., 2012; Acuna et al., 2016; Zhang et al., 2016; Catterall and Few, 2008; Missler et al., 2003; Hoppa et al., 2012**). These regulatory pathways are of clinical importance, as disruptions in presynaptic Ca^{2+} influx are linked to several diseases including migraine and ataxia (**Cao and Tsien, 2005; Ophoff et al., 1996; Pietrobon and Striessnig, 2003; Zhuchenko et al., 1997; Luo et al., 2017; Brusich et al., 2018**). One conserved regulator of VGCC abundance at synapses is the $\alpha 2\delta$ subunit that contributes to channel trafficking and is pharmacologically targeted by the widely prescribed drugs gabapentin and pregabalin (**Dolphin, 2016; Dickman et al., 2008; Hoppa et al., 2012; Eroglu et al., 2009; Saheki and Bargmann, 2009; Cassidy et al., 2014; Schöpf et al., 2021**). Despite the importance of $\alpha 2\delta$ and other VGCC regulatory pathways, the dynamics of channel trafficking to and from the presynaptic membrane are largely unknown due to a lack of tools for experimentally parsing the contributions of delivery versus recycling. For example, experiments in which mutant channels appear to displace wildtype channels in competition for AZ localization have generated a model where VGCCs compete for AZ 'slots', but whether this capacity for VGCCs is regulated through limited delivery or protein turnover is unknown (**Cao et al., 2004**). Indeed, the resident time of VGCCs at the presynaptic AZ membrane, to what extent VGCCs are stabilized against inter-AZ lateral transfer, and how VGCC recycling and delivery rates contribute to the overall abundance of VGCCs at release sites has not been established.

The *Drosophila* neuromuscular junction (NMJ) is an attractive system to interrogate the dynamics of VGCCs in vivo as many core proteins and pathways are evolutionarily conserved, genetic toolkits are abundant, and individual AZs are resolvable using light microscopy (**Harris and Littleton, 2015**). Additionally, while mammals have seven high voltage-activated VGCCs and four $\alpha 2\delta$ family members, evoked synaptic transmission in *Drosophila* is mediated solely by the cacophony (Cac) $\alpha 1$ subunit, a Ca_v2 channel that requires only one $\alpha 2\delta$ subunit (straightjacket) for presynaptic localization and function (**Catterall and Few, 2008; Kawasaki et al., 2004; Ryglewski et al., 2012; Heinrich and Ryglewski, 2020; Ly et al., 2008**). The *Drosophila* larval stages span roughly 6 days, during which time AZs are continuously added to the NMJ. AZs mature over a multi-day period as Cac channels and AZ scaffolds like Bruchpilot (BRP) accumulate, generating a population of AZs at multiple stages of maturation (**Fouquet et al., 2009; Rasse et al., 2005; Akbergenova et al., 2018**). This developmental heterogeneity produces functional diversity. Optical P_r mapping reveals >40-fold variation in P_r across the AZ population of a single motoneuron, with each NMJ housing a small population of high releasing sites among a majority of low P_r AZs (**Melom et al., 2013; Akbergenova et al., 2018; Gratz et al., 2019; Newman et al., 2017; Peled et al., 2014; Peled and Isacoff, 2011; Newman et al., 2022**). P_r at individual AZs correlates well with Cac abundance, demonstrating AZ Cac levels tightly regulate presynaptic output (**Akbergenova et al., 2018; Gratz et al., 2019; Newman et al., 2022**).

Here, we probe the relationship between Cac and the AZ scaffold and characterize how biosynthesis, delivery, and turnover contribute to establishing Cac abundance at AZs of the *Drosophila* NMJ. We find that AZ abundance of Cac and BRP are regulated independently at growing AZs. The AZ scaffold forms and matures in the absence of Cac channels, and BRP scaffold abundance is not a limiting factor in AZ Cac accumulation. Additionally, Cac AZ abundance is regulated downstream of a surplus of biosynthesized channels, whereas BRP biosynthesis directly reflects synaptic BRP levels. To characterize how AZ Cac is regulated downstream of biosynthesis, we used photoconversion and

photobleaching experiments in intact animals to visualize Cac delivery and recycling. Cac delivery occurs at a majority of AZs over 24 hr, correlates highly with AZ size, and is rate-limited by $\alpha 2\delta$. Although Cac does not undergo detectable lateral transfer between neighboring AZs over the course of development, Cac recycling from the AZ membrane contributes significantly to regulating Cac AZ abundance, with new delivery driving channel turnover. Together, these data elucidate the behavior of bulk presynaptic VGCC flow across the AZ population of a single neuron.

Results

Ca^{2+} channels are not required for AZ scaffold formation

The AZ scaffold is required for proper clustering and accumulation of Cac channels at the *Drosophila* NMJ, as null mutants of AZ building blocks including BRP and RIM-binding protein (RBP) dramatically reduce AZ Cac abundance (Fouquet et al., 2009; Liu et al., 2011). Whether Cac channels are also required for efficient AZ scaffold formation is unclear due to the embryonic lethality of cac null mutants. The Flpstop conditional gene knockout approach allows single gene expression to be switched off in a cell-type specific manner by expressing a Flippase to reverse the genomic orientation of a 'Flp' construct residing in a gene of interest. A successful Flp event initiates sustained transcription of a cytosolic tdTomato reporter (Fisher et al., 2017). To circumvent cac embryonic lethality and determine whether AZs form and mature in cac null neurons in vivo, we expressed UAS-Flippase using a single-neuron GAL4 driver (MN1-lb-GAL4; expressed in the lb motoneuron innervating muscle 1) in animals carrying a Flpstop insertion in the cac locus (*cac^{flp}*). Because cac is on the X chromosome, the presence of the tdTomato reporter in the MN1-lb neuron of a male represents loss of the sole copy of cac from that neuron. To determine the timecourse of the flip event during development, we assayed the onset of expression of the tdTomato reporter. At the 1st instar stage, ~11 of the 14 (79%) MN1-lb motoneurons in abdominal segments A1-A7 had undergone a flip event at the cac locus, and by the 2nd instar stage 91% were tdTomato positive (Figure 1—figure supplement 1A, B). Given 3rd instar MN1-lb NMJs have fivefold more AZs than 2nd instar NMJs (Figure 1—figure supplement 1C, D), the majority of AZs present at the 3rd instar stage formed after the flip event occurred.

MN1-lb synapses were divided into four groups based on the presence or absence of a co-innervating ls motoneuron, and on the presence or absence of a successful Cac-flip event (Figure 1A). MN1-ls and MN1-lb identity was determined using HRP staining to mark neuronal membranes, and Cac-flip events were reported by tdTomato fluorescence. Two-electrode voltage-clamp (TEVC) recordings from muscle 1 demonstrated a dramatic reduction in EJC amplitude following stimulation in neurons that underwent a successful Cac-flip event, reflecting reduction in Cac abundance at the synaptic terminal. In lb/ls co-innervated muscles, Cac-flipped animals had a lower EJC amplitude compared to co-innervated controls, but still supported some release due to the contribution from unaffected ls synapses. However, a successful flip event in muscles solely innervated by a lb neuron dramatically decreased evoked responses, demonstrating Cac is not abundantly present at Cac-flipped AZs (Figure 1B and C). Immunostains to determine synaptic morphology (anti-HRP) and AZ number (anti-BRP) revealed these parameters are unaltered in *Cac^{lb-Flp}* neurons (Figure 1D and E). The apposition of presynaptic AZs to postsynaptic glutamate receptor fields was also unaffected in Cac-flipped neurons (Figure 1—figure supplement 1I-K). Only minor alterations in terminal morphology were observed, with ectopic filopodia forming from synaptic boutons in a subset of Cac-flipped NMJs, consistent with previously reported defects in synaptically silenced *Drosophila* synapses (Aponte-Santiago et al., 2020; Figure 1F). Thus, despite the dramatic reduction in evoked release reflecting a Cac-flip event early in synapse development, AZ seeding and subsequent synaptic growth occur at a normal rate.

Although AZ seeding occurs normally without Cac, structural maturation of the AZ scaffold or accumulation of SVs could be dependent on Cac presence. Quantitative immunostaining for two AZ scaffolds demonstrated normal BRP levels and a mild increase in RBP abundance at Cac-negative AZs (Figure 1G-I), indicating that AZ structural maturation through the developmental acquisition of key scaffold proteins can occur independent of Cac. To further assess if AZs formed after the flip event mature at a normal rate, the AZ population was divided into two groups based on BRP abundance. BRP enrichment correlates highly with AZ age (Akbergenova et al., 2018), indicating that AZs with the lowest BRP enrichment represent more recently formed AZs. Both groups of the AZ population

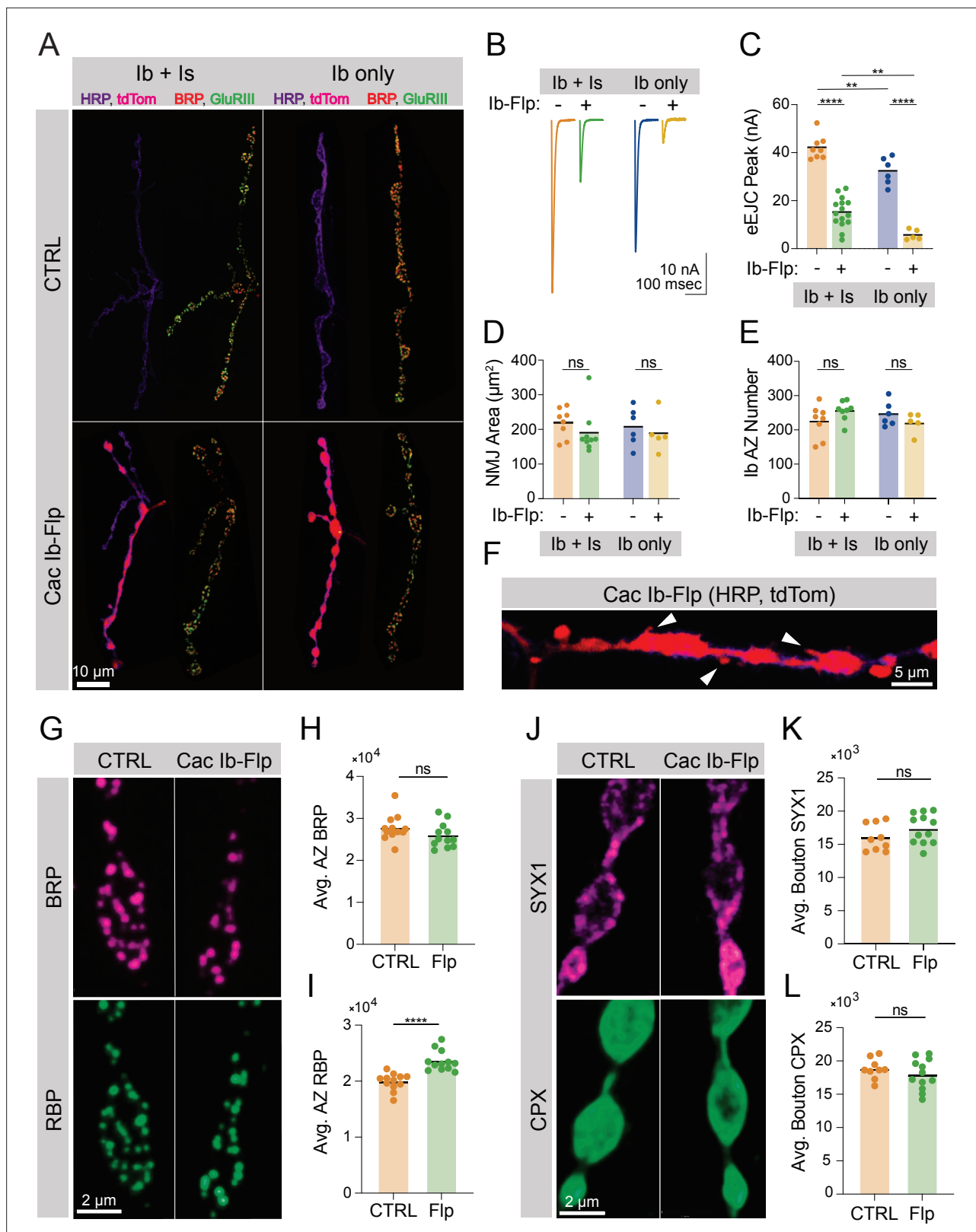


Figure 1. Ca²⁺ channels are not required for active zone (AZ) seeding or scaffold accumulation. **(A)** Representative images of control neuromuscular junctions (NMJs) with both Ib and Is motoneurons co-innervating muscle 1 (top left), or muscle 1 with only Ib innervation (top right), and Is and cac-flipped Ib neurons co-innervating muscle 1 (bottom left) or cac-flipped Ib neurons with no Is present (bottom right). The flip-reporter tdTomato (magenta) and HRP (neuronal membranes; purple) were imaged prior to fixation (left panels). After fixation, NMJs were immunostained for Bruchpilot

Figure 1 continued on next page

Figure 1 continued

(BRP) (red) and GluRIII (green) to label AZs and PSDs, respectively (right panels). **(B, C)** Average traces and evoked amplitudes (peak current, nA) from the indicated genotypes (co-innervated controls: orange, 42.11 ± 1.757 , $n=8$ NMJs from 6 animals; co-innervated $Cac^{lb-flip}$: green, 15.13 ± 1.607 , $n=15$ NMJs from 12 animals, $p < 0.0001$; lb-only controls: blue, 32.32 ± 2.329 , $n=6$ NMJs from 6 animals; lb-only $Cac^{lb-flip}$: gold, 5.749 ± 0.9544 , $n=5$ NMJs from 5 animals, $p < 0.0001$). **(D)** Neuronal (HRP-stained) area of lb synapses (co-innervated controls: orange, 219.1 ± 15.15 , $n=8$ NMJs from 6 animals; co-innervated $Cac^{lb-flip}$: green, 190.4 ± 21.12 , $n=9$ NMJs from 8 animals; lb-only controls: blue, 207.8 ± 22.4 , $n=6$ NMJs from 6 animals; lb-only $Cac^{lb-flip}$: gold, 189 ± 24.59 , $n=5$ NMJs from 5 animals). **(E)** Number of AZs formed by lb synapses (co-innervated controls: orange, 224.3 ± 16.88 ; co-innervated $Cac^{lb-flip}$: green, 255.1 ± 10.13 ; lb-only controls: blue, 245.8 ± 14.73 ; lb-only $Cac^{lb-flip}$: gold, 220.4 ± 13.47). **(F)** Some NMJs lacking Cac display ectopic filopodia extending from boutons (white arrowheads). **(G)** Representative images of cac-flipped NMJs stained with anti-BRP (magenta) and anti-RIM-binding protein (RBP) (green). **(H)** Quantification of BRP abundance. Each point represents the average fluorescence intensity across the AZ population of a single NMJ (CTRL: orange, $27,736 \pm 900.2$, $n=12$ NMJs from 6 animals; $Cac^{lb-flip}$: green, $25,943 \pm 843.7$, $n=12$ NMJs from 6 animals). **(I)** Quantification of RBP abundance (CTRL: orange, $19,910 \pm 439.2$; $Cac^{lb-flip}$: green, $23,593 \pm 530.6$, $p < 0.0001$). **(J)** Representative images of cac-flipped animals stained for syntaxin 1 (SYX1) (magenta) and complexin (CPX) (green). **(K)** Quantification of SYX1 abundance. Each point represents the average fluorescence intensity across the bouton population of a single NMJ (CTRL: orange, $16,028 \pm 683.5$, $n=9$ NMJs from 5 animals; $Cac^{lb-flip}$: green, $17,365 \pm 643.4$, $n=12$ NMJs from 6 animals). **(L)** Quantification of CPX abundance (CTRL: orange, $18,810 \pm 509.4$; $Cac^{lb-flip}$: green, $17,961 \pm 663.5$).

The online version of this article includes the following source data and figure supplement(s) for figure 1:

Source data 1. Source data for **Figure 1**.

Figure supplement 1. Characterization of Cac-flipping.

Figure supplement 1—source data 1. Source data for **Figure 1—figure supplement 1**.

had normal BRP abundance in Cac-flipped NMJs when compared to controls, further indicating that AZ Cac presence is not required for BRP to accumulate normally (**Figure 1—figure supplement 1 E, F**). When the AZ population was divided into two groups based on RBP enrichment, both the low-RBP and high-RBP halves of the AZ population displayed increased RBP enrichment in Cac-flipped NMJs (**Figure 1—figure supplement 1 G, H**). Similarly, mean bouton levels of the SV-associated protein complexin (CPX) and the t-SNARE syntaxin 1 (SYX1) were unchanged in Cac-negative neurons (**Figure 1 J–L**). These data indicate that Cac abundance is critical for determining AZ function, but its presence at an AZ does not play a significant role in facilitating that AZ's formation or structural maturation, similar to observations at mammalian central nervous system (CNS) synapses (**Held et al., 2020**).

BRP and Cac display distinct AZ accumulation trajectories

The independence of BRP scaffold formation from Cac suggests that their accumulation at growing AZs may be regulated through separate pathways. Alternatively, Cac and BRP could be co-regulated by a joint upstream component that implements a stoichiometric accumulation pattern during AZ development. It is unclear whether AZs cease accumulating new presynaptic components, or whether proteins such as BRP and Cac continue to accrue at AZs without a maturation endpoint. In a joint regulation model, the presence or absence of a cap on material accumulation would likely be the same for both proteins. Alternatively, a model where the two proteins are separately regulated would allow Cac and BRP to diverge in their accumulation trajectories over development. In wildtype larvae raised at 20°C, the larval stages are terminated after ~6 days by pupation, limiting the time available to observe AZ maturation. However, RNAi knockdown of the PTTH receptor, Torso, with a prothoracic gland GAL4 driver (*phm-GAL4*) extends larval development and triples the 3rd instar period (**Miller et al., 2012**). Quantitative imaging was used to determine whether the accumulation patterns of endogenously CRISPR-tagged Cac-GFP (**Gratz et al., 2019**) and immunostained BRP differed in long-lived larvae at day 6 and day 16 of development. These experiments test whether maturation trajectories of BRP and Cac display an endpoint, and whether they proceed stoichiometrically or diverge across extended developmental time.

Immunostaining of neuronal membranes and BRP-positive AZs demonstrated both NMJ area and AZ number increased between day 6 and day 16 (**Figure 2A–C**). These results are consistent with prior studies demonstrating muscle surface area and axonal arbors continue to grow during the extended larval period (**Miller et al., 2012**). TEVC recordings from muscle 6 revealed increased EJC amplitude in long-lived larvae at day 16 compared to day 6 (**Figure 2D and F**). This change reflects both an increase in quantal size (**Figure 2E and G**) and quantal content (**Figure 2H**). In addition, 16-day NMJs showed elevated spontaneous release frequency, consistent with the elevation in AZ number

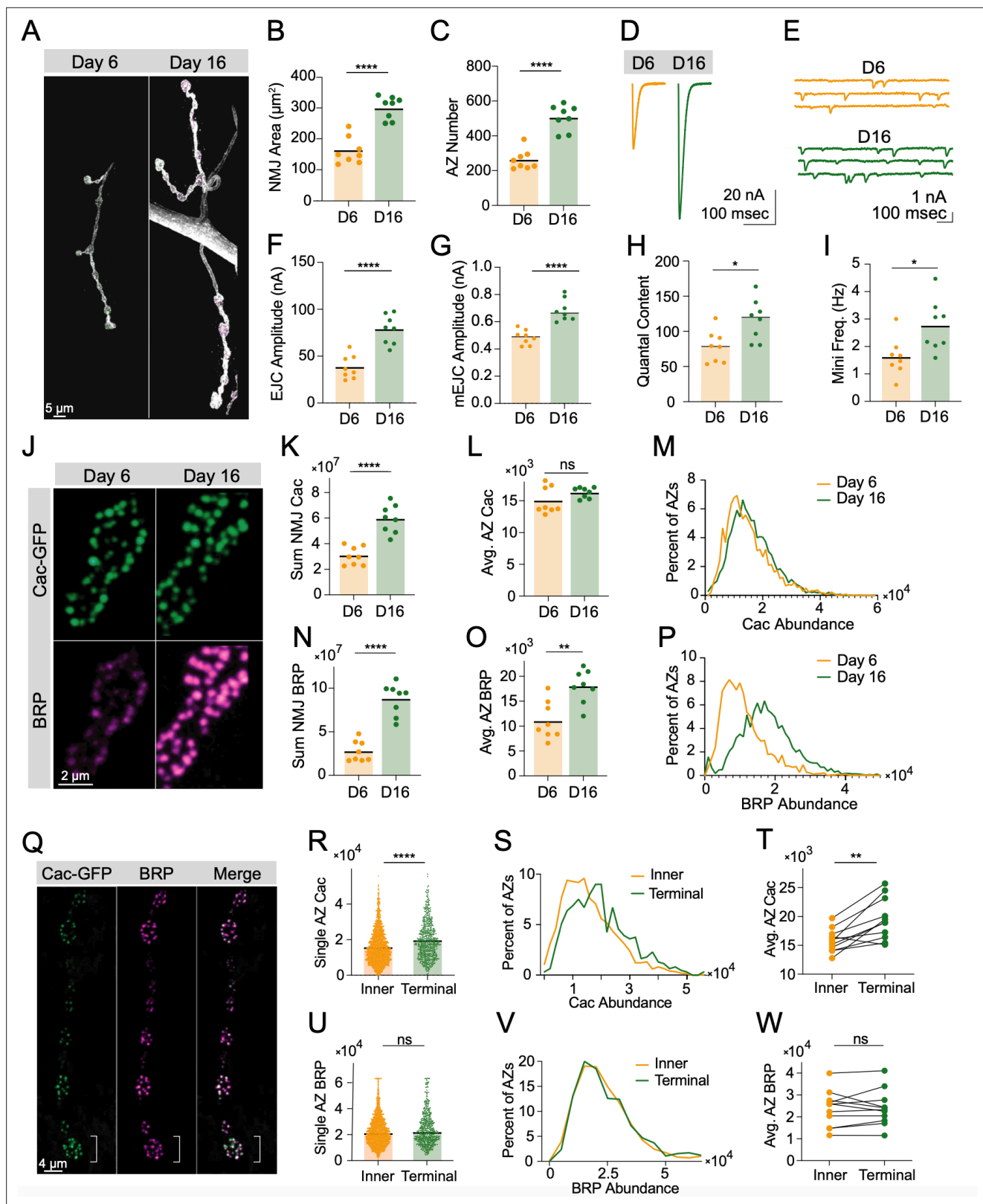


Figure 2. Bruchpilot (BRP) and Cac display distinct active zone (AZ) accumulation trajectories. **(A)** Representative muscle 4 neuromuscular junctions (NMJs) (stained with anti-HRP) in long-lived larvae (*phm-GAL4 >UAS-torso-RNAi*) at 6 and 16 days of larval life. **(B)** Synaptic (HRP stained) area at muscle 4 NMJs on day 6 and day 16 (D6: orange, 169.5 ± 16.03 , $n=8$ NMJs from 6 animals; D16: green, 316.9 ± 13.64 , $n=8$ NMJs from 6 animals, $p < 0.0001$). **(C)** BRP-positive AZ number at muscle 4 NMJs on day 6 and day 16 (D6: orange, 261.6 ± 20.02 , D16: green, 504.8 ± 25.86 , $p < 0.0001$). **(D, E)** Average

Figure 2 continued on next page

Figure 2 continued

EJC traces and representative mEJC traces at muscle 6 NMJs on day 6 and day 16. **(F)** Average evoked amplitudes (peak current, nA) (D6: orange, 38.27 ± 4.421 , $n=8$ NMJs from 6 animals; D16: green, 78.35 ± 5.476 , $n=8$ NMJs from 6 animals, $p < 0.0001$). **(G)** Average mEJC peak amplitude (nA) (D6: 0.4862 ± 0.01891 ; D16: 0.6843 ± 0.9284 , $p < 0.0001$). **(H)** Quantal content (D6: 78.41 ± 8.012 ; D16: 116.4 ± 10.35 , $p = 0.0116$). **(I)** Average mini frequency (D6: 1.617 ± 0.2448 , D16: 2.748 ± 0.3335 , $p = 0.0161$). **(J)** Representative synaptic boutons with endogenously tagged Cac-GFP (green) and BRP (magenta). **(K)** Sum Cac abundance per NMJ (D6: $30,486,042 \pm 2,547,718$, $n=8$ NMJs from 6 animals; D16: $59,296,888 \pm 3,909,993$, $n=8$ NMJs from 6 animals, $p < 0.0001$). **(L)** Average AZ Cac-GFP signal intensity at NMJs on day 6 and day 16 (D6: $15,058 \pm 746.1$; D16: $16,296 \pm 290.9$). **(M)** Histogram showing distribution of Cac-GFP intensities across the AZ population at day 6 and day 16 NMJs. **(N)** Sum BRP abundance per NMJ (D6: $27,664,071 \pm 4,206,865$; D16: $87,502,172 \pm 6,434,001$, $p < 0.0001$). **(O)** Average AZ BRP abundance per NMJ (D6: $11,132 \pm 1350$; D16: $17,985 \pm 1178$, $p < 0.01$). **(P)** Histogram showing distribution of BRP intensities across the AZ population at day 6 and day 16 NMJs. **(Q)** Representative images of muscle 4 lb NMJs showing Cac-GFP (green) and BRP (magenta). The white bracket marks the terminal bouton. **(R)** AZ Cac abundance at inner boutons versus terminal boutons, with each point representing the maximum fluorescent pixel intensity for one AZ (Inner: $15,879 \pm 213$, $n=1951$ AZs; Terminal: $19,617 \pm 415.1$, $n=612$ AZs, $p < 0.0001$). **(S)** Distribution of AZ Cac-GFP intensities across the AZ population in inner boutons versus terminal boutons. **(T)** Average AZ Cac intensity for inner boutons versus terminal boutons. Inner boutons and terminal boutons from a single NMJ are connected with a line. **(U)** BRP abundance at AZs of inner versus terminal boutons (Inner: $23,009 \pm 262.8$, $n=1917$ AZs; Terminal: $24,210 \pm 504.1$, $n=602$ AZs). **(V, W)** BRP intensity distributions and pairwise comparisons of inner versus terminal boutons.

The online version of this article includes the following source data for figure 2:

Source data 1. Source data for **Figure 2**.

(Figure 2E,I). Quantitative confocal imaging of endogenously tagged Cac-GFP and immunostained BRP at long-lived NMJs confirmed the continued biosynthesis, trafficking, and delivery of these AZ components throughout development, as the sum of both Cac and BRP across the entire NMJ is elevated at day 16. However, while total BRP abundance increased by roughly fourfold at the NMJ, Cac abundance showed only an approximately twofold increase, similar to the twofold increase in AZ number **(Figure 2C, J, K and N)**. Measurements of Cac-GFP at individual AZs revealed the average AZ Cac abundance in 16-day-old NMJs was not increased beyond that observed at day 6, and the distribution of Cac abundance across the AZ population did not change **(Figure 2L and M)**. Thus, doubling of total Cac protein at the NMJ precisely reflected the amount necessary to maintain the AZ Cac distribution given the increase in AZ number. In contrast, BRP accumulation continued at AZs throughout the extended larval stage, resulting in a shift in the entire AZ population toward higher BRP abundance **(Figure 2O and P)**, consistent with prior observations **(Perry et al., 2020)**. These data demonstrate that prolonged access to new Cac and BRP results in an increased BRP-enriched AZ population with no alteration in AZ Cac accumulation, suggesting that separate regulatory mechanisms control their AZ abundance. In addition, these results suggest that Cac accumulation, but not BRP, is capped at growing AZs.

To probe whether BRP and Cac accumulation at AZs are also regulated separately in a wildtype background, we analyzed the abundance of these components at AZs across the synaptic arbor **(Figure 2Q)**. Cac abundance was significantly increased at AZs in terminal boutons at muscle 4 **(Figure 2R–T)**. In contrast, BRP AZ abundance was not increased in terminal boutons **(Figure 2U–W)**. The unique dependence of Cac accumulation on arbor location indicates accumulation of the two proteins is regulated separately at AZs in a wildtype NMJ, consistent with their distinct accumulation trajectories in long-lived larvae.

AZ Cac accumulation is regulated downstream of Cac biosynthesis

The cap on AZ Cac abundance across prolonged development despite continued delivery of new Cac channels suggests that regulation downstream of Cac biosynthesis allows for a stable Cac distribution to be maintained under varying environmental or developmental conditions **(Figure 2)**. To determine if AZ Cac abundance is bidirectionally buffered against moderate changes in biosynthesis, the effects of increasing whole-neuron Cac levels using Cac overexpression, and decreasing Cac levels using a heterozygous cac deficiency, were assayed. Since a C-terminal-tagged UAS-Cac-GFP^C overexpression construct has been demonstrated to localize to AZs and support synaptic transmission **(Kawasaki et al., 2004)**, an identical C-terminal tag was inserted into the endogenous Cac locus (Cac-GFP^C) using CRISPR so protein products of the endogenous and overexpressed locus are identical. Larvae expressing Cac-GFP^C had normal NMJ area defined by anti-HRP staining and showed a mild decrease in AZ number **(Figure 3—figure supplement 1A–C)**. In contrast to the N-terminally tagged Cac-GFP^N used in previous experiments **(Gratz et al., 2019)**, total Cac fluorescence in Cac-GFP^C,

C155>UAS-Cac-GFP NMJs can be quantitatively imaged without the confounds of different GFP identities and tagging locations.

Quantitative confocal imaging of Cac abundance at NMJs with BRP immunostaining to label AZs revealed nearly identical AZ Cac abundance following Cac overexpression compared with controls, suggesting that Cac levels at growing AZs are rate-limited downstream of Cac biosynthesis, and that Cac channels compete for limited delivery or incorporation into growing AZs (**Figure 3A–C**). Overexpression of red-tagged UAS-Cac-tdTomato in the CRISPR-tagged Cac-GFP background directly demonstrated this competition between Cac channels, as Cac-tdT overexpression resulted in an ~70% decrease in Cac-GFP abundance at AZs (**Figure 3D and E**). TEVC recordings demonstrated that Cac overexpression does not significantly increase release, consistent with the failure of Cac overexpression to drive increased Cac abundance at AZs (**Figure 3F and G**). Together, these results indicate that AZs resist over-accumulating Cac channels in conditions of increased cellular availability. This reflects observations in extended larval stage animals and suggests that AZ Cac incorporation is limited downstream of Cac biosynthesis, perhaps by regulated trafficking, incorporation, or retention at synapses.

Though Cac biosynthesis is not a limiting regulatory point of AZ Cac incorporation, it is possible that Cac biosynthesis precisely matches Cac demand in growing NMJs. In this model, moderate reductions in Cac biosynthesis should result in similar reductions in AZ Cac levels. Alternatively, Cac could be biosynthesized in excess of AZ demand in wildtype situations, resulting in AZs being buffered against moderate reductions in Cac biosynthesis. Western blot analysis of adult head extracts of female animals with endogenously tagged Cac-GFP in heterozygous combination with a chromosomal deletion spanning the *cac* locus (*cac^{GFP/Df}*) revealed that whole-brain Cac levels in *cac^{GFP/Df}* heterozygotes were reduced to 52% of control (homozygous *cac^{GFP}*) levels (**Figure 3H,I**). Despite the twofold reduction in Cac biosynthesis, MN4-Ib AZs in *cac^{GFP/Df}* heterozygotes retained 90% of control Cac-GFP levels without a change in AZ number (**Figure 3J–M**). Quantitative confocal imaging of Cac-GFP fluorescence in female larvae expressing endogenously tagged Cac-GFP in combination with untagged wildtype Cac (*cac^{GFP/+}*) demonstrated exactly 50% of AZ fluorescence intensity when compared to *cac^{GFP}* homozygotes, verifying these methods accurately report fold-change in protein abundance (**Figure 3—figure supplement 2A, B**). Other image analysis metrics, including sum GFP fluorescence in ROIs covering each AZ, revealed similarly robust quantification (**Figure 3—figure supplement 2C–G**).

While bidirectional buffering mitigates AZ Cac depletion in *cac* deficiency heterozygotes, even small changes in Cac abundance are predicted to impact release due to the steep reliance of P_r on presynaptic Ca^{2+} influx. Beyond the 10% decrease in AZ Cac levels at MN4-Ib terminals, Cac-GFP intensity at the co-innervating MN4-Is AZs revealed a greater decrease of 30%, perhaps due to the bigger size of the Is terminal which innervates a large subset of muscles and may have increased demand for Cac channels (**Figure 3N**). Electrophysiological recordings in *cac^{GFP/Df}* heterozygous NMJs confirmed a 60% decrease in evoked peak current compared to controls, corresponding to the composite 10% and 30% reductions in AZ Cac abundance in Ib and Is neurons, respectively (**Figure 3O and P**). This highlights the functional significance of mild alterations in AZ Cac abundance. Overall, these results demonstrate that at wildtype synapses, Cac AZ abundance is buffered against moderate decreases or increases in biosynthesis, suggesting that the rate-limiting factor for AZ Cac incorporation is situated downstream of its biosynthesis levels.

BRP biosynthesis rate-limits BRP accumulation at AZs

In contrast to Cac, AZs continue to accrue BRP given extended developmental time (**Figure 2**), suggesting that BRP biosynthesis may rate-limit AZ BRP incorporation into growing AZs. In a biosynthesis-limiting model, moderate decreases in neuronal BRP abundance should result in comparable decreases of the protein at AZs. This hypothesis is consistent with prior observations that AZ BRP abundance is negatively correlated with AZ number in mutants with altered AZ number (**Goel et al., 2019**). Reductions in BRP abundance using either a heterozygous BRP deficiency (*brp^{Df/+}*) or pan-neuronal expression of BRP RNAi revealed a linear relationship between whole-cell and AZ BRP abundance (**Figure 4A–D**). Western blot analysis of head extracts demonstrated that *brp^{Df/+}* heterozygotes produced 65% of control levels of the protein, with AZ BRP abundance reduced to 64% of control levels. Similarly, pan-neuronal RNAi knockdown reduced BRP levels to 14% in whole brains, resulting in a comparable reduction to 15% at AZs. These results are consistent with the increase in

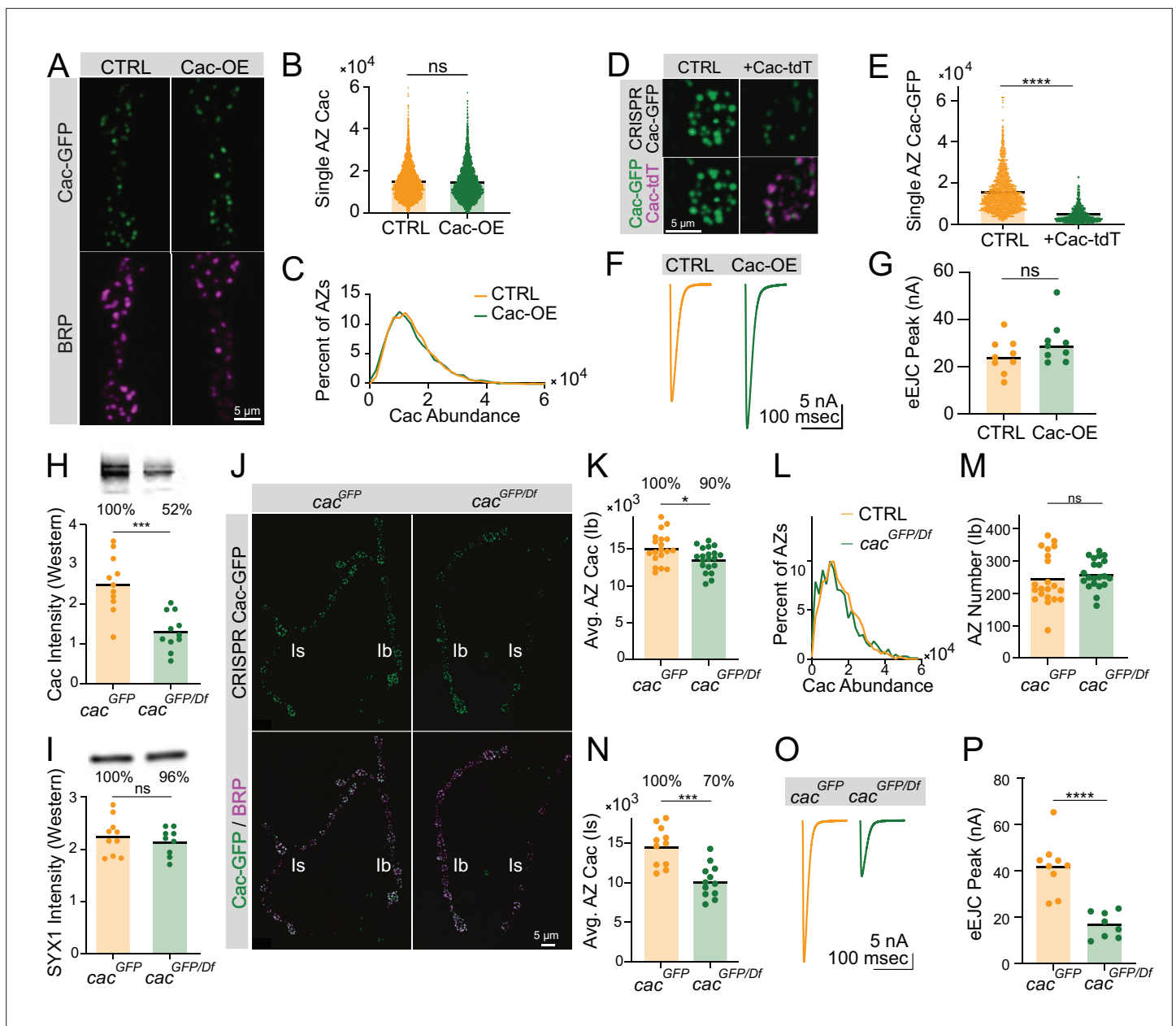


Figure 3. Active zone (AZ) Cac accumulation is regulated downstream of Cac biosynthesis. **(A)** Representative images of Cac-GFP (green) and Bruchpilot (BRP) (magenta) at muscle 4 for endogenously C-terminally tagged Cac-GFP controls (*cac^{GFP(C)}*, *C155/cac^{GFP(C)}*) and Cac overexpression animals (*cac^{GFP(C)}*, *C155/cac^{GFP(C)}*, *UAS-Cac-GFP*). **(B)** Quantification of AZ Cac intensity in control versus Cac overexpression neuromuscular junctions (NMJs). Each point represents the maximum Cac-GFP pixel intensity of a single AZ (control: 14617 ± 130.8 , $n=3663$ AZs from 10 NMJs from 6 animals; Cac OE: $14,383 \pm 148.2$, $n=3145$ AZs from 10 NMJs from 6 animals). **(C)** Distribution of AZ Cac-GFP abundance across the AZ population in control versus Cac overexpression NMJs. **(D)** Representative images of endogenously tagged Cac-GFP (green) and overexpressed Cac-tdTomato (magenta) at AZs in control (*cac^{GFP}*, *C155*) versus Cac-tdTomato overexpression (*cac^{GFP}*, *C155*; *UAS-Cac-tdT*). **(E)** Quantification of AZ Cac-GFP intensity with and without Cac-tdTomato overexpression (control: $15,339 \pm 232$, $n=1613$ AZs, Cac-tdT: 4477 ± 123.9 , $n=850$ AZs, $p < 0.0001$). **(F, G)** Average traces and evoked peak currents (nA) at muscle 6 in Cac overexpression and control animals (control: 24.45 ± 2.433 , $n=9$ NMJs from 5 animals; Cac OE: 30.11 ± 3.046 , $n=9$ NMJs from 5 animals). **(H, I)** Quantifications and representative images of Western blots of adult head extracts from *cac^{GFP/Df}* heterozygotes and *cac^{GFP}* controls ($n=11$ samples, extracts from 5 adult heads per sample). Each point in **H** represents Cac intensity in one lane (*cac^{GFP}*: $25,092 \pm 2146$; *cac^{GFP/Df}*: $13,055 \pm 1403$, $p < 0.001$). Each point in **I** represents syntaxin 1 (SYX1) intensity in one lane (*cac^{GFP}*: $224,900 \pm 11,239$; *cac^{GFP/Df}*: $214,889 \pm 86,96$). Representative images for Cac and SYX are shown above each quantification. **(J)** Representative images of endogenous Cac-GFP (green) and BRP (magenta) at muscle 4 AZs in *cac^{GFP/Df}* heterozygotes and *cac^{GFP}* controls. lb and ls terminals are labeled in white. **(K)** Quantification of average Cac-GFP AZ abundance per MN4-lb NMJs (*cac^{GFP}*: $15,105 \pm 486.3$, $n=19$ NMJs from 7 animals; *cac^{GFP/Df}*: $13,617 \pm 365.9$, $n=21$ NMJs from 7 animals, $p < 0.05$). **(L)** Histogram of Cac-GFP intensity across the AZ population in *cac^{GFP/Df}* heterozygotes and *cac^{GFP}* controls at MN4-lb NMJs. **(M)** BRP-positive AZ number per MN4-lb NMJ (*cac^{GFP}*: 250 ± 20 , $n=19$ NMJs; *cac^{GFP/Df}*: 260 ± 20 , $n=21$ NMJs, $p = ns$). **(N)** Average traces and evoked peak currents (nA) at muscle 6 in Cac overexpression and control animals (control: 24.45 ± 2.433 , $n=9$ NMJs from 5 animals; Cac OE: 30.11 ± 3.046 , $n=9$ NMJs from 5 animals). **(O)** Average traces and evoked peak currents (nA) at muscle 6 in Cac overexpression and control animals (control: 24.45 ± 2.433 , $n=9$ NMJs from 5 animals; Cac OE: 30.11 ± 3.046 , $n=9$ NMJs from 5 animals). **(P)** Average traces and evoked peak currents (nA) at muscle 6 in Cac overexpression and control animals (control: 24.45 ± 2.433 , $n=9$ NMJs from 5 animals; Cac OE: 30.11 ± 3.046 , $n=9$ NMJs from 5 animals).

Figure 3 continued on next page

Figure 3 continued

243.4±17.05; $cac^{GFP/Df}$: 260.3±9.963). (N) Quantification of average AZ Cac-GFP intensity per Is innervation of muscle 4 NMJs (cac^{GFP} : 14,621±747.5, n=11 NMJs from 7 animals; $cac^{GFP/Df}$: 10,219±601 n=12 NMJs from 7 animals, p<0.001). (O, P) Average traces and evoked peak currents (nA) at muscle 6 in $cac^{GFP/Df}$ heterozygotes and cac^{GFP} controls (cac^{GFP} : 41.96±3.879, n=9 NMJs from 5 animals; $cac^{GFP/Df}$: 16.7±1.984, n=8 NMJs from 7 animals, p<0.0001).

The online version of this article includes the following source data and figure supplement(s) for figure 3:

Source data 1. Source data for **Figure 3**.

Source data 2. Western regions used for **Figure 3**.

Source data 3. Western for **Figure 3**.

Figure supplement 1. Synaptic morphology of Cac-GFP C-terminal CRISPR-tagged larvae.

Figure supplement 1—source data 1. Source data for **Figure 3—figure supplement 1**.

Figure supplement 2. Quantitative imaging control.

Figure supplement 2—source data 1. Source data for **Figure 3—figure supplement 2**.

AZ BRP observed during extended larval stages and indicate that BRP biosynthesis determines AZ BRP abundance.

BRP enrichment does not limit AZ Cac accumulation

Given the requirement of BRP for proper Cac accumulation at AZs (Fouquet et al., 2009), it is possible that BRP abundance is a limiting factor for Cac incorporation into growing AZs. An alternative model is that Cac accumulation requires BRP but is not limited by the amount of BRP at AZs, consistent with the observation that elevated BRP levels at AZs of 16-day-old long-lived larvae do not promote increased Cac levels (Figure 2). Quantitative confocal imaging of endogenously tagged Cac-GFP at AZs in control, $brp^{Df/+}$ heterozygotes, and pan-neuronal BRP knockdown revealed that BRP is required but not rate-limiting for AZ Cac accumulation (Figure 4A and E). BRP knockdown to 15% of control BRP levels resulted in a moderate reduction of Cac AZ abundance (69% of control levels), reflecting the importance of BRP in facilitating AZ Cac accumulation as previously reported (Fouquet et al., 2009). However, although AZ BRP is reduced by 36% in $brp^{Df/+}$ heterozygotes, Cac-GFP is present at normal levels (Figure 4B and E). Evoked synaptic transmission following single action potentials was unaffected by this 36% reduction in AZ BRP, further indicating Cac abundance is unaffected by a moderate reduction in AZ BRP enrichment (Figure 4F and G).

To further assess the extent to which AZ BRP enrichment is required for normal Cac accumulation, AZs in NMJs of animals expressing pan-neuronally driven BRP RNAi were subdivided into two groups based on the presence or absence of BRP. When all Cac-positive AZs were analyzed regardless of their BRP presence or absence, AZ Cac levels were significantly lower at BRP RNAi NMJs (Figure 4—figure supplement 1A-C). However, when only the BRP-positive AZs were analyzed, Cac levels were normal despite an ~80% reduction in BRP abundance compared to controls (Figure 4—figure supplement 1D-G). These data further indicate that although BRP abundance may rate-limit other aspects of AZ structural or functional maturation, it is not a limiting factor in Cac accumulation at AZs.

Cac accumulation at AZs is dosage sensitive to the $\alpha 2\delta$ subunit

Across multiple systems, the highly conserved VGCC subunit $\alpha 2\delta$ promotes channel surface expression. In rodents, $\alpha 2\delta$ overexpression leads to increased surface VGCC density and increased synaptic release, indicating $\alpha 2\delta$ is a rate-limiting factor in VGCC accumulation (Hoppa et al., 2012). In *Drosophila*, mutations in the $\alpha 2\delta$ subunit (*straightjacket*) lead to reduced Cac at nerve terminals, reduced synaptic growth, and failure of synaptic homeostasis (Ly et al., 2008; Dickman et al., 2008; Kurshan et al., 2009; Wang et al., 2016). Consistently, quantitative confocal imaging of endogenously tagged Cac-GFP in animals heterozygous for a combination of the $\alpha 2\delta^2$ null allele and an $\alpha 2\delta$ splice site mutant that reduces full-length protein expression ($cac^{GFP}; \alpha 2\delta^{2/k10814}$) revealed a large decrease in AZ Cac levels to 36% of control levels, with a third of AZs lacking detectable Cac (Figure 5A-C). TEVC recordings revealed a severe decrease in evoked current, reflecting the reduction in Cac levels at this terminal (Figure 5D and E). Imaging of Cac-GFP in animals heterozygous for the $\alpha 2\delta^2$ null allele ($cac^{GFP}; \alpha 2\delta^{2/+}$) indicates that Cac abundance at AZs is dosage sensitive to $\alpha 2\delta$, as Cac-GFP was reduced

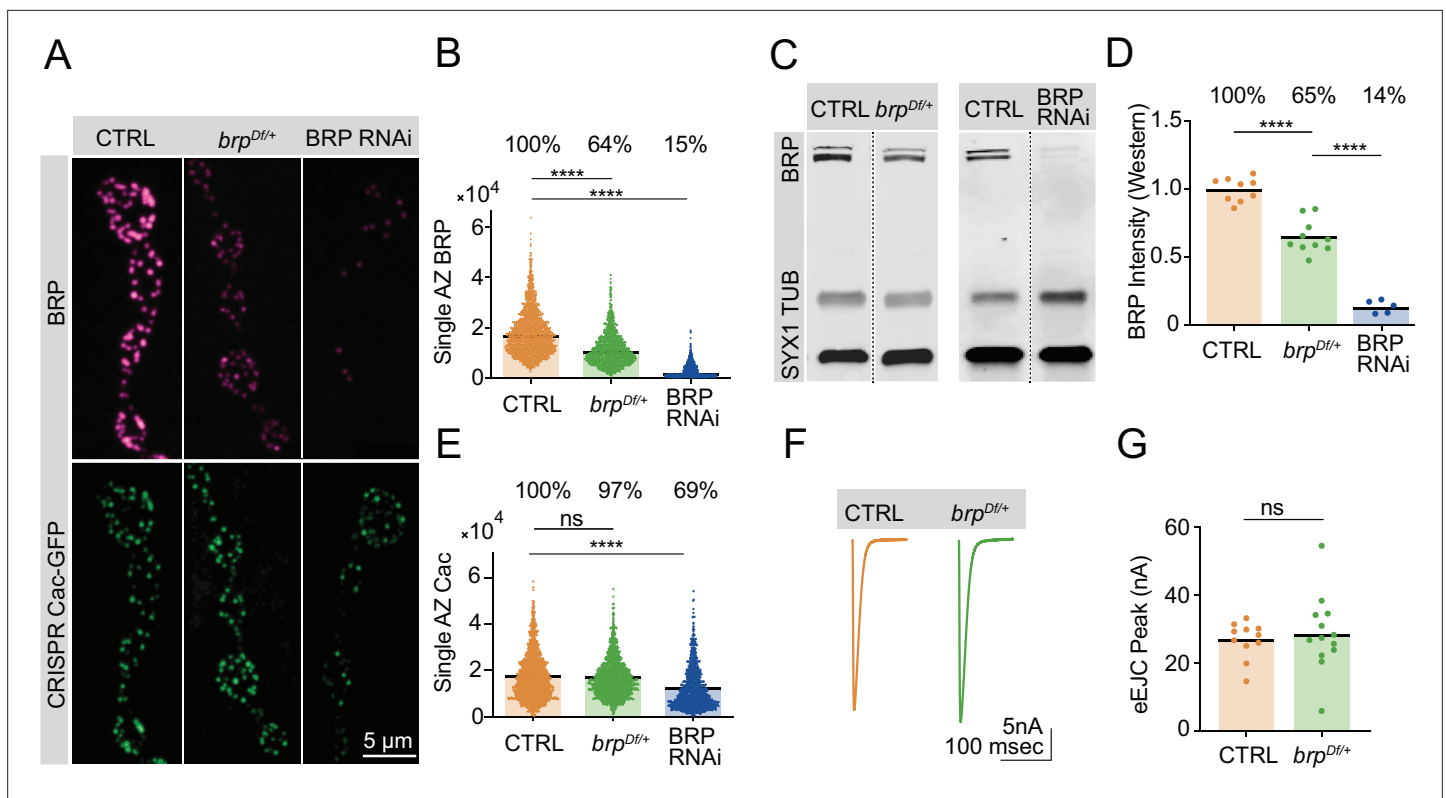


Figure 4. Bruchpilot (BRP) biosynthesis rate-limits active zone (AZ) BRP incorporation. **(A)** Representative images of BRP and endogenously tagged Cac-GFP at AZs in controls, *brp^{Df/+}* heterozygotes and pan-neuronally (*elav-GAL4*) expressed BRP RNAi. **(B)** Quantification of single AZ BRP intensity, with average AZ BRP intensity listed as a percent of control above each genotype (control: $18,161 \pm 210.7$, $n=1779$ AZs; *brp^{Df/+}*: $11,534 \pm 176.7$, $n=1350$ AZs, $p < 0.0001$; BRP RNAi: 2806 ± 79.91 , $n=1140$ AZs, $p < 0.0001$). **(C)** Representative image of Western blots of adult head extracts from control and *brp^{Df/+}* heterozygotes (left panel), and control and pan-neuronally expressed BRP RNAi animals (right panel) stained for syntaxin 1 (SYX1) (loading control), Tubulin, and BRP. **(D)** Quantification of BRP intensity in Western blots of the indicated genotypes. Each point represents BRP intensity in one lane, with BRP intensity normalized to the SYX1 loading control. Percent of protein abundance compared to control (100%) is shown above each genotype (control: 1.0 ± 0.02912 , $n=9$ lanes; *brp^{Df/+}*: 0.6518 ± 0.03862 , $n=10$ lanes, $p < 0.0001$; BRP RNAi: 0.1366 ± 0.02117 , $n=5$ lanes, $p < 0.0001$). **(E)** Quantification of endogenously tagged Cac-GFP intensity at single AZs in controls, *brp^{Df/+}* heterozygotes, and pan-neuronally expressed BRP RNAi (control: $17,268 \pm 232.4$, $n=1757$ AZs; *brp^{Df/+}*: $16,788 \pm 217$, $n=1403$ AZs; BRP RNAi: $11,959 \pm 259$, $n=1140$ AZs, $p < 0.0001$). **(F, G)** Average traces and quantified evoked peak currents (nA) in control and *brp^{Df/+}* heterozygotes at muscle 6 (control: 26.78 ± 1.632 , $n=11$ neuromuscular junctions (NMJs); *brp^{Df/+}*: 28.71 ± 3.105 , $n=13$ NMJs).

The online version of this article includes the following source data and figure supplement(s) for figure 4:

Source data 1. Source data for **Figure 4**.

Source data 2. Western for **Figure 4** panel C - BRP deficiency heterozygote.

Source data 3. Western regions used for **Figure 4** panel C - BRP RNAi.

Figure supplement 1. Single active zone (AZ) analysis of Cac and Bruchpilot (BRP) following BRP RNAi knockdown.

Figure supplement 1—source data 1. Source data for **Figure 4—figure supplement 1**.

to 83% of control levels in the $\alpha 2\delta^{2/+}$ heterozygote, with release significantly reduced compared to controls (**Figure 5A–E**).

To further examine whether AZ Cac accumulation is rate-limited by $\alpha 2\delta$, UAS- $\alpha 2\delta$ was pan-neuronally overexpressed in the CRISPR Cac-GFP background (*cac^{GFP}, elav-Gal4;; UAS- $\alpha 2\delta$*). $\alpha 2\delta$ overexpression increased average AZ Cac abundance to 123% of driver-only control levels (**Figure 5F and G**), in contrast with Cac-GFP overexpression, which failed to promote increased Cac accumulation at AZs (**Figure 3A–C**). However, this increase in AZ Cac abundance was non-uniform across the AZ population, as AZs with the highest levels of Cac were unaffected by $\alpha 2\delta$ overexpression (**Figure 5H**). Because this population is predicted to be the high releasing AZs that drive a majority of release in low external Ca^{2+} (**Akbergenova et al., 2018**), and because low P_r AZs facilitate while high P_r AZs depress

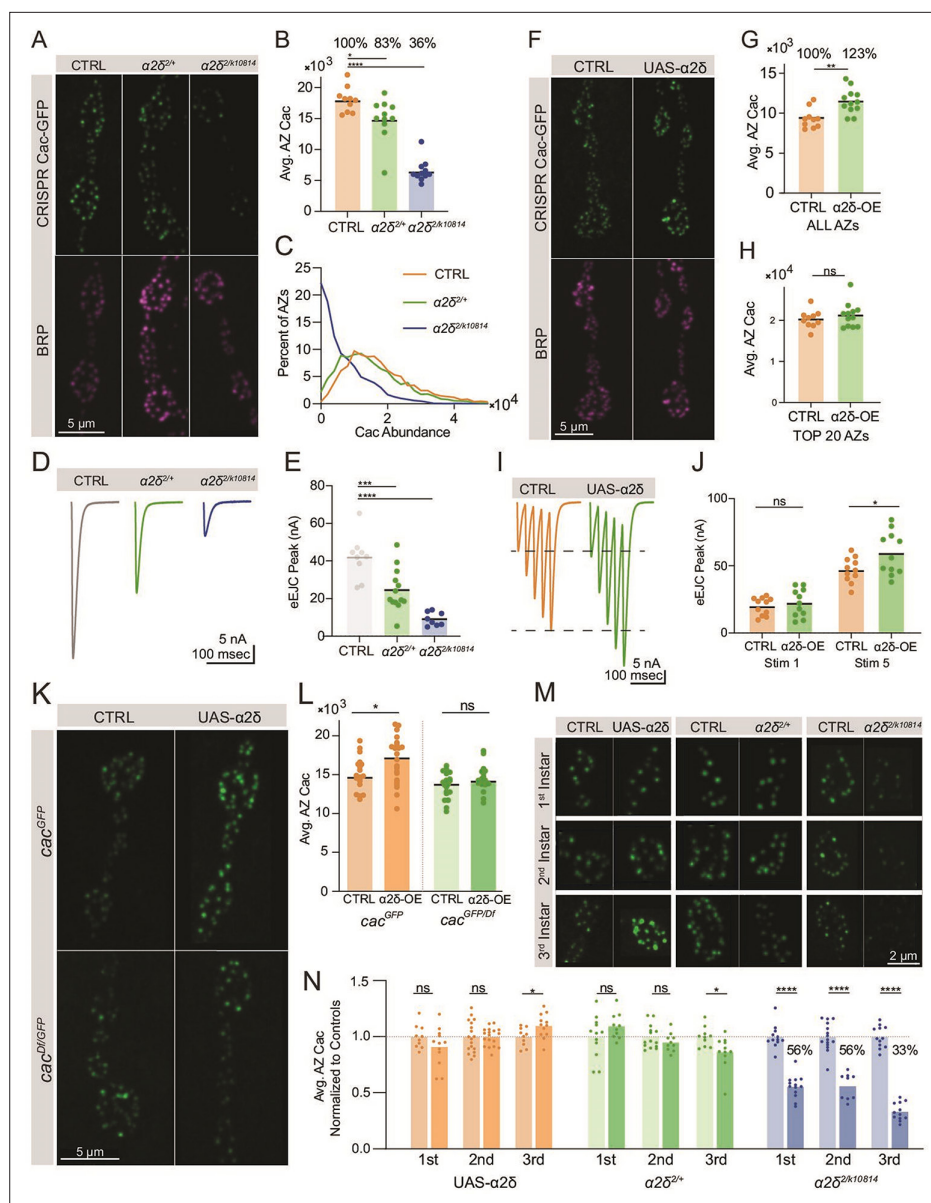


Figure 5. Cac accumulation at active zones (AZs) is dosage sensitive to the $\alpha 2\delta$ subunit. **(A)** Representative images of endogenously tagged Cac-GFP (green) and Bruchpilot (BRP) (magenta) in controls (cac^{GFP}), $\alpha 2\delta$ null heterozygotes ($cac^{GFP}; \alpha 2\delta^{2/+}$) and $\alpha 2\delta^{2/k10814}$ transheterozygotes ($cac^{GFP}; \alpha 2\delta^{2/k10814}$). **(B)** Quantification of average AZ Cac-GFP fluorescence of neuromuscular junctions (NMJs) in each genotype. Cac abundance as a percent of control levels is shown above each genotype (control: $18,007 \pm 641.1$, $n=10$ NMJs from 5 animals; $\alpha 2\delta^{2/+}$: $14,926 \pm 1014$, $n=11$ NMJs from 6 animals, $p=0.0174$; $\alpha 2\delta^{2/k10814}$: 6542 ± 541.3 , $n=11$ NMJs from 6 animals, $p<0.0001$). **(C)** Frequency distribution of single AZ Cac-GFP intensity across the AZ population in each genotype. **(D, E)** Average traces and quantified evoked peak current (nA) at muscle 6 for each genotype. Recordings were collected in combination with $cac^{GFP/Df}$ heterozygotes (**Figure 3P**) and the control is replicated here in gray for ease of comparison (control: 41.96 ± 3.879 , $n=9$ NMJs; $\alpha 2\delta^{2/+}$: 24.53 ± 3.133 , $n=13$ NMJs, $p<0.001$; $\alpha 2\delta^{2/k10814}$: 9.161 ± 1.268 , $n=8$ NMJs, $p<0.0001$). **(F)** Representative images of endogenously tagged Cac-GFP (green) and BRP (magenta) in control ($cac^{GFP}; C155$) and $\alpha 2\delta$ overexpression animals ($cac^{GFP}; C155; UAS-\alpha 2\delta$). **(G)** Average AZ Cac abundance per NMJ (control: 9332 ± 388.6 , $n=10$ NMJs from 5 animals; $\alpha 2\delta$ OE: 11497 ± 449.8 , $n=12$ NMJs from 6 animals, $p=0.0019$). **(H)** Average of top 20 brightest AZs per NMJ (control: $22,996 \pm 752.5$; $\alpha 2\delta$ OE: $24,823 \pm 1011$). **(I, J)** Average traces and quantified 1st and 5th stimulus evoked peak current at muscle 6 in 0.25 mM external Ca^{2+} for controls and $\alpha 2\delta$ overexpression animals (control 1st: 19.87 ± 1.98 , $n=11$ NMJs; $\alpha 2\delta$ OE 1st: 22.45 ± 3.127 , $n=11$ NMJs; control 5th: 46.82 ± 2.794 ; $\alpha 2\delta$ OE 5th: 59.21 ± 4.839 , $p=0.0249$). **(K, L)** Representative images and quantification of endogenously tagged Cac-GFP with (right) and without (left) $\alpha 2\delta$ overexpression in either control **Figure 5 continued on next page**

Figure 5 continued

(top) or *cac^{GFP/Df}* heterozygous (bottom) NMJs (*cac^{GFP},C155*: 15,105±486.3, n=19 NMJs; *cac^{GFP},C155;UAS-α2δ/+*: 17,142±814.4, n=15 NMJs, p<0.0225; *cac^{Df}/cac^{GFP},C155*: 13,617±365.9, n=20 NMJs; *cac^{Df}/cac^{GFP},C155;UAS-α2δ/+*: 14,895±587, n=12 NMJs). (M, N) Representative images and quantification of average AZ Cac intensity per NMJ of endogenously tagged Cac-GFP in 1st, 2nd, and 3rd instar muscle 4 lb NMJs in *α2δ* overexpression, *α2δ^{2/+}*, and *α2δ^{2/k10814}* animals. Each pairwise comparison was normalized so that the control average is 1.0 (*α2δ*-OE 1st: 0.9125±0.0496, n=12 NMJs; *α2δ*-OE 2nd: 1±0.019, n=18 NMJs; *α2δ*-OE 3rd: 1.098±0.03132, n=12 NMJs, p=0.0296; *α2δ^{2/+}* 1st: 1.096±0.0361, n=10 NMJs; *α2δ^{2/+}* 2nd: 0.9525±0.02574, n=10 NMJs; *α2δ^{2/+}* 3rd, p=0.0213; 0.8661±0.04408, n=11 NMJs; *α2δ^{2/k10814}* 1st: 0.5569±0.02853, n=15 NMJs, p<0.0001; *α2δ^{2/k10814}* 2nd: 0.5619±0.03902, n=9 NMJs, p<0.0001; *α2δ^{2/k10814}* 3rd: 0.3344±0.02298, n=12 NMJs, p<0.0001).

The online version of this article includes the following source data and figure supplement(s) for figure 5:

Source data 1. Source data for **Figure 5**.

Figure supplement 1. *α2δ*'s role in regulating neuromuscular junction (NMJ) morphology is not dosage-sensitive and its Cac localization phenotype is independent of axon length.

Figure supplement 1—source data 1. Source data for **Figure 5—figure supplement 1**.

(Peled and Isacoff, 2011; Newman et al., 2017), the increase in Cac at low-releasing sites due to *α2δ* overexpression is predicted to have a limited effect on single action potential release (dominated by high *P_r*, AZs), but would enhance facilitation during a short train of action potentials (when lower *P_r*, AZs contribute more to net release). Consistent with this prediction, TEVC recordings showed that evoked peak current in the first stimulation in a train of five action potentials was unaffected by *α2δ* overexpression, but an increase in response was observed by the fifth stimulus (**Figure 5I and J**). Together, these results demonstrate that unlike BRP, which is required but not rate-limiting for Cac accumulation at AZs, *α2δ* is both required and rate-limiting for this process.

The mechanism by which *α2δ* rate-limits Cac AZ abundance is unclear, as *α2δ* could control a bottleneck in Cac trafficking and/or promote Cac stabilization at AZs' post-incorporation. At NMJs of 3rd instar larvae, AZ Cac abundance is almost fully maintained at AZs even when total neuronal Cac abundance is reduced by 50% (**Figure 3**), indicating that only a fraction of total Cac channels are mobilized for AZ occupancy, and that this fraction is modulated depending on total Cac availability. To test whether *α2δ* controls the fraction of biosynthesized Cac destined for AZs, we tested whether *α2δ* overexpression can increase AZ Cac in the *cac^{GFP/Df}* heterozygous background. While *α2δ* overexpression resulted in elevated AZ Cac in control animals, it did not increase AZ Cac in the *cac^{GFP/Df}* deficiency background, indicating that overexpressed *α2δ* relies on the presence of a non-AZ Cac pool for its ability to enhance Cac abundance at AZs (**Figure 5K and L**). These data suggest that *α2δ* mediates Cac trafficking rather than channel stabilization. A forward trafficking role could facilitate progression through the biosynthetic pathway or long-range axonal transport. However, the severity of the Cac-depletion phenotype in *α2δ^{2/k10814}* mutants is independent of axon length, with distal (segments 5 and 6) and proximal (segments 1 and 2) abdominal segments displaying similar reductions in Cac compared to controls (**Figure 5—figure supplement 1D, E**). These data are consistent with a role for *α2δ* in mediating progression through the ER/Golgi pathway prior to long-range axonal transport. Imaging of endogenously tagged Cac-GFP following *α2δ* overexpression or reduction in 1st, 2nd, and 3rd instar animals demonstrated that *α2δ* becomes rate-limiting for AZ Cac over developmental time, with *α2δ* overexpression and *α2δ^{2/+}* heterozygote phenotypes appearing during the 3rd instar stage when a large majority of new AZs are forming. Similarly, the *α2δ^{2/k10814}* phenotype is present across all stages of larval development but becomes more severe in the 3rd instar stage, likely due to an increased demand for Cac trafficking and delivery as AZ number increases (**Figure 5M and N**). Together, these results demonstrate that *α2δ* plays a rate-limiting role in AZ Cac accumulation in a regulatory step upstream of AZ Cac delivery, and that the need for normal *α2δ* levels increases throughout developmental time as the number of AZs increases.

Similar to prior reports, a modest decrease in synapse area and AZ number was observed in the more severe *α2δ* reduction (*α2δ^{2/k10814}*), reflecting a role for *α2δ* in morphological development of the NMJ (**Figure 5—figure supplement 1A-C**; Kurshan et al., 2009). The requirements of *α2δ* in morphological development and Cac accumulation have been shown to represent independent functions of the subunit (Kurshan et al., 2009). That AZs and NMJs form normally in the absence of Cac channels (**Figure 1**), but abnormally in the *α2δ^{2/k10814}* mutant, supports the model that the morphological role

of $\alpha 2\delta$ is not downstream of its role in Cac localization. Moreover, unlike $\alpha 2\delta$'s requirement in Cac abundance, the morphological phenotype is not dosage-dependent, as $\alpha 2\delta^{2/+}$ heterozygotes were morphologically normal (**Figure 5—figure supplement 1**).

Cac delivery to AZs correlates with AZ size and is regulated by $\alpha 2\delta$

To establish a protocol to directly measure the delivery of new Cac channels, entire Ib NMJs innervating muscle 26 in late 2nd instar animals expressing endogenously tagged Cac-GFP and GluRIIA-RFP were photobleached and synapses were imaged immediately after photobleaching to confirm loss of the Cac-GFP signal (**Figure 6—figure supplement 1A**). Animals were then allowed to recover and grow for 24 hr before dissection. Fixed NMJs were imaged 24 hr post-bleach alongside unbleached NMJs as a control (**Figure 6—figure supplement 1B**). New synapse growth and new AZ addition (1.9-fold increase in AZ number) were observed after 24 hr of growth, as previously described (**Akbergenova et al., 2018; Figure 6—figure supplement 1C**). AZ ROIs were defined using unbleached GluRIIA-labeled PSDs. Total Cac signal inside each ROI was measured and averaged at AZs across the NMJ, demonstrating near-complete photobleaching and partial recovery of Cac-GFP signal 24 hr post-bleach, representing new Cac-GFP channels that arrived at NMJs after photobleaching (**Figure 6—figure supplement 1A, B, D**).

This FRAP protocol was used to measure Cac-GFP delivery over 24 hr in control and $\alpha 2\delta^{2/k10814}$ NMJs, and recovered Cac levels were correlated with post-fixation BRP immunostaining (**Figure 6A**). Cac delivery was broadly distributed across AZs of the NMJ, rather than targeted to a specific subset of AZs. In the span of 24 hr, 90% of AZs had received detectable new Cac-GFP channels (**Figure 6B**). New Cac-GFP signal was roughly 50% dimmer than unbleached Cac-GFP control AZs, consistent with prior demonstration that AZs grow to full structural and functional maturity over several days (**Akbergenova et al., 2018; Figure 6C**). To determine whether new channels were delivered preferentially to AZs based on AZ size or age, 24 hr delivery of CRISPR Cac-GFP was correlated with BRP abundance, an established correlate of AZ age and functional maturity (**Akbergenova et al., 2018**). In non-photobleached NMJs, Cac-GFP correlated highly with BRP abundance at individual AZs, with an average Pearson r of 0.88, consistent with prior studies (**Figure 6D and F; Akbergenova et al., 2018**). After 24 hr of new channel delivery post-photobleaching, Cac-GFP signal correlated similarly with BRP at AZs, indicating that a larger number of newly delivered channels were incorporated at mature AZs over a 24 hr period, and new delivery correlated with AZ size and maturity (**Figure 6E and F**). Twenty-four hour Cac delivery correlated similarly well with GluRIIA-RFP abundance, another established proxy for AZ age (**Figure 6—figure supplement 1E-G; Akbergenova et al., 2018**).

Cac levels in $\alpha 2\delta^{2/k10814}$ mutants in unbleached segments were reduced by roughly 70% at AZs, similar to the Cac reduction measured at muscle 4 (**Figure 6G, Figure 5A and B**). After 24 hr of recovery, $\alpha 2\delta^{2/k10814}$ mutants showed an ~50% reduction in Cac delivery compared to controls, with no change in AZ number, suggesting that $\alpha 2\delta$ is required for Cac delivery (**Figure 6H,I**). Although reduced, residual Cac delivery remained correlated with BRP abundance in $\alpha 2\delta^{2/k10814}$ mutants (**Figure 6J-L**). These data indicate that Cac delivery is regulated by $\alpha 2\delta$, is broadly available to AZs across the NMJ, and its incorporation positively correlates with AZ size and age.

Cac turnover contributes to setting AZ Cac abundance

The leveling-off of Cac accumulation at mature AZs despite continued delivery predicts that Cac turnover must occur. The efficiency of Cac surface retention and timecourse of VGCC removal from AZs has not been measured in any in vivo system to our knowledge. Additionally, the mechanism by which VGCC regulatory proteins promote Cac surface expression has remained unclear due to difficulties experimentally distinguishing Cac trafficking/delivery versus Cac turnover. To facilitate direct measurements of Cac removal from AZs, an endogenously tagged photoconvertible green-to-red Cac channel (Cac-Maple) was generated using CRISPR by inserting Maple onto the C-terminal region of Cac at the same location previously used for UAS-Cac-GFP (**Kawasaki et al., 2004**) and Cac-GFP^C (**Figure 3**). Cac-Maple localizes to AZs and is visible at all release sites, displaying normal heterogeneity across the AZ population. Prior to photoconversion, Cac-Maple is entirely green without any red signal. Upon exposure to 405 nm light, the protein completely and irreversibly photoconverts to red (**Figure 7—figure supplement 1A**). TEVC recordings demonstrated that Cac-Maple supports normal

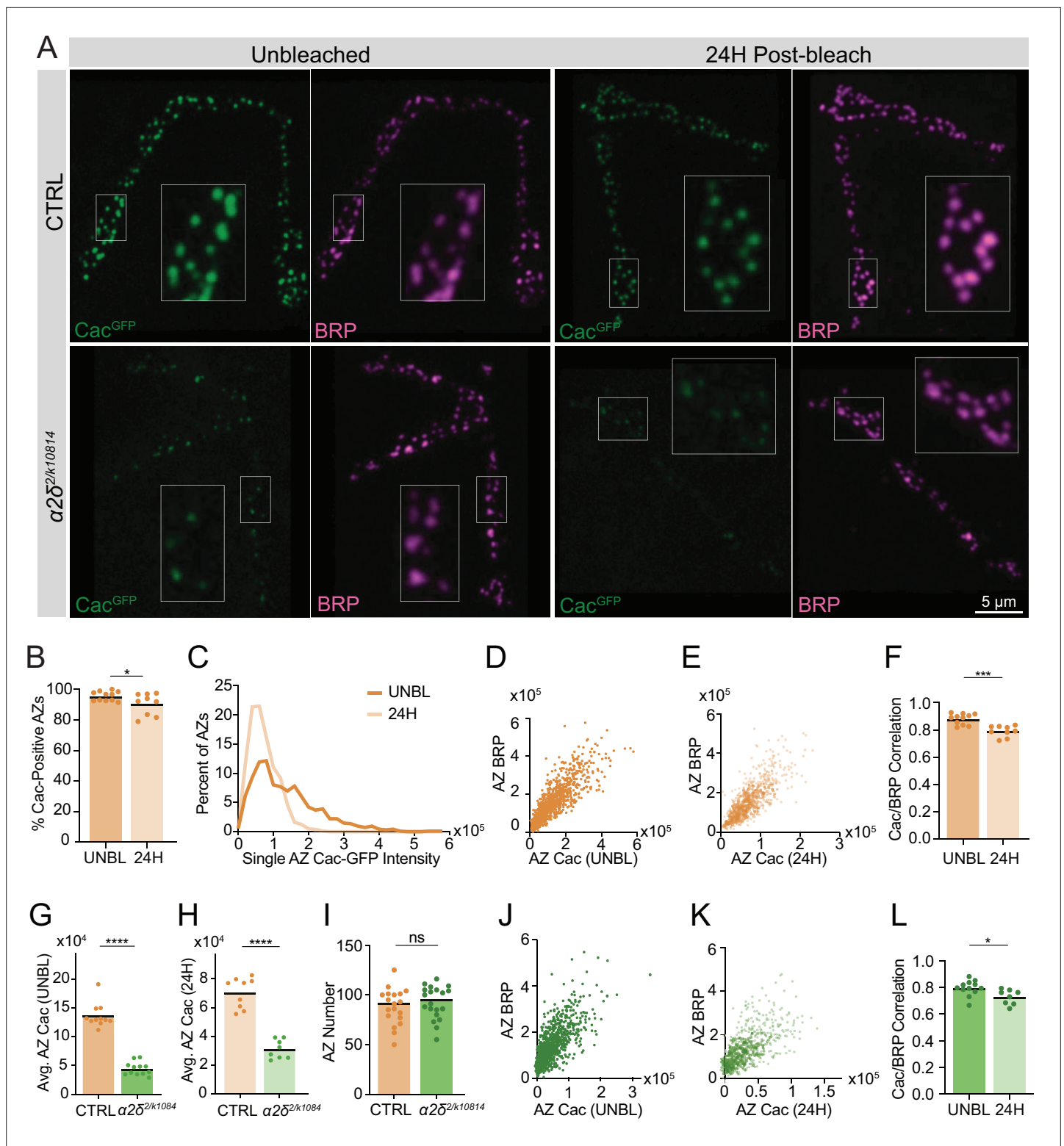


Figure 6. Cac delivery to active zones (AZs) correlates with AZ size and is regulated by $\alpha 2\delta$. **(A)** Representative images of FRAP experiments in CTRL (*cac^{GFP}*) and $\alpha 2\delta$ mutant (*cac^{GFP}; \alpha 2\delta^{2/k10814}*) neuromuscular junctions (NMJs). Fixed and Bruchpilot (BRP)-immunostained (magenta) NMJs are shown 24 hr post-bleaching, with unbleached NMJs as a control. Boutons inside white boxes are enlarged. **(B)** Percent of BRP-positive AZs with Cac-GFP max pixel intensity greater than 150% of average background fluorescence (pre: 95.56 ± 0.9347 ; 0H: 90.37 ± 2.347 , $p = 0.0422$). **(C)** Distribution of single AZ Cac-GFP intensity (sum Cac-GFP fluorescence within an ROI encompassing each BRP-positive AZ) in unbleached NMJs (UNBL) and 24 hr after bleaching (pre: $13,6052 \pm 3018$, $n = 946$ AZs; 24H: $72,261 \pm 1389$, $n = 804$ AZs). **(D, E)** Correlations of Cac-GFP and BRP at individual AZs in unbleached controls **(D)** and

Figure 6 continued on next page

Figure 6 continued

NMJs 24 hr post-bleach (E). (F) Pearson r value for the correlation of Cac-GFP and BRP intensity across the AZ population at each NMJ in unbleached control NMJs (UNBL) and 24 hr post-bleach (pre: 0.8801 ± 0.01191 ; 24H: 0.7913 ± 0.01348 , $p < 0.001$). (G) Average AZ Cac-GFP intensity in unbleached segments in cac^{GFP} and $\alpha 2\delta^{2/k10814}$ NMJs (cac^{GFP} : $136,462 \pm 6346$, $n = 11$ NMJs; $\alpha 2\delta^{2/k10814}$: $44,340 \pm 3252$, $n = 12$ NMJs, $p < 0.0001$). (H) Average AZ Cac-GFP intensity 24 hr post-bleach (cac^{GFP} : $70,528 \pm 3508$, $n = 9$ NMJs; $\alpha 2\delta^{2/k10814}$: $31,086 \pm 2326$, $n = 8$ NMJs, $p < 0.0001$). (I) AZ number at NMJs (cac^{GFP} : 88.26 ± 4.13 , $n = 19$ NMJs; $\alpha 2\delta^{2/k10814}$: 92.45 ± 3.689 , $n = 20$ NMJs). (J, K) Correlation of Cac-GFP and BRP at individual AZs in unbleached $\alpha 2\delta^{2/k10814}$ mutants (J) and $\alpha 2\delta^{2/k10814}$ NMJs 24 hr post-bleach (K). (L) Pearson r value for the correlation of Cac-GFP and BRP intensity across the AZ population in unbleached NMJs (UNBL) and NMJs 24 hr post-bleach in $\alpha 2\delta^{2/k10814}$ mutants (UNBL: 0.7952 ± 0.01635 ; 24H: 0.7285 ± 0.01955 , $p = 0.018$).

The online version of this article includes the following source data and figure supplement(s) for figure 6:

Source data 1. Source data for **Figure 6**.

Figure supplement 1. Photobleaching validation and GluRIIA correlations.

Figure supplement 1—source data 1. Source data for **Figure 6—figure supplement 1**.

evoked synaptic transmission both before and after photoconversion (**Figure 7—figure supplement 1B-E**).

Early 2nd instar cac^{Maple} larvae were photoconverted for a total of 60 s under a mercury lamp with a 405 nm filter and animals were dissected and imaged either 24 hr or 5 days post-conversion. Since Maple is brighter and more photostable in its red state, green BRP immunostaining was used to facilitate reliable AZ identification in experiments measuring red Cac-Maple decay across time. In animals 24 hr post-conversion, a majority of AZs were labeled with red Cac-Maple, with a minority of AZs lacking red signal (**Figure 7A**). This minority represents that AZs formed after the photoconverted pool was AZ-incorporated. In animals imaged 5 days post-conversion, the population of red-labeled AZs was present among a much larger population of green-only AZs, as expected given AZ number doubles daily during this period of NMJ growth (**Akbergenova et al., 2018; Figure 7A and B**). Occasionally, entire boutons or long inter-bouton spaces were completely devoid of red channels, representing parts of the NMJ that grew after photoconversion (**Figure 7A**, white arrow).

The red signal present at AZs 5 days post-conversion represents the fraction of remaining Cac-Maple channels that were either present at AZs at the time of conversion, or were photoconverted en route to AZs and incorporated shortly after conversion. To avoid drawing an arbitrary cutoff for 'zero' red signal, the measurement of Cac-Maple decay was performed at the brightest 30 AZs per NMJ (see Materials and methods). The average fluorescence intensity of photoconverted red Cac-Maple at these AZs (per NMJ) decayed by 28–30%, with a predicted Cac $T_{1/2}$ of 8 days at 18°C (**Figure 7C and D, Figure 7—figure supplement 1F**). The total number of red-labeled AZs did not change between day 1 and day 5 post-conversion, suggesting that Cac at AZs is stable and does not undergo lateral transfer between neighboring AZs (**Figure 7B**). Moreover, many bright red AZs were observed with neighboring AZs entirely lacking red Cac-Maple signal, further supporting the local stability of Cac at individual AZs (**Figure 7A**).

Cac turnover at AZs is abolished by reductions in either Cac or $\alpha 2\delta$ expression

To directly assay whether $\alpha 2\delta$ plays a role in facilitating Cac surface retention, we measured Cac-Maple turnover over 4 days in an $\alpha 2\delta^{2/+}$ heterozygous background ($cac^{Maple}; \alpha 2\delta^{2/+}$) and in the $\alpha 2\delta^{2/k10814}$ transheterozygote ($cac^{Maple}; \alpha 2\delta^{2/k10814}$). In control NMJs (cac^{Maple}), red Cac-Maple intensity diminished by 30% over the 4-day window (**Figure 7A, C and D**). However, measurable Cac turnover at AZs was eliminated in both $\alpha 2\delta^{2/+}$ and $\alpha 2\delta^{2/k10814}$ backgrounds, as red Cac-Maple intensity was unchanged at AZs on day 5 compared to day 1 (**Figure 7A and D**). The lack of turnover in $\alpha 2\delta$ reduction backgrounds indicates $\alpha 2\delta$ is not facilitating Cac abundance at AZs by promoting stabilization. In addition, it suggests that reduced levels of Cac delivery to AZs in these mutant backgrounds decreases Cac turnover. If Cac turnover is dependent on Cac delivery, then animals heterozygous for the Cac deficiency ($cac^{Maple/Df}$), which mildly reduced AZ Cac levels, should have reduced turnover when compared with a cac^{Maple} homozygous control. Unlike Cac in control AZs, which decayed by 30% over a 4-day window, Cac-Maple in the $cac^{Maple/Df}$ heterozygote did not show measurable levels of decay, phenocopying the $\alpha 2\delta$ reduction mutants and supporting a model in which Cac turnover depends on new Cac delivery to AZs (**Figure 7A and D**). The fact that reducing either $\alpha 2\delta$ or Cac abolishes Cac turnover demonstrates

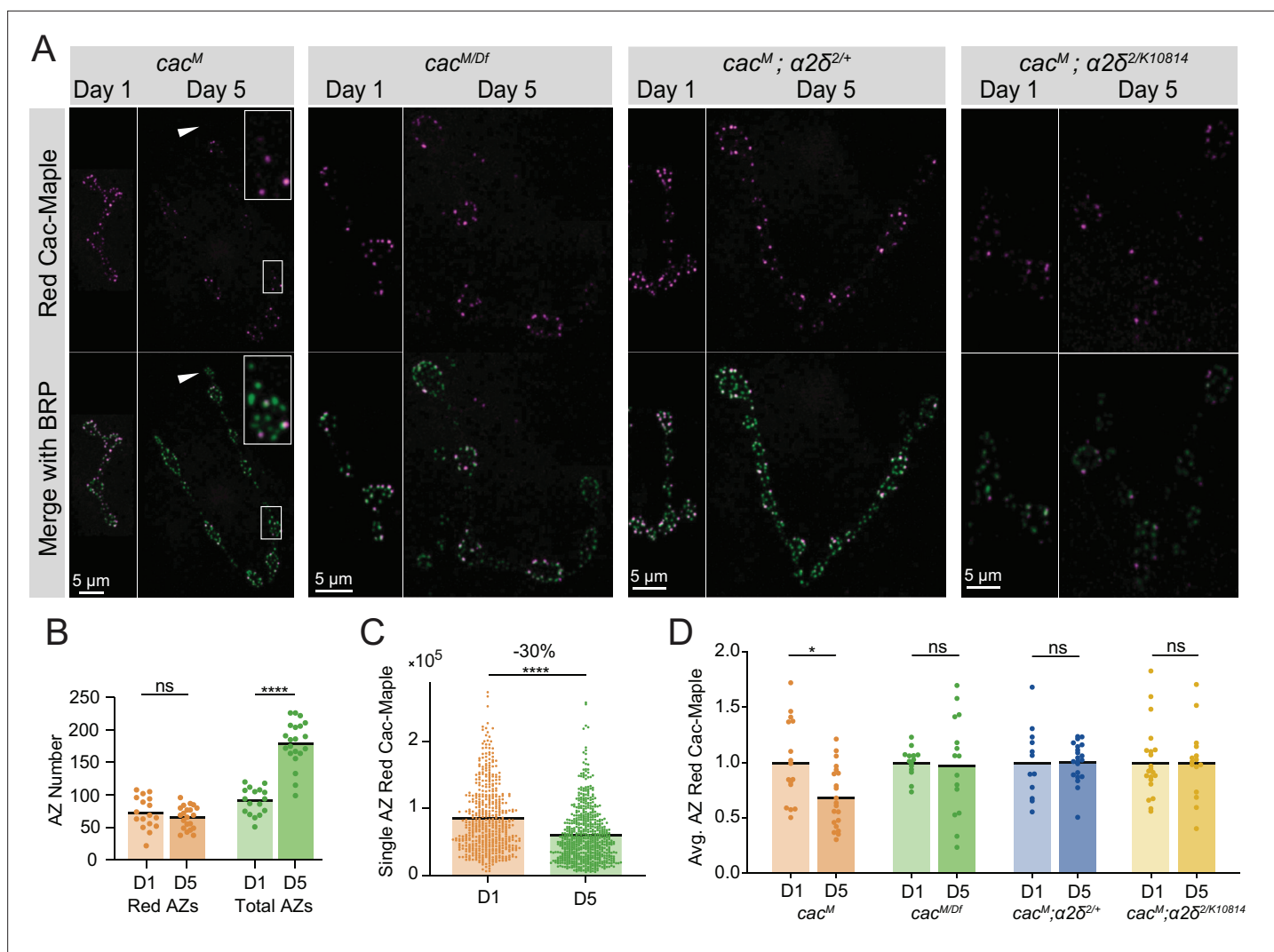


Figure 7. Cac turnover at active zones (AZs) is abolished by reductions in either Cac or $\alpha 2\delta$ expression. **(A)** Representative images of endogenously tagged photoconverted Cac-Maple (magenta) and Bruchpilot (BRP) (green, overlapping with green unconverted Cac-Maple for reliable AZ identification) in controls (*cac^M*), *cac^{M/Df}* heterozygotes, $\alpha 2\delta^{2/+}$ heterozygotes (*cac^M; \alpha 2\delta^{2/+}*), and $\alpha 2\delta^{2/K10814}$ mutants (*cac^M; \alpha 2\delta^{2/K10814}*) at 1 and 5 days after photoconversion. Boutons in white box are enlarged in control panel, and white arrows mark a bouton with no red Cac-Maple fluorescence. **(B)** Number of red-marked AZs (photoconverted Cac-Maple) and total AZs (identified using BRP immunostain) quantified 1 and 5 days post-conversion (red D1: 72.59 ± 5.921 , $n=17$ NMJs; red D5: 65.57 ± 3.789 , $n=21$ NMJs; total D1: 90.65 ± 4.948 ; total D5: 179.5 ± 7.502 , $p < 0.0001$). **(C)** Red Cac-Maple fluorescence at individual AZs (30 brightest AZs per NMJ pooled from 16 to 21 NMJs) at 1 and 5 days post-photoconversion. Percent reduction in brightness at day 5 compared to day 1 is shown above (day 1: $84,672 \pm 2258$, $n=502$ AZs; day 5: $59,383 \pm 1598$, $n=630$ AZs, $p < 0.0001$). **(D)** Average Cac-Maple fluorescence of the 30 brightest AZs per NMJ at indicated genotypes at 1 and 5 days post-conversion. For each genotype, average Cac-Maple intensity at day 1 was normalized to 1.0 (*Cac^M* D5: 0.6868 ± 0.05975 , $p=0.0103$; *cac^{M/Df}* D5: 0.9746 ± 0.1154 ; *Cac^M; \alpha 2\delta^{2/+}* D5: 1.006 ± 0.03891 ; *Cac^M; \alpha 2\delta^{2/K10814}* D5: 1 ± 0.08489).

The online version of this article includes the following source data and figure supplement(s) for figure 7:

Source data 1. Source data for **Figure 7**.

Figure supplement 1. Cac-Maple localizes to active zones (AZs), photoconverts fully, and has normal function.

Figure supplement 1—source data 1. Source data for **Figure 7—figure supplement 1**.

that turnover is driven by new delivery and that $\alpha 2\delta$ is required for Cac delivery. A minor secondary role for $\alpha 2\delta$ in stabilizing Cac at AZs cannot be completely ruled out due to the residual levels of $\alpha 2\delta$ remaining in these mutant backgrounds.

In a model where $\alpha 2\delta$ levels rate-limit Cac delivery to AZs and Cac is normally expressed in excess, Cac overexpression should not result in increased Cac delivery to AZs and Cac turnover should be unaffected by Cac overexpression. UAS-Cac-GFP overexpression using a pan-neuronal driver

(elav-GAL4) in the *cac*^{Maple} background did not alter Cac-Maple turnover rate despite a reduction in initial Cac-Maple abundance at AZs as expected from competition between the two pools (**Figure 7—figure supplement 1G, H**). These data further indicate that Cac overexpression does not increase Cac delivery to AZs, as suggested by imaging and electrophysiology described above (**Figure 3**). Together, these data indicate that Cac delivery to growing AZs drives Cac turnover, with $\alpha 2\delta$ promoting Cac delivery into AZs rather than facilitating Cac retention at release sites.

Discussion

In the present study, we used the *Drosophila* NMJ as a model synapse to characterize the flow of VGCCs into and out of AZs, probing the relationship between Cac, its conserved regulatory subunit $\alpha 2\delta$, and the AZ scaffold. Unlike extensive research that has been performed on the trafficking and retention of postsynaptic glutamate receptors at rest and during plasticity, much less is known about how the key engine of Ca^{2+} influx for presynaptic release, VGCCs, are delivered, accumulate, and recycle at AZs (*Rasse et al., 2005; Citri and Malenka, 2008; Hastings and Man, 2018*). Because of the steep dependence of SV fusion on Ca^{2+} influx and the high correlation between VGCC abundance and *P*, at individual AZs, understanding how VGCC abundance is established through delivery and turnover provides critical insights into how neurons regulate synaptic strength (*Akbergenova et al., 2018; Gratz et al., 2019; Augustine et al., 1985; Borst and Sakmann, 1996; Sheng et al., 2012*). In the current study, we find that Cac channels are not essential for AZ formation at *Drosophila* NMJs. We also demonstrate that AZs are buffered against moderate increases or decreases in Cac biosynthesis, in contrast to the lack of buffering for the AZ scaffold BRP. We find that Cac delivery to AZs occurs broadly across the AZ population, correlates with AZ size, and is regulated by $\alpha 2\delta$. Finally, we show that Cac recycling from AZs is promoted by new Cac delivery and counterbalances delivery at mature AZs to generate the observed upper limit on Cac accumulation at single release sites.

Despite the well-established requirement of VGCCs in synaptic function, whether they also promote AZ structural formation at *Drosophila* synapses has not been determined. Using single-neuron knockouts, we showed that the $\alpha 1$ subunit of the *Drosophila* VGCC Cac is dispensable for AZ formation and structural maturation. A recent study in mammalian neurons used a similar approach to demonstrate normal AZ number and structure despite conditional knockout of the entire *Ca_v2* family of VGCCs in cultured mouse hippocampal neurons and the Calyx of Held (*Held et al., 2020*). Many molecular components of the AZ are functionally conserved, but the broad variety of AZ architectures across species raises interesting questions about the similarity of AZ formation and maturation processes (*Zhai and Bellen, 2004*). The finding that AZ formation is independent of VGCCs at *Drosophila* NMJs and mammalian central synapses suggests that this is likely to be a conserved feature of neurons across evolution. While Cac is not essential for BRP accumulation at growing AZs, BRP plays an established role in promoting proper Cac clustering and accumulation (*Fouquet et al., 2009; Kittel et al., 2006*). However, whether BRP plays a rate-limiting role in regulating Cac abundance at the AZ is unclear. Here, we demonstrate that Cac AZ abundance is unaffected by a 36% reduction in AZ BRP (BRP heterozygote deficiency background) or by ~80% reduction in AZ BRP in the BRP-positive subset of AZs present following BRP RNAi knockdown (**Figure 4, Figure 4—figure supplement 1**). While it is possible that a subset of BRP proteins are post-translationally modified to rate-limit Cac accumulation at AZs, these findings suggest that BRP's presence or absence, rather than its abundance, controls whether AZs accrue normal levels of Cac.

Because the BRP/RBP AZ scaffold forms independent of Cac, we predicted that Cac accumulation at growing AZs is regulated independently from other AZ components. Many synaptic proteins co-traffic to the synaptic terminal, but VGCCs have not been identified on these transport vesicles (*Vukoja et al., 2018; Wu et al., 2013; Maas et al., 2012; Bury and Sabo, 2011; Maeder et al., 2014*). We focused on levels of the *Drosophila* CASK/ELKS homolog BRP as a representative AZ scaffold protein given *brp* mutants lack AZ T-bars and show a significant reduction in Cac and other key scaffolding proteins at release sites (*Kittel et al., 2006; Fouquet et al., 2009*). In long-lived larvae, we observed increased BRP enrichment at AZs and a leveling-off of Cac accumulation. This divergent trajectory of Cac and BRP accumulation over an extended developmental window suggests that the two proteins are independently regulated.

Manipulation of BRP biosynthesis revealed that BRP AZ abundance directly reflects its biosynthesis, consistent with observations that a mutant with increased AZ seeding (*endophilin*) and one with fewer

mature AZs (*rab3*) have opposite changes in AZ BRP abundance (Goel et al., 2019). In contrast to BRP, we found that AZ Cac levels do not reflect Cac biosynthesis. Moderate reductions in Cac biosynthesis do not result in comparable depletion of Cac at AZs, indicating that AZs are buffered against alterations in Cac transcription or translation. Kenyon cells in the *Drosophila* mushroom body maintain normal presynaptic release following weak Cac RNAi knockdown, but fail to potentiate presynaptic release during odor conditioning, suggesting that Cac buffering also occurs in the CNS and its biosynthesis may become rate-limiting during certain forms of presynaptic plasticity (Stahl et al., 2022). We also find that Cac overexpression fails to increase Cac abundance at AZs, indicating that Cac biosynthesis does not rate-limit AZ Cac accumulation and suggesting that competition between Cac channels for AZ localization. To visualize this competition directly, we overexpressed red-tagged UAS-Cac-tdTomato in the CRISPR Cac-GFP background and saw that red channels displace green channels from AZs. This competition between channels is supported by VGCC overexpression experiments in mammalian neurons that demonstrate overexpression of PQ channels with channelopathy mutations compete with wildtype channels for AZ localization, and that overexpressing the Ca_v2 α 1 subunit fails to increase Ca_v2 levels at AZs (Cao et al., 2004; Cao and Tsien, 2010; Hoppa et al., 2012).

The two major processes downstream of Cac biosynthesis that establish Cac AZ levels are Cac delivery to AZs and Cac stabilization once incorporated. However, the patterns and rate of Cac delivery to AZs have not been described in detail. We tested whether Cac delivery to AZs occurs in a targeted fashion (with delivery to a subset of AZs) or a population-wide manner (where all AZs within a terminal have continuous access to new channels throughout development). Quantification of Cac delivery at individual AZs revealed a majority of AZs receive new channels over 24 hr, but the levels of new Cac delivery were well below AZ Cac capacity, consistent with previous reports that AZs mature to high-releasing states over a period of several days (Rasse et al., 2005; Akbergenova et al., 2018). Because AZs level off their accumulation of Cac over developmental time, we expected to find reduced or halted Cac delivery at the most mature AZs. Surprisingly, the largest AZs continued to receive the most Cac, as delivery correlated highly with GluRIIA and BRP levels (two reliable correlates of AZ age and maturation state) across the entire AZ population (Akbergenova et al., 2018). We propose a model where new Cac channels are available to the entire AZ population rather than being targeted to a subset of AZs, and larger AZs incorporate more of the available channels than smaller AZs. This distribution of Cac delivery differs from postsynaptic glutamate receptor fields at the *Drosophila* NMJ, where new receptors are only added to growing PSDs, while PSDs that reach a mature state do not incorporate new receptors (Rasse et al., 2005).

If mature AZs level off in their Cac accumulation despite increasing levels of Cac delivery, Cac turnover must be occurring at mature AZs. VGCC turnover from the presynaptic membrane has not been measured in any in vivo system, leaving many open questions about both the inter-AZ mobility and stability of Cac channels, as well as their AZ resident time. We generated endogenously tagged green-to-red photoconvertible Cac-Maple to analyze resident time of endogenous Cac channels at AZs and found that roughly 30% of Cac channels are removed from AZs over 4 days at 18°C, suggesting an average half-life of 8 days under these conditions. This turnover was significantly reduced when the transcription of either Cac or the VGCC trafficking subunit α 2 δ were lowered, indicating that Cac turnover at AZs is promoted by new Cac delivery rather than Cac channels being removed from AZs with a set half-life. The lack of observed turnover in Cac and α 2 δ reduction backgrounds also indicates that Maple photobleaching is not responsible for the 30% reduction in red Cac-Maple signal measured in wildtype animals. These data support a model where Cac channels turn over at AZs more readily when Cac delivery approaches or exceeds Cac capacity, consistent with the idea that channels compete for spots at AZs, perhaps through limited stabilization by binding partners.

Cac channels could either be removed from AZs through degradation, or undergo lateral transfer and stabilization into nearby AZs. Though we cannot rule out that limited lateral transfer may occur below our limit of detection, two observations suggest lateral transfer is unlikely to be a main avenue of Cac loss from individual AZs. First, the number of red-labeled AZs remained constant over the 4-day window in photoconverted Cac-Maple larvae. If red-labeled Cac channels were drifting into nearby AZs, one would expect an increase in red-labeled AZs. Second, at 4 days post-photoconversion, brightly red-labeled AZs are typically surrounded by AZs with no detectable red signal, suggesting red-labeled Cac does not drift between neighboring AZs during this developmental window. Consistent with this model, new studies using mEOS tagging to track the motion of individual Cac channels revealed a

high degree of Cac mobility within individual AZs, but no significant lateral diffusion between AZs (Ghelani et al., 2022). This observation parallels findings from the postsynaptic compartment, where new glutamate receptor fields form via new delivery instead of splitting from existing receptor fields (Rasse et al., 2005).

The ability to separately measure Cac delivery and turnover provides new approaches to understand how VGCC regulatory proteins control synaptic abundance of Cac. Here, we focused on $\alpha 2\delta$ – a conserved VGCC subunit and a target of the commonly prescribed drugs pregabalin and gabapentin (Dolphin, 2016; Dickman et al., 2008; Hoppa et al., 2012; Eroglu et al., 2009). $\alpha 2\delta$'s canonical and highly conserved role is to promote surface expression of the VGCC's pore-forming $\alpha 1$ subunit (Hoppa et al., 2012; Saheki and Bargmann, 2009; Cassidy et al., 2014; Dickman et al., 2008; Ly et al., 2008). Indeed, we observed that $\alpha 2\delta$ is required for AZ Cac abundance in a dosage-sensitive manner. While Cac overexpression failed to increase Cac abundance at AZs, $\alpha 2\delta$ overexpression was sufficient to shift the AZ population toward higher Cac abundance without increasing Cac at the most mature AZs. $\alpha 2\delta$ is thought to facilitate VGCC surface expression through promoting forward trafficking rather than inhibiting AZ retention. Our data provides new support for this forward trafficking model. First, $\alpha 2\delta$ overexpression cannot drive increased AZ Cac levels without excess Cac translation, indicating that $\alpha 2\delta$ is required between translation and AZ delivery, rather than via a post-delivery mechanism. Second, $\alpha 2\delta$ mutants show reduced Cac delivery but increased Cac stability. A well-described VGCC-independent role of $\alpha 2\delta$ is to promote synapse formation (Kurshan et al., 2009). Our data support a model that $\alpha 2\delta$'s role in synapse formation is independent of VGCC localization, as neurons form AZs and grow at a normal rate in the absence of VGCCs, but severe reductions in $\alpha 2\delta$ cause a reduction in synaptic growth and AZ formation.

In summary, these data provide a model of Cac regulation in which Cac abundance at AZs is buffered against moderate alterations in Cac biosynthesis and Cac accumulation is rate-limited by $\alpha 2\delta$ -mediated trafficking (Figure 8A). Cac incorporation into AZs correlates with AZ size, and new delivery promotes Cac turnover at mature AZs, allowing AZ Cac accumulation to level off after several days of development. Our findings indicate that VGCC abundance at AZs reaches a capacity limit, similar to the previously proposed 'slot' model (Cao et al., 2004). Future work is needed to identify the molecular basis for this limited capacity and where excess VGCCs reside within the neuron. In addition to AZ-localized Cac, immobile puncta of endogenously tagged Cac-GFP are enriched in axon bundles proximal to the ventral nerve cord (VNC; Figure 8B). Following Cac-GFP overexpression, VNC-proximal axonal regions show a roughly 40 μm long area of Cac-GFP enrichment, beginning approximately 25 μm from the soma, likely corresponding to the distal axon segment, an invertebrate parallel to the axon initial segment (AIS) in mammals, defined by enrichment for the para sodium channel (Ravenscroft et al., 2020; Figure 8C). It is unknown whether this Cac population has a functional role in the distal axon segment, or may instead represent an excess pool of the protein that is available for AZ delivery following mobilization. Clarifying the localization and regulation of non-synaptic Cac channels may also provide insight into plasticity mechanisms, since the abundance of Cac and other AZ proteins are reported to change during short- and long-term plasticity at *Drosophila* NMJs (Gaviño et al., 2015; Gratz et al., 2019; Böhme et al., 2019; Hong et al., 2020). Future studies should reveal additional molecular mechanisms that mediate bulk flow of VGCCs to and from AZs, as well as how these processes can dynamically change during synaptic plasticity.

Materials and methods

Drosophila stocks

Flies were cultured on standard medium and maintained at 18–25°C. Late 3rd instar larvae were used for imaging and electrophysiological experiments unless otherwise noted. Western blots were performed on adult brain extracts. For experiments performed in homozygous *cac*^{Maple} and *cac*^{GFP} backgrounds, males were used to simplify genetic crosses unless otherwise noted. Experiments were performed in a *w*¹¹¹⁸ (BCSC #3605) genetic background unless otherwise noted. Fluorescently tagged Cac lines include N-terminally CRISPR-tagged Cac-GFP^N (referred to in text as Cac-GFP; Gratz et al., 2019); Cac-GFP^C (C-terminally CRISPR tagged, this study); Cac-Maple (C-terminally CRISPR tagged, this study); UAS-Cac-GFP (Kawasaki et al., 2004); and UAS-Cac-tdTomato (provided by Richard Ordway). A Cac deficiency (*cac*^{Df}; BDSC #9171; Ryder et al., 2007) was used to generate Cac heterozygotes.

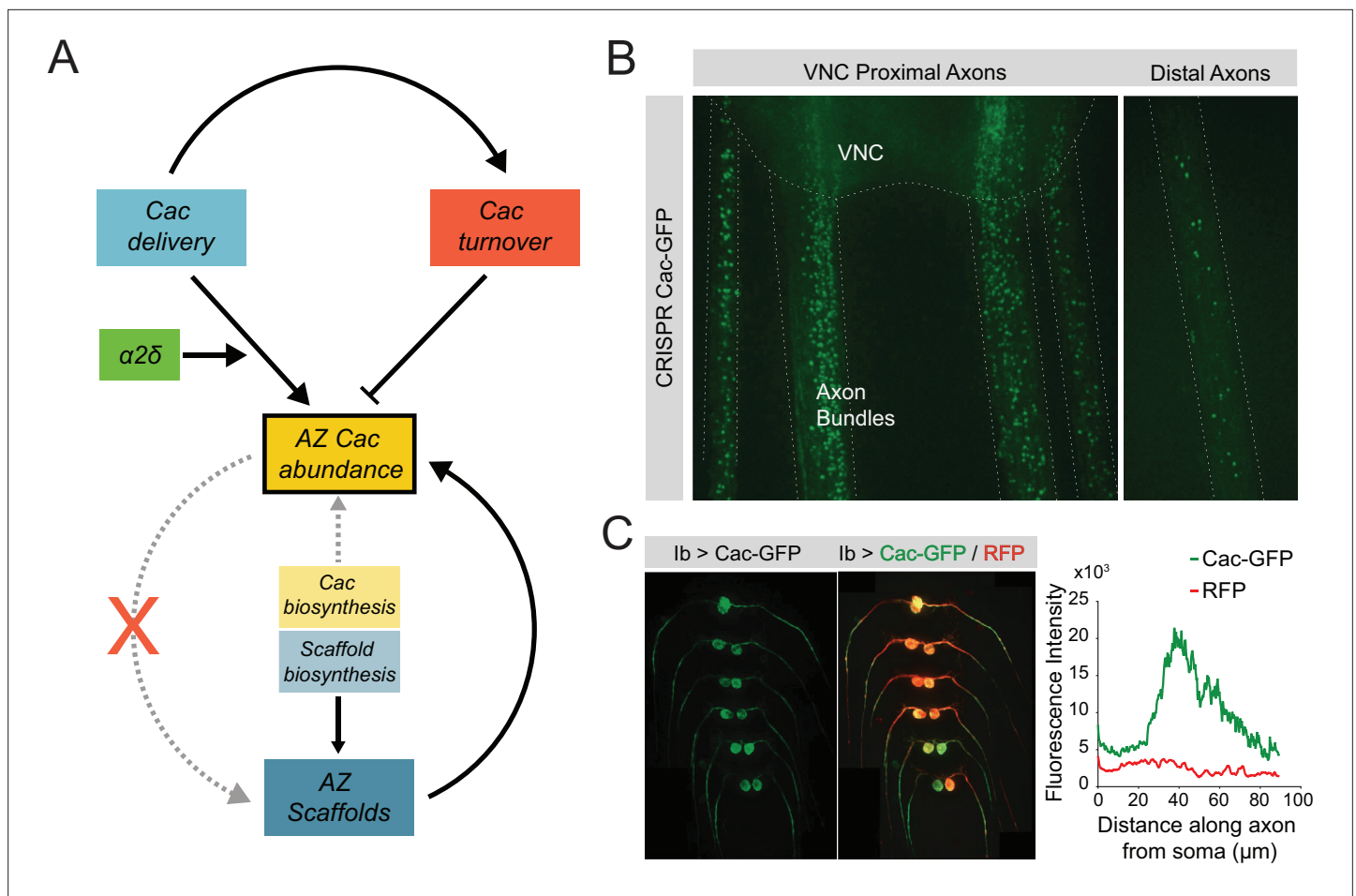


Figure 8. Model of Cac and active zone (AZ) scaffold regulation at the *Drosophila* neuromuscular junction (NMJ). **(A)** AZ Cac abundance (yellow box) is regulated by both new Cac delivery (blue box) and Cac turnover from AZs (red box). Cac delivery is positively regulated by $\alpha 2\delta$, and new delivery promotes turnover of existing channels. Cac biosynthesis (light yellow box) weakly regulates AZ Cac abundance, as AZ abundance is buffered against moderate changes in biosynthesis. In contrast, scaffold biosynthesis is a strong regulator of AZ scaffold abundance. The dependence relationship between AZ Cac abundance and AZ scaffold abundance is unidirectional: AZ scaffolds regulate Cac accumulation, but Cac is dispensable for AZ scaffold formation. **(B)** Left – representative image of endogenously tagged Cac-GFP puncta in axon bundles proximal to the ventral nerve cord (VNC). Right – representative image of Cac-GFP in distal axons. These axon puncta are immobile over a period of 30 min. **(C)** Left – representative image of a VNC with Cac-GFP (green) and RFP (red) expressed exclusively in MN1-Ib neurons. Right – quantification of Cac-GFP and RFP signal intensity as a function of distance along the axon from the soma. Plotted signal intensity was averaged across eight axons. RFP intensity is constant throughout the first 100 μm , while Cac-GFP intensity is elevated in the 30–60 μm range.

For single-neuron Cac knockout experiments, the Ib-specific Gal4 driver GMR94G06 (BDSC #40701) was used to drive UAS-FLP (BDSC #4539) in the *cac^{fp,nd}* background (BDSC #67681; **Fisher et al., 2017**). Long-lived larval experiments were performed using one copy of *phm-Gal4* and one copy of UAS-*torso-RNAi* (**Rewitz et al., 2009; Miller et al., 2012**). BRP mutants and RNAi constructs used for this study include *brp⁶⁹* (provided by Stephan Sigrist), *brp^{Df}*, and *BRP RNAi* (provided by Ethan Graf). $\alpha 2\delta$ (straightjacket) mutants and constructs used for this study include *stj²* (BDSC #39715); *stj^{k10814}* (BDSC #11004), and UAS-*Stj* (FlyORF F001495). PSD labeling for intravital FRAP experiments was performed using GluRIIA-RFP inserted onto chromosome III under the control of its endogenous promoter (provided by Stephan Sigrist). Pan-neuronal expression was performed using *elav^{C155}-GAL4* (BDSC #8765).

Generation of CRISPR-tagged Ca²⁺ channel lines

Two endogenously C terminally tagged Cac lines (Cac-GFP^C and Cac-Maple) were generated in this study using the same CRISPR genome engineering approach. One guide RNA (

CGAGGGTTCAGACCACTCTT) was chosen using the CRISPR Optimal Target Finder (*Gratz et al., 2014*) and inserted twice into the pCFD4 expression vector (Addgene #49411, *Port et al., 2014*) using the Gibson assembly protocol and NEBuilder HighFidelityDNA Assembly Cloning Kit (E5520). Donor template constructs were generating using Gibson assembly. Donor templates encode one Kb 5' and 3' homology arms flanking the 3' end of the *cac* coding region; these arms were generated through PCR amplification from the *Drosophila* genome. The 5' homology arm was mutated at the gRNA-binding site using silent mutations that do not alter the amino acid sequence (mutated to CGAGGGTTCAGACctgatTT). DNA encoding the fluorescent tag (either GFP or Maple) was inserted between the homology arms and flanked by the restriction sites EcoRI and XbaI. The tag was inserted immediately before the stop codon, with the same tagging location and GFP identity previously used to generate UAS-Cac-GFP (*Kawasaki et al., 2004*). A portion of the pCFD4 vector was linearized using PCR (forward primer: caattgtgctcggaacagt; reverse primer: caattgatcggctaattggtatg) and used as a backbone sequence for the donor template plasmid. gRNA and template plasmids were co-injected into *yw;;nos-Cas9(III-attP2)* embryos by BestGene Inc (Chino Hills, CA). PCR was used to screen progeny of injected animals for presence of the fluorescent tag. The modified locus was confirmed by sequencing.

Immunocytochemistry

Larvae were dissected in HL3 solution and fixed in 4% paraformaldehyde for 10 min, washed in Ca²⁺-free HL3, and blocked in 5% normal goat serum and 5% BSA in PBT for 15 min. Samples were incubated overnight at 25°C in blocking solution containing primary antibodies, and then washed for 1 hr in blocking solution. Samples were incubated for 1–2 hr at room temperature in blocking solution containing fluorophore-conjugated secondary antibodies. Primary antibodies used in this study were mouse anti-BRP at 1:500 (Nc82 DSHB, Iowa City, IA), rabbit anti-RBP at 1:500 (provided by Stephan Sigrist), mouse anti-SYX1 at 1:100 (8C3; DSHB), rabbit anti-GluRIII at 1:500 (*Marrus et al., 2004*), and anti-CPX at 1:500 (*Huntwork and Littleton, 2007*). Secondary antibodies used in this study were goat anti-mouse Alexa Fluor 607-, 546-, or 488-conjugated anti-mouse IgG at 1:5000 (Invitrogen, #s A21237, A11030, and A32723) and goat anti-rabbit Alexa Fluor 488-conjugated IgG at 1:5000 (A-11008; ThermoFisher). For HRP staining, samples were incubated in DyLight 649-conjugated HRP at 1:500 (#123-605-021; Jackson Immuno Research, West Grove, PA). Samples were mounted in Vectashield (Vector Laboratories, Burlingame, CA). For Cac Flpstop experiments, red tdTomato reporter fluorescence was completely abolished by fixation in 4% paraformaldehyde, allowing other proteins to be immunostained and imaged post-fixation in the red channel.

Cac-Maple photoconversion and analysis

To photoconvert larvae, early 2nd instar animals were placed on a glass slide in a thin film of halo-carbon oil to prevent drying. Animals freely crawled for three 20 s intervals under a mercury lamp with a 405 nm filter. After photoconversion, animals were placed in chambers with food in an 18°C incubator and were kept in the dark to prevent photobleaching from ambient light. Animals were dissected and stained with anti-BRP with Alexa Fluor 488-conjugated secondary antibody, and imaged under oil immersion. The sum fluorescence of red Cac-Maple signal within ROIs drawn manually to encompass the entire red-positive AZ area was determined. For each AZ ROI, mean single-pixel background fluorescence was multiplied by ROI pixel number and subtracted. The 30 AZs per NMJ with the brightest red Cac-Maple signal were analyzed to avoid AZs near the lower brightness limit of detection. Analysis on control animals selecting the top 10, 20, or 30 brightest AZs demonstrates the number of brightest AZs analyzed did not affect turnover measurements (*Figure 7—figure supplement 1F*).

Confocal imaging and imaging data analysis

Confocal images were acquired using a Zeiss Axio Imager 2 with a spinning-disk confocal head (CSU-X1; Yokagawa) and Imagem X2 EM-CCD camera (Hamamatsu). An Olympus LUMFL N 60× objective with a 1.10 NA was used for live imaging, and a Zeiss pan-APOCHROMAT 63× objective with 1.40 NA was used for imaging stained or intravital mounted animals. A 3D image stack was acquired for each NMJ imaged. Image analysis was performed in Volocity 3D Image Analysis software (PerkinElmer) and 3D stack images were merged into a single plane for 2D analysis. Analysis of Cac, BRP, RBP, and GluRIIA intensities were performed by first identifying AZ position using the 'find spot' algorithm in

Volocity 3.2 software that detects fluorescent peaks, and AZs were manually added in cases where the algorithm missed an AZ. ROIs were automatically generated by the software from identified spots and max pixel intensity or sum pixel intensity within the AZ ROI was reported as noted in figure legends. Background fluorescence was measured using the mean pixel intensity of background (non-NMJ) areas within merged images and background was subtracted from AZ fluorescent measurements. HRP area measurements were performed using the 'find object' algorithm in Volocity 3.2 software that creates an ROI around the HRP-positive area.

Live intravital imaging and photobleaching

Larvae were anesthetized with SUPRANE (desflurane, USP) from Amerinet Choice (Zhang *et al.*, 2010). Larvae were placed on a glass coverslide in a thin film of halocarbon oil to prevent drying and incubated under a glass jar with a small cotton ball soaked in Suprane for 40 s in a fume hood. For imaging, anesthetized larvae were covered in halocarbon oil and positioned ventral side up on a glass slide between spacers made by clay, compressed moderately, and covered with a cover glass. NMJs on muscle 26 in hemi-segment A2 or A3 were imaged. For photobleaching experiments, NMJs were imaged continuously with 80% laser power and 1 s exposure for 90 s until green fluorescent signal was no longer visible. After an imaging session, larvae were placed in individual Eppendorf tubes with food in a 25°C incubator and were wrapped in aluminum foil to prevent photobleaching by ambient light in the room. Animals that did not recover within 5 min of unmounting were excluded from further analysis. The same data acquisition settings were used to visualize NMJs at different larval stages. To facilitate easier visual comparison between developmental time periods, images of the corresponding NMJ area at younger stages were cut, rotated when necessary, and placed onto a black background for figure presentation.

TEVC electrophysiology

Postsynaptic currents were recorded using TEVC with a -80 mV holding potential. Experiments were performed in room temperature HL3.1 saline solution (in mM, 70 NaCl, 5 KCl, 10 NaHCO₃, 4 MgCl₂, 5 trehalose, 115 sucrose, 5 HEPES, pH 7.18) as previously described (Jorquera *et al.*, 2012). Final [Ca²⁺] was adjusted to 0.3 mM unless otherwise noted. Recordings were performed in 3rd instar larvae at muscle 1 of segments A3 and A4 (for Cac knockout experiments) and at muscle 6 of segment A4 (for all other experiments). Motor axon bundles were cut and suctioned into a glass electrode and action potentials were stimulated at 0.33 Hz (unless indicated) using a programmable stimulator (Master8, AMPI; Jerusalem, Israel). Data acquisition and analysis was performed using Axoscope 9.0 and Clampfit 9.0 software (Molecular Devices, Sunnyvale, CA) and inward currents are labeled on a reverse axis.

Western blot analysis

Adult head lysates were prepared by freezing whole flies in liquid nitrogen in Eppendorf tubes and vortexing briefly to mechanically separate heads from bodies. Heads were sorted on a cold glass slide and five heads per sample were placed into loading buffer (2× Laemmli buffer with 1 M DTT) and homogenized. After centrifugation, supernatant was diluted into water for a final concentration of 1× Laemmli buffer and one head per 10 μl of sample. Western blotting was performed using standard laboratory procedures with mouse anti-SYX1 at 1:1000 (8C3; DSHB), mouse anti-BRP at 1:5000 (NC82; DSHB), rabbit anti-GFP at 1:5000 (ab6556; Abcam, Cambridge, UK) and mouse anti-Tubulin at 1:1,000,000 (Sigma; T5168). IRDye 680LT-conjugated goat anti-mouse at 1:5000 (LICOR; 926-68020) and IRDye 800CW-conjugated goat anti-rabbit at 1:5000 were used as secondary antibodies. A LI-COR Odyssey Imaging System (LI-COR Biosciences, Lincoln, MA) was used for visualization and analysis was performed using FIJI image analysis software (Schindelin *et al.*, 2012). Lanes with damaged spots on the membrane that prevented reliable quantification were excluded from analysis.

Statistical analysis

Statistical analysis and plot generation were performed using GraphPad Prism (San Diego, CA). The plot function in MATLAB R2020A (MathWorks, Natick, MA) was used to generate average electrophysiological traces. For comparisons of three or more groups of data, one-way ANOVA followed by Šidák's or Dunnett's multiple comparisons test was used to determine significance. For comparisons

of two groups, Student's t-test was used. The mean of each distribution is plotted in figures with individual datapoints also shown. Figure legends report mean \pm SEM, and n. Asterisks indicate the following p-values: *, $p \leq 0.05$; **, $p \leq 0.01$; ***, $p \leq 0.001$; ****, $p \leq 0.0001$. Pearson coefficient of correlation was calculated in GraphPad Prism using the following parameters: two-tailed p value and 95% confidence interval.

Acknowledgements

This work was supported by NIH grants MH104536 and NS117588 to JTL. KLC was supported in part by NIH pre-doctoral training grant T32GM007287. We thank the Bloomington *Drosophila* Stock Center (NIH P40OD018537), the Developmental Studies Hybridoma Bank, Ethan Graf (Amherst University), Gerald Rubin (Janelia Research Campus), Kate O'Connor-Giles (Brown University), Richard Ordway (Penn State University), Barry Ganetzky (University of Wisconsin), and Stephan Sigrist (Freie Universitat Berlin) for providing *Drosophila* strains and antibodies, Dina Volfson for cloning assistance, Ellen Hill for help with Western data acquisition, and members of the Littleton lab for helpful discussions and comments on the manuscript.

Additional information

Funding

Funder	Grant reference number	Author
National Institute of Mental Health	MH104536	J Troy Littleton
National Institute of Neurological Disorders and Stroke	NS117588	J Troy Littleton
National Institutes of Health	T32GM007287	Karen L Cunningham

The funders had no role in study design, data collection and interpretation, or the decision to submit the work for publication.

Author contributions

Karen L Cunningham, Conceptualization, Data curation, Formal analysis, Investigation, Methodology, Writing - original draft, Writing - review and editing; Chad W Sauvola, Data curation, Formal analysis; Sara Taviana, Data curation; J Troy Littleton, Conceptualization, Supervision, Funding acquisition, Writing - original draft, Project administration, Writing - review and editing

Author ORCIDs

Karen L Cunningham  <http://orcid.org/0000-0002-7738-0318>

J Troy Littleton  <http://orcid.org/0000-0001-5576-2887>

Decision letter and Author response

Decision letter <https://doi.org/10.7554/eLife.78648.sa1>

Author response <https://doi.org/10.7554/eLife.78648.sa2>

Additional files

Supplementary files

- Transparent reporting form

Data availability

All data generated or analyzed during this study are included in the manuscript and supporting file; Source Data files have been provided for Figures 1 to 7.

References

- Acuna C**, Liu X, Südhof TC. 2016. How to make an active zone: Unexpected universal functional redundancy between rims and RIM-bps. *Neuron* **91**:792–807. DOI: <https://doi.org/10.1016/j.neuron.2016.07.042>
- Akbergenova Y**, Cunningham KL, Zhang YV, Weiss S, Littleton JT. 2018. Characterization of developmental and molecular factors underlying release heterogeneity at *Drosophila* synapses. *eLife* **7**:e38268. DOI: <https://doi.org/10.7554/eLife.38268>
- Aponte-Santiago NA**, Ormerod KG, Akbergenova Y, Littleton JT. 2020. Synaptic plasticity induced by differential manipulation of tonic and phasic motoneurons in *Drosophila*. *J Neuroscience* **40**:6270–6288. DOI: <https://doi.org/10.1523/JNEUROSCI.0925-20.2020>
- Ariel P**, Hoppa MB, Ryan TA. 2012. Intrinsic variability in Pv, RRP size, Ca(2+) channel repertoire, and presynaptic potentiation in individual synaptic boutons. *Frontiers in Synaptic Neuroscience* **4**:9. DOI: <https://doi.org/10.3389/fnsyn.2012.00009>
- Atwood HL**, Karunanithi S. 2002. Diversification of synaptic strength: presynaptic elements. *Nature Reviews. Neuroscience* **3**:497–516. DOI: <https://doi.org/10.1038/nrn876>
- Augustine GJ**, Charlton MP, Smith SJ. 1985. Calcium entry and transmitter release at voltage-clamped nerve terminals of squid. *The Journal of Physiology* **367**:163–181. DOI: <https://doi.org/10.1113/jphysiol.1985.sp015819>, PMID: 2865362
- Böhme MA**, McCarthy AW, Grasskamp AT, Beuschel CB, Goel P, Jusyte M, Laber D, Huang S, Rey U, Petzoldt AG, Lehmann M, Göttfert F, Haghghi P, Hell SW, Oswald D, Dickman D, Sigrist SJ, Walter AM. 2019. Rapid active zone remodeling consolidates presynaptic potentiation. *Nature Communications* **10**:1085. DOI: <https://doi.org/10.1038/s41467-019-08977-6>, PMID: 30842428
- Borst JG**, Sakmann B. 1996. Calcium influx and transmitter release in a fast CNS synapse. *Nature* **383**:431–434. DOI: <https://doi.org/10.1038/383431a0>, PMID: 8837774
- Branco T**, Staras K. 2009. The probability of neurotransmitter release: variability and feedback control at single synapses. *Nature Reviews. Neuroscience* **10**:373–383. DOI: <https://doi.org/10.1038/nrn2634>, PMID: 19377502
- Brusich DJ**, Spring AM, James TD, Yeates CJ, Helms TH, Frank CA. 2018. *Drosophila* CaV2 channels harboring human migraine mutations cause synapse hyperexcitability that can be suppressed by inhibition of a Ca2+ store release pathway. *PLOS Genetics* **14**:e1007577. DOI: <https://doi.org/10.1371/journal.pgen.1007577>, PMID: 30080864
- Bucurenciu I**, Kulik A, Schwaller B, Frotscher M, Jonas P. 2008. Nanodomain coupling between Ca2+ channels and Ca2+ sensors promotes fast and efficient transmitter release at a cortical GABAergic synapse. *Neuron* **57**:536–545. DOI: <https://doi.org/10.1016/j.neuron.2007.12.026>, PMID: 18304483
- Bury LAD**, Sabo SL. 2011. Coordinated trafficking of synaptic vesicle and active zone proteins prior to synapse formation. *Neural Development* **6**:24. DOI: <https://doi.org/10.1186/1749-8104-6-24>, PMID: 21569270
- Cao YQ**, Piedras-Rentería ES, Smith GB, Chen G, Harata NC, Tsien RW. 2004. Presynaptic Ca2+ channels compete for channel type-preferring slots in altered neurotransmission arising from Ca2+ channelopathy. *Neuron* **43**:387–400. DOI: <https://doi.org/10.1016/j.neuron.2004.07.014>, PMID: 15294146
- Cao YQ**, Tsien RW. 2005. Effects of familial hemiplegic migraine type 1 mutations on neuronal P/Q-type Ca2+ channel activity and inhibitory synaptic transmission. *PNAS* **102**:2590–2595. DOI: <https://doi.org/10.1073/pnas.0409896102>, PMID: 15699344
- Cao YQ**, Tsien RW. 2010. Different relationship of N- and P/Q-type Ca2+ channels to channel-interacting slots in controlling neurotransmission at cultured hippocampal synapses. *The Journal of Neuroscience* **30**:4536–4546. DOI: <https://doi.org/10.1523/JNEUROSCI.5161-09.2010>, PMID: 20357104
- Cassidy JS**, Ferron L, Kadurin I, Pratt WS, Dolphin AC. 2014. Functional exofacially tagged N-type calcium channels elucidate the interaction with auxiliary $\alpha 2\delta$ -1 subunits. *PNAS* **111**:8979–8984. DOI: <https://doi.org/10.1073/pnas.1403731111>, PMID: 24889613
- Catterall WA**, Few AP. 2008. Calcium channel regulation and presynaptic plasticity. *Neuron* **59**:882–901. DOI: <https://doi.org/10.1016/j.neuron.2008.09.005>, PMID: 18817729
- Chen Z**, Das B, Nakamura Y, DiGregorio DA, Young SM. 2015. Ca2+ channel to synaptic vesicle distance accounts for the readily releasable pool kinetics at a functionally mature auditory synapse. *The Journal of Neuroscience* **35**:2083–2100. DOI: <https://doi.org/10.1523/JNEUROSCI.2753-14.2015>, PMID: 25653365
- Citri A**, Malenka RC. 2008. Synaptic plasticity: multiple forms, functions, and mechanisms. *Neuropsychopharmacology* **33**:18–41. DOI: <https://doi.org/10.1038/sj.npp.1301559>, PMID: 17728696
- Dickman DK**, Kurshan PT, Schwarz TL. 2008. Mutations in a *Drosophila* alpha2delta voltage-gated calcium channel subunit reveal a crucial synaptic function. *The Journal of Neuroscience* **28**:31–38. DOI: <https://doi.org/10.1523/JNEUROSCI.4498-07.2008>, PMID: 18171920
- Dolphin AC**. 2016. Voltage-gated calcium channels and their auxiliary subunits: physiology and pathophysiology and pharmacology. *The Journal of Physiology* **594**:5369–5390. DOI: <https://doi.org/10.1113/JP272262>, PMID: 27273705
- Eggermann E**, Bucurenciu I, Goswami SP, Jonas P. 2011. Channels and sensors of exocytosis at fast mammalian synapses. *Nature Reviews. Neuroscience* **13**:7–21. DOI: <https://doi.org/10.1038/nrn3125>, PMID: 22183436
- Eroglu C**, Allen NJ, Susman MW, O'Rourke NA, Park CY, Ozkan E, Chakraborty C, Mulinyawe SB, Annis DS, Huberman AD, Green EM, Lawler J, Dolmetsch R, Garcia KC, Smith SJ, Luo ZD, Rosenthal A, Mosher DF, Barres BA. 2009. Gabapentin receptor alpha2delta-1 is a neuronal thrombospondin receptor responsible for

- excitatory CNS synaptogenesis. *Cell* **139**:380–392. DOI: <https://doi.org/10.1016/j.cell.2009.09.025>, PMID: 19818485
- Fisher YE, Yang HH, Isaacman-Beck J, Xie M, Gohl DM, Clandinin TR. 2017. FlpStop, a tool for conditional gene control in *Drosophila*. *eLife* **6**:e22279. DOI: <https://doi.org/10.7554/eLife.22279>, PMID: 28211790
- Fouquet W, Oswald D, Wichmann C, Mertel S, Depner H, Dyba M, Hallermann S, Kittel RJ, Eimer S, Sigrist SJ. 2009. Maturation of active zone assembly by *Drosophila* Bruchpilot. *The Journal of Cell Biology* **186**:129–145. DOI: <https://doi.org/10.1083/jcb.200812150>, PMID: 19596851
- Gaviño MA, Ford KJ, Archila S, Davis GW. 2015. Homeostatic synaptic depression is achieved through a regulated decrease in presynaptic calcium channel abundance. *eLife* **4**:eLife . DOI: <https://doi.org/10.7554/eLife.05473>, PMID: 25884248
- Ghelani T, Escher M, Thomas U, Esch K, Lützkendorf J, Depner H, Maglione M, Parutto P, Gratz S, Ryglewski S, Walter A, Holcman D, O'Connor-Giles K, Heine M, Sigrist S. 2022. An active zone state switch concentrates and immobilizes voltage-gated ca²⁺ channels to promote long-term plasticity. An Active Zone State Switch Concentrates and Immobilizes Voltage-Gated Ca²⁺ Channels to Promote Long-Term Plasticity. In *Review*:e1292687. DOI: <https://doi.org/10.21203/rs.3.rs-1292687/v1>
- Goel P, Dufour Bergeron D, Böhme MA, Nunnally L, Lehmann M, Buser C, Walter AM, Sigrist SJ, Dickman D. 2019. Homeostatic scaling of active zone scaffolds maintains global synaptic strength. *The Journal of Cell Biology* **218**:1706–1724. DOI: <https://doi.org/10.1083/jcb.201807165>, PMID: 30914419
- Graf ER, Valakh V, Wright CM, Wu C, Liu Z, Zhang YQ, DiAntonio A. 2012. RIM promotes calcium channel accumulation at active zones of the *Drosophila* neuromuscular junction. *The Journal of Neuroscience* **32**:16586–16596. DOI: <https://doi.org/10.1523/JNEUROSCI.0965-12.2012>, PMID: 23175814
- Gratz SJ, Ukken FP, Rubinstein CD, Thiede G, Donohue LK, Cummings AM, O'Connor-Giles KM. 2014. Highly specific and efficient CRISPR/Cas9-catalyzed homology-directed repair in *Drosophila*. *Genetics* **196**:961–971. DOI: <https://doi.org/10.1534/genetics.113.160713>, PMID: 24478335
- Gratz SJ, Goel P, Bruckner JJ, Hernandez RX, Khateeb K, Macleod GT, Dickman D, O'Connor-Giles KM. 2019. Endogenous tagging reveals differential regulation of Ca²⁺ Channels at single active zones during presynaptic homeostatic potentiation and depression. *The Journal of Neuroscience* **39**:2416–2429. DOI: <https://doi.org/10.1523/JNEUROSCI.3068-18.2019>, PMID: 30692227
- Harris KP, Littleton JT. 2015. Transmission, development, and plasticity of synapses. *Genetics* **201**:345–375. DOI: <https://doi.org/10.1534/genetics.115.176529>, PMID: 26447126
- Hastings MH, Man HY. 2018. Synaptic capture of laterally diffusing ampa receptors - an idea that stuck. *Trends in Neurosciences* **41**:330–332. DOI: <https://doi.org/10.1016/j.tins.2018.03.016>, PMID: 29801525
- Heinrich L, Ryglewski S. 2020. Different functions of two putative *Drosophila* α₂δ subunits in the same identified motoneurons. *Scientific Reports* **10**:13670. DOI: <https://doi.org/10.1038/s41598-020-69748-8>, PMID: 32792569
- Held RG, Liu C, Ma K, Ramsey AM, Tarr TB, De Nola G, Wang SSH, Wang J, van den Maagdenberg AMJM, Schneider T, Sun J, Blanpied TA, Kaeser PS. 2020. Synapse and active zone assembly in the absence of presynaptic ca²⁺ channels and ca²⁺ entry. *Neuron* **107**:667–683.. DOI: <https://doi.org/10.1016/j.neuron.2020.05.032>
- Hong H, Zhao K, Huang S, Huang S, Yao A, Jiang Y, Sigrist S, Zhao L, Zhang YQ. 2020. Structural remodeling of active zones is associated with synaptic homeostasis. *The Journal of Neuroscience* **40**:2817–2827. DOI: <https://doi.org/10.1523/JNEUROSCI.2002-19.2020>, PMID: 32122953
- Hoppa MB, Lana B, Margas W, Dolphin AC, Ryan TA. 2012. α₂δ expression sets presynaptic calcium channel abundance and release probability. *Nature* **486**:122–125. DOI: <https://doi.org/10.1038/nature11033>, PMID: 22678293
- Huntwork S, Littleton JT. 2007. A complexin fusion clamp regulates spontaneous neurotransmitter release and synaptic growth. *Nature Neuroscience* **10**:1235–1237. DOI: <https://doi.org/10.1038/nn1980>, PMID: 17873870
- Jorquera RA, Huntwork-Rodriguez S, Akbergenova Y, Cho RW, Littleton JT. 2012. Complexin controls spontaneous and evoked neurotransmitter release by regulating the timing and properties of synaptotagmin activity. *The Journal of Neuroscience* **32**:18234–18245. DOI: <https://doi.org/10.1523/JNEUROSCI.3212-12.2012>, PMID: 23238737
- Kawasaki F, Zou B, Xu X, Ordway RW. 2004. Active zone localization of presynaptic calcium channels encoded by the cacophony locus of *Drosophila*. *The Journal of Neuroscience* **24**:282–285. DOI: <https://doi.org/10.1523/JNEUROSCI.3553-03.2004>, PMID: 14715960
- Kittel RJ, Wichmann C, Rasse TM, Fouquet W, Schmidt M, Schmid A, Wagh DA, Pawlu C, Kellner RR, Willig KI, Hell SW, Buchner E, Heckmann M, Sigrist SJ. 2006. Bruchpilot promotes active zone assembly, Ca²⁺ channel clustering, and vesicle release. *Science* **312**:1051–1054. DOI: <https://doi.org/10.1126/science.1126308>, PMID: 16614170
- Kurshan PT, Oztan A, Schwarz TL. 2009. Presynaptic alpha2delta-3 is required for synaptic morphogenesis independent of its Ca²⁺-channel functions. *Nature Neuroscience* **12**:1415–1423. DOI: <https://doi.org/10.1038/nn.2417>, PMID: 19820706
- Liu KSY, Siebert M, Mertel S, Knoche E, Wegener S, Wichmann C, Matkovic T, Muhammad K, Depner H, Mettke C, Bückers J, Hell SW, Müller M, Davis GW, Schmitz D, Sigrist SJ. 2011. RIM-binding protein, a central part of the active zone, is essential for neurotransmitter release. *Science* **334**:1565–1569. DOI: <https://doi.org/10.1126/science.1212991>, PMID: 22174254
- Luo X, Rosenfeld JA, Yamamoto S, Harel T, Zuo Z, Hall M, Wierenga KJ, Pastore MT, Bartholomew D, Delgado MR, Rotenberg J, Lewis RA, Emrick L, Bacino CA, Eldomery MK, Coban Akdemir Z, Xia F, Yang Y, Lalani SR, Lotze T, et al. 2017. Clinically severe CACNA1A alleles affect synaptic function and

- neurodegeneration differentially. *PLOS Genetics* **13**:e1006905. DOI: <https://doi.org/10.1371/journal.pgen.1006905>, PMID: 28742085
- Ly CV**, Yao CK, Verstreken P, Ohyama T, Bellen HJ. 2008. Straightjacket is required for the synaptic stabilization of cacophony, a voltage-gated calcium channel alpha1 subunit. *The Journal of Cell Biology* **181**:157–170. DOI: <https://doi.org/10.1083/jcb.200712152>, PMID: 18391075
- Maas C**, Torres VI, Altrock WD, Leal-Ortiz S, Wagh D, Terry-Lorenzo RT, Fejtova A, Gundelfinger ED, Ziv NE, Garner CC. 2012. Formation of Golgi-derived active zone precursor vesicles. *The Journal of Neuroscience* **32**:11095–11108. DOI: <https://doi.org/10.1523/JNEUROSCI.0195-12.2012>, PMID: 22875941
- Maeder CI**, San-Miguel A, Wu EY, Lu H, Shen K. 2014. In vivo neuron-wide analysis of synaptic vesicle precursor trafficking. *Traffic* **15**:273–291. DOI: <https://doi.org/10.1111/tra.12142>, PMID: 24320232
- Marrus SB**, Portman SL, Allen MJ, Moffat KG, DiAntonio A. 2004. Differential localization of glutamate receptor subunits at the *Drosophila* neuromuscular junction. *The Journal of Neuroscience* **24**:1406–1415. DOI: <https://doi.org/10.1523/JNEUROSCI.1575-03.2004>, PMID: 14960613
- Melom JE**, Akbergenova Y, Gavornik JP, Littleton JT. 2013. Spontaneous and evoked release are independently regulated at individual active zones. *The Journal of Neuroscience* **33**:17253–17263. DOI: <https://doi.org/10.1523/JNEUROSCI.3334-13.2013>, PMID: 24174659
- Miller DL**, Ballard SL, Ganetzky B. 2012. Analysis of synaptic growth and function in *Drosophila* with an extended larval stage. *The Journal of Neuroscience* **32**:13776–13786. DOI: <https://doi.org/10.1523/JNEUROSCI.0508-12.2012>, PMID: 23035089
- Missler M**, Zhang W, Rohlmann A, Kattenstroth G, Hammer RE, Gottmann K, Südhof TC. 2003. Alpha-neurexins couple Ca²⁺ channels to synaptic vesicle exocytosis. *Nature* **423**:939–948. DOI: <https://doi.org/10.1038/nature01755>, PMID: 12827191
- Nakamura Y**, Harada H, Kamasawa N, Matsui K, Rothman JS, Shigemoto R, Silver RA, DiGregorio DA, Takahashi T. 2015. Nanoscale distribution of presynaptic Ca(2+) channels and its impact on vesicular release during development. *Neuron* **85**:145–158. DOI: <https://doi.org/10.1016/j.neuron.2014.11.019>, PMID: 25533484
- Newman ZL**, Hoagland A, Aghi K, Worden K, Levy SL, Son JH, Lee LP, Isacoff EY. 2017. Input-specific plasticity and homeostasis at the *Drosophila* larval neuromuscular junction. *Neuron* **93**:1388–1404. DOI: <https://doi.org/10.1016/j.neuron.2017.02.028>, PMID: 28285823
- Newman ZL**, Bakshinskaya D, Schultz R, Kenny SJ, Moon S, Aghi K, Stanley C, Marnani N, Li R, Bleier J, Xu K, Isacoff EY. 2022. Determinants of synapse diversity revealed by super-resolution quantal transmission and active zone imaging. *Nature Communications* **13**:229. DOI: <https://doi.org/10.1038/s41467-021-27815-2>, PMID: 35017509
- Ophoff RA**, Terwindt GM, Vergouwe MN, van Eijk R, Oefner PJ, Hoffman SM, Lamerdin JE, Mohrenweiser HW, Bulman DE, Ferrari M, Haan J, Lindhout D, van Ommen GJ, Hofker MH, Ferrari MD, Frants RR. 1996. Familial hemiplegic migraine and episodic ataxia type-2 are caused by mutations in the Ca²⁺ channel gene CACNL1A4. *Cell* **87**:543–552. DOI: [https://doi.org/10.1016/s0092-8674\(00\)81373-2](https://doi.org/10.1016/s0092-8674(00)81373-2), PMID: 8898206
- Peled ES**, Isacoff EY. 2011. Optical quantal analysis of synaptic transmission in wild-type and rab3-mutant *Drosophila* motor axons. *Nature Neuroscience* **14**:519–526. DOI: <https://doi.org/10.1038/nn.2767>
- Peled ES**, Newman ZL, Isacoff EY. 2014. Evoked and spontaneous transmission favored by distinct sets of synapses. *Current Biology: CB* **24**:484–493. DOI: <https://doi.org/10.1016/j.cub.2014.01.022>
- Perry S**, Goel P, Tran NL, Pinales C, Buser C, Miller DL, Ganetzky B, Dickman D. 2020. Developmental arrest of *Drosophila* larvae elicits presynaptic depression and enables prolonged studies of neurodegeneration. *Development (Cambridge, England)* **147**:e186312. DOI: <https://doi.org/10.1242/dev.186312>
- Petzoldt AG**, Lützkendorf J, Sigrist SJ. 2016. Mechanisms controlling assembly and plasticity of presynaptic active zone scaffolds. *Current Opinion in Neurobiology* **39**:69–76. DOI: <https://doi.org/10.1016/j.conb.2016.04.009>
- Pietrobon D**, Striessnig J. 2003. Neurobiology of migraine. *Nature Reviews. Neuroscience* **4**:386–398. DOI: <https://doi.org/10.1038/nrn1102>, PMID: 12728266
- Port F**, Chen HM, Lee T, Bullock SL. 2014. Optimized CRISPR/Cas tools for efficient germline and somatic genome engineering in *Drosophila*. *PNAS* **111**:E2967–E2976. DOI: <https://doi.org/10.1073/pnas.1405500111>, PMID: 25002478
- Rasse TM**, Fouquet W, Schmid A, Kittel RJ, Mertel S, Sigrist CB, Schmidt M, Guzman A, Merino C, Qin G, Quentin C, Madeo FF, Heckmann M, Sigrist SJ. 2005. Glutamate receptor dynamics organizing synapse formation in vivo. *Nature Neuroscience* **8**:898–905. DOI: <https://doi.org/10.1038/nn1484>, PMID: 16136672
- Ravenscroft TA**, Janssens J, Lee PT, Tepe B, Marcogliese PC, Makhzami S, Holmes TC, Aerts S, Bellen HJ. 2020. *Drosophila* voltage-gated sodium channels are only expressed in active neurons and are localized to distal axonal initial segment-like domains. *The Journal of Neuroscience* **40**:7999–8024. DOI: <https://doi.org/10.1523/JNEUROSCI.0142-20.2020>, PMID: 32928889
- Rewitz KF**, Yamanaka N, Gilbert LI, O'Connor MB. 2009. The insect neuropeptide PTTH activates receptor tyrosine kinase torso to initiate metamorphosis. *Science* **326**:1403–1405. DOI: <https://doi.org/10.1126/science.1176450>, PMID: 19965758
- Ryder E**, Ashburner M, Bautista-Llacer R, Drummond J, Webster J, Johnson G, Morley T, Chan YS, Blows F, Coulson D, Reuter G, Baisch H, Apelt C, Kauk A, Rudolph T, Kube M, Klimm M, Nickel C, Szidonya J, Maróy P, et al. 2007. The drosdel deletion collection: A *Drosophila* genomewide chromosomal deficiency resource. *Genetics* **177**:615–629. DOI: <https://doi.org/10.1534/genetics.107.076216>, PMID: 17720900

- Ryglewski S**, Lance K, Levine RB, Duch C. 2012. Ca(v)2 channels mediate low and high voltage-activated calcium currents in *Drosophila* motoneurons. *The Journal of Physiology* **590**:809–825. DOI: <https://doi.org/10.1113/jphysiol.2011.222836>, PMID: 22183725
- Saheki Y**, Bargmann CI. 2009. Presynaptic CaV2 calcium channel traffic requires CALF-1 and the alpha(2)delta subunit UNC-36. *Nature Neuroscience* **12**:1257–1265. DOI: <https://doi.org/10.1038/nn.2383>, PMID: 19718034
- Schindelin J**, Arganda-Carreras I, Frise E, Kaynig V, Longair M, Pietzsch T, Preibisch S, Rueden C, Saalfeld S, Schmid B, Tinevez JY, White DJ, Hartenstein V, Eliceiri K, Tomancak P, Cardona A. 2012. Fiji: an open-source platform for biological-image analysis. *Nature Methods* **9**:676–682. DOI: <https://doi.org/10.1038/nmeth.2019>, PMID: 22743772
- Schöpf CL**, Ablinger C, Geisler SM, Stanika RI, Campiglio M, Kaufmann WA, Nimmervoll B, Schlick B, Brockhaus J, Missler M, Shigemoto R, Obermair GJ. 2021. Presynaptic $\alpha_2\delta$ subunits are key organizers of glutamatergic synapses. *PNAS* **118**:e1920827118. DOI: <https://doi.org/10.1073/pnas.1920827118>, PMID: 33782113
- Sheng J**, He L, Zheng H, Xue L, Luo F, Shin W, Sun T, Kuner T, Yue DT, Wu LG. 2012. Calcium-channel number critically influences synaptic strength and plasticity at the active zone. *Nature Neuroscience* **15**:998–1006. DOI: <https://doi.org/10.1038/nn.3129>, PMID: 22683682
- Stahl A**, Noyes NC, Boto T, Botero V, Broyles CN, Jing M, Zeng J, King LB, Li Y, Davis RL, Tomchik SM. 2022. Associative learning drives longitudinally graded presynaptic plasticity of neurotransmitter release along axonal compartments. *eLife* **11**:e76712. DOI: <https://doi.org/10.7554/eLife.76712>, PMID: 35285796
- Vukoja A**, Rey U, Petzoldt AG, Ott C, Vollweiler D, Quentin C, Puchkov D, Reynolds E, Lehmann M, Hohensee S, Rosa S, Lipowsky R, Sigrist SJ, Haucke V. 2018. Presynaptic biogenesis requires axonal transport of lysosome-related vesicles. *Neuron* **99**:1216–1232. DOI: <https://doi.org/10.1016/j.neuron.2018.08.004>
- Wang LY**, Neher E, Taschenberger H. 2008. Synaptic vesicles in mature calyx of Held synapses sense higher nanodomain calcium concentrations during action potential-evoked glutamate release. *J Neuroscience* **28**:14450–14458. DOI: <https://doi.org/10.1523/JNEUROSCI.4245-08.2008>, PMID: 19118179
- Wang T**, Jones RT, Whippen JM, Davis GW. 2016. $\alpha_2\delta$ -3 Is required for rapid transsynaptic homeostatic signaling. *Cell Reports* **16**:2875–2888. DOI: <https://doi.org/10.1016/j.celrep.2016.08.030>
- Wu YE**, Huo L, Maeder CI, Feng W, Shen K. 2013. The balance between capture and dissociation of presynaptic proteins controls the spatial distribution of synapses. *Neuron* **78**:994–1011. DOI: <https://doi.org/10.1016/j.neuron.2013.04.035>
- Zhai RG**, Bellen HJ. 2004. The architecture of the active zone in the presynaptic nerve terminal. *Physiology* **19**:262–270. DOI: <https://doi.org/10.1152/physiol.00014.2004>, PMID: 15381754
- Zhang Y**, Füger P, Hannan SB, Kern JV, Lasky B, Rasse TM. 2010. In vivo imaging of intact *Drosophila* larvae at sub-cellular resolution. *Journal of Visualized Experiments*:2249. DOI: <https://doi.org/10.3791/2249>, PMID: 20864927
- Zhang YV**, Hannan SB, Stapper ZA, Kern JV, Jahn TR, Rasse TM. 2016. The *Drosophila* KIF1A Homolog unc-104 is important for site-specific synapse maturation. *Frontiers in Cellular Neuroscience* **10**:207. DOI: <https://doi.org/10.3389/fncel.2016.00207>, PMID: 27656128
- Zhuchenko O**, Bailey J, Bonnen P, Ashizawa T, Stockton DW, Amos C, Dobyns WB, Subramony SH, Zoghbi HY, Lee CC. 1997. Autosomal dominant cerebellar ataxia (SCA6) associated with small polyglutamine expansions in the alpha 1A-voltage-dependent calcium channel. *Nature Genetics* **15**:62–69. DOI: <https://doi.org/10.1038/ng0197-62>, PMID: 8988170



Figures and figure supplements

Regulation of presynaptic Ca^{2+} channel abundance at active zones through a balance of delivery and turnover

Karen L Cunningham *et al*

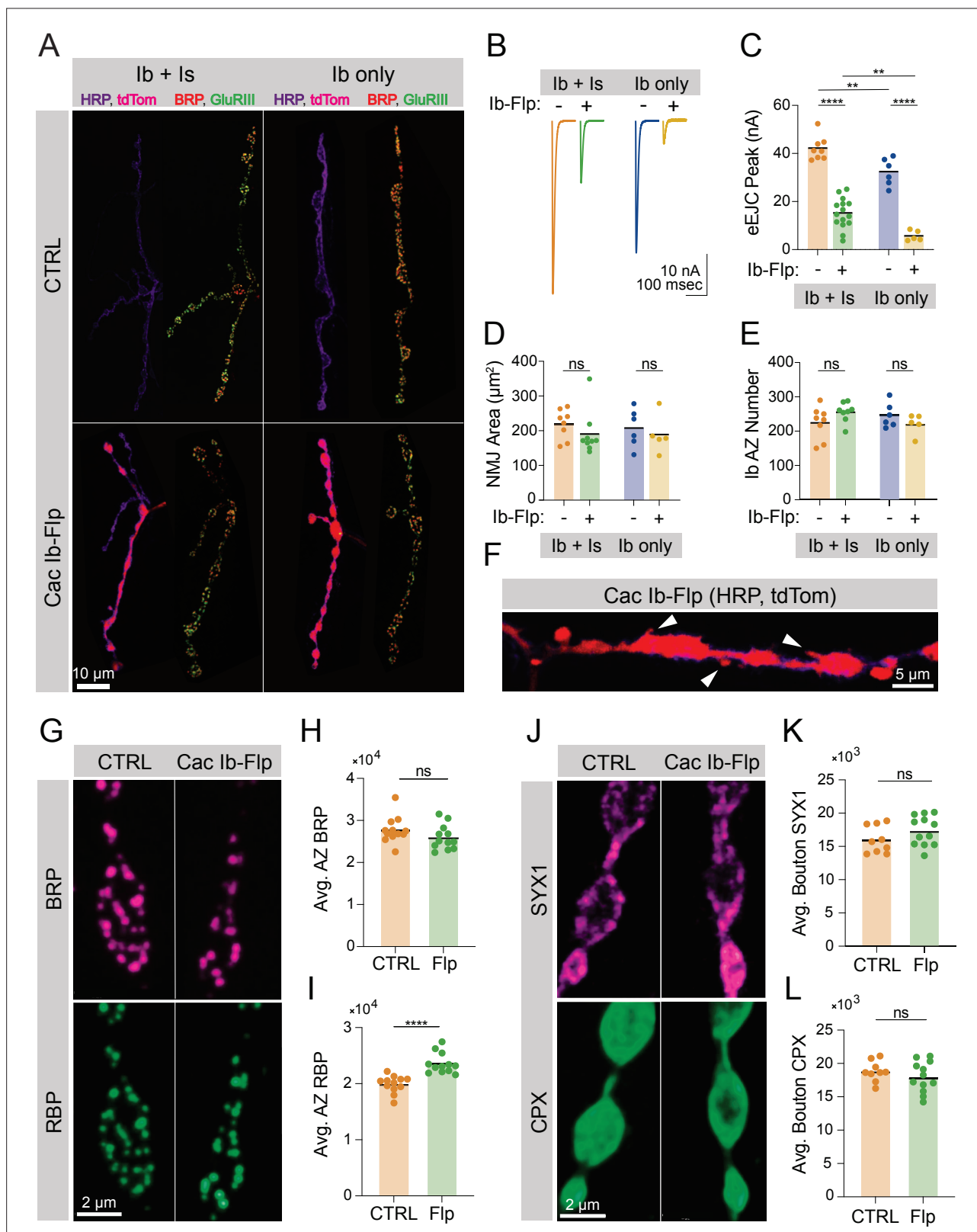


Figure 1. Ca^{2+} channels are not required for active zone (AZ) seeding or scaffold accumulation. **(A)** Representative images of control neuromuscular junctions (NMJs) with both Ib and Is motoneurons co-innervating muscle 1 (top left), or muscle 1 with only Ib innervation (top right), and Is and cac-flipped Ib neurons co-innervating muscle 1 (bottom left) or cac-flipped Ib neurons with no Is present (bottom right). The flip-reporter tdTomato (magenta) and HRP (neuronal membranes; purple) were imaged prior to fixation (left panels). After fixation, NMJs were immunostained for Bruchpilote

Figure 1 continued on next page

Figure 1 continued

(BRP) (red) and GluRIII (green) to label AZs and PSDs, respectively (right panels). **(B, C)** Average traces and evoked amplitudes (peak current, nA) from the indicated genotypes (co-innervated controls: orange, 42.11 ± 1.757 , n=8 NMJs from 6 animals; co-innervated $Cac^{lb-flip}$: green, 15.13 ± 1.607 , n=15 NMJs from 12 animals, $p < 0.0001$; lb-only controls: blue, 32.32 ± 2.329 , n=6 NMJs from 6 animals; lb-only $Cac^{lb-flip}$: gold, 5.749 ± 0.9544 , n=5 NMJs from 5 animals, $p < 0.0001$). **(D)** Neuronal (HRP-stained) area of lb synapses (co-innervated controls: orange, 219.1 ± 15.15 , n=8 NMJs from 6 animals; co-innervated $Cac^{lb-flip}$: green, 190.4 ± 21.12 , 9 NMJs from 8 animals; lb-only controls: blue, 207.8 ± 22.4 , n=6 NMJs from 6 animals; lb-only $Cac^{lb-flip}$: gold, 189 ± 24.59 , n=5 NMJs from 5 animals). **(E)** Number of AZs formed by lb synapses (co-innervated controls: orange, 224.3 ± 16.88 ; co-innervated $Cac^{lb-flip}$: green, 255.1 ± 10.13 ; lb-only controls: blue, 245.8 ± 14.73 ; lb-only $Cac^{lb-flip}$: gold, 220.4 ± 13.47). **(F)** Some NMJs lacking *Cac* display ectopic filopodia extending from boutons (white arrowheads). **(G)** Representative images of *cac*-flipped NMJs stained with anti-BRP (magenta) and anti-RIM-binding protein (RBP) (green). **(H)** Quantification of BRP abundance. Each point represents the average fluorescence intensity across the AZ population of a single NMJ (CTRL: orange, $27,736 \pm 900.2$, n=12 NMJs from 6 animals; $Cac^{lb-flip}$: green, $25,943 \pm 843.7$, n=12 NMJs from 6 animals). **(I)** Quantification of RBP abundance (CTRL: orange, $19,910 \pm 439.2$; $Cac^{lb-flip}$: green, $23,593 \pm 530.6$, $p < 0.0001$). **(J)** Representative images of *cac*-flipped animals stained for syntaxin 1 (SYX1) (magenta) and complexin (CPX) (green). **(K)** Quantification of SYX1 abundance. Each point represents the average fluorescence intensity across the bouton population of a single NMJ (CTRL: orange, $16,028 \pm 683.5$, n=9 NMJs from 5 animals; $Cac^{lb-flip}$: green, $17,365 \pm 643.4$, n=12 NMJs from 6 animals). **(L)** Quantification of CPX abundance (CTRL: orange, $18,810 \pm 509.4$; $Cac^{lb-flip}$: green, $17,961 \pm 663.5$).

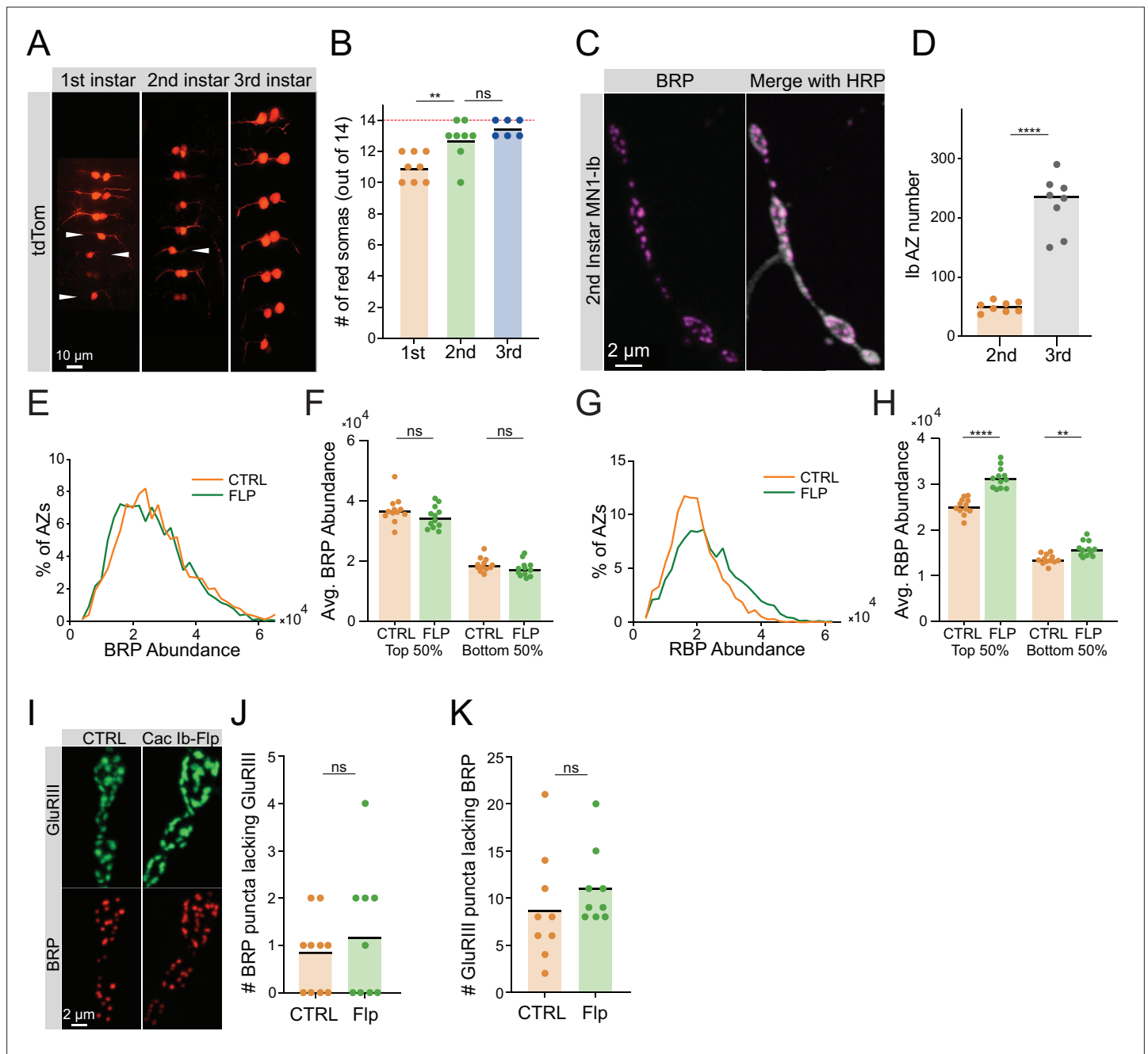


Figure 1—figure supplement 1. Characterization of *Cac*-flipping. **(A)** Representative ventral nerve cords (VNCs) in 1st, 2nd, and 3rd instar larvae expressing the tdTomato reporter in MN1-lb cell bodies of neurons that have undergone a *cac*-flip event in abdominal segments A1-A7. White arrowheads indicate hemisegments that have not flipped. **(B)** Quantification of the number of MN1-lb somas (out of 14 total neurons) expressing the tdTomato reporter in 1st, 2nd, and 3rd instar VNCs (1st: 11 ± 0.3273 , $n=8$ VNCs; 2nd: 12.75 ± 0.4532 , $n=8$ VNCs, $p<0.01$; 3rd: 13.5 ± 0.2236 , $n=6$ VNCs). **(C)** Representative images of MN1-lb NMJs in the 2nd instar stage stained with Bruchpilot (BRP) and HRP. **(D)** Quantification of lb active zone (AZ) number at the 2nd instar stage (orange) with 3rd instar MN1-lb AZ number (gray) from **Figure 1E** for comparison (2nd: 49.75 ± 3.155 , $n=8$ neuromuscular junctions (NMJs); 3rd: 224.3 ± 16.88 , $N=8$ NMJs, $p<0.0001$). **(E)** Distribution of BRP abundance (max pixel intensity per AZ) across the AZ population in control and *cac*-flipped NMJs, quantified from images in **Figure 1G**. **(F)** Average AZ BRP abundance (per NMJ) for the highest BRP-enriched 50% of AZs and the least BRP-enriched 50% of AZs in control and *cac*-flip NMJs, quantified from images in **Figure 1G** (control top 50%: $36,937 \pm 1264$; Flp top 50%: $34,615 \pm 1056$; control bottom 50%: $18,874 \pm 647.8$; Flp bottom 50%: $17,539 \pm 740.6$). **(G)** Distribution of RIM-binding protein (RBP) abundance (max pixel intensity per AZ) across the AZ population in control and *cac*-flipped NMJs, quantified from images in **Figure 1G**. **(H)** Average AZ RBP abundance (per NMJ) for the highest RBP-enriched 50% of AZs and the least RBP-enriched 50% of AZs in control and *cac*-flipped NMJs, quantified from images in **Figure 1G** (control top 50%: $25,130 \pm 500.2$; Flp top 50%: $31,376 \pm 654.6$, $p<0.01$; control bottom 50%: $13,630 \pm 301.6$; Flp bottom 50%: $15,853 \pm 464.9$, $p > 0.05$ (ns)). **(I)** Representative images of NMJs in control (CTRL) and *Cac* lb-Flp larvae stained for GluRIII and BRP. **(J)** Quantification of the number of BRP puncta lacking GluRIII in control (CTRL) and *Flp* NMJs. $p > 0.05$ (ns). **(K)** Quantification of the number of GluRIII puncta lacking BRP in control (CTRL) and *Flp* NMJs. $p > 0.05$ (ns).

Figure 1—figure supplement 1 continued on next page

Figure 1—figure supplement 1 continued

$p < 0,0001$). **(I)** Representative images of control and *cac*-flipped AZs stained for GluRIII and BRP, acquired from the dataset in **Figure 1A–F**. **(J)** Quantification of the number of BRP-positive AZs per NMJ lacking GluRIII signal in control and *cac*-flipped neurons (control: 0.8 ± 0.2494 , $n = 10$ NMJs; Flp: 1.222 ± 0.4648 , $n = 9$ NMJs). **(K)** Quantification of the number of GluRIII-positive PSDs per NMJ lacking BRP signal in control and *cac*-flipped neurons (control: 8.889 ± 1.925 ; Flp: 11 ± 1.354).

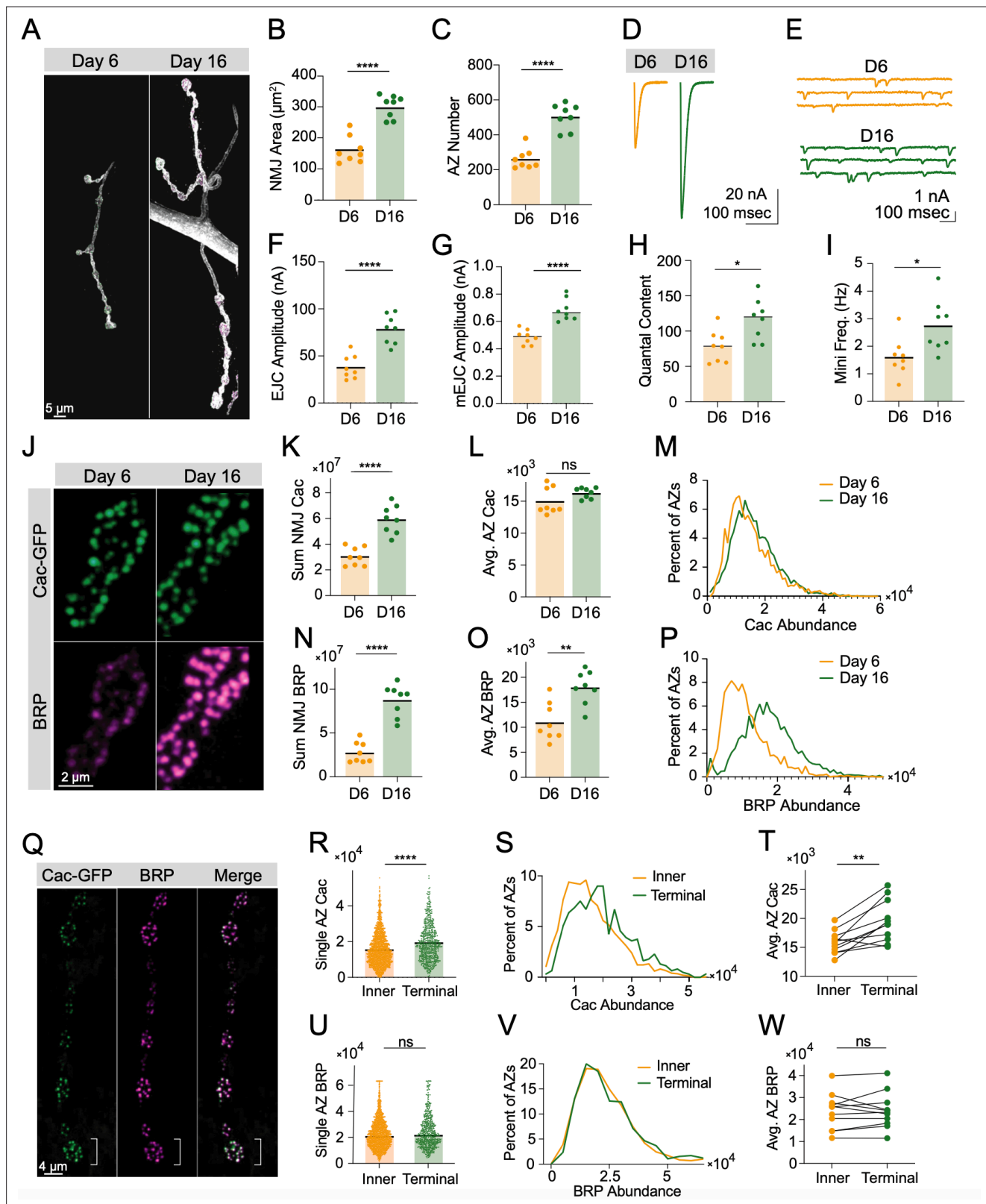


Figure 2. Bruchpilot (BRP) and Cac display distinct active zone (AZ) accumulation trajectories. **(A)** Representative muscle 4 neuromuscular junctions (NMJs) (stained with anti-HRP) in long-lived larvae (*phm-GAL4 >UAS-torso-RNAi*) at 6 and 16 days of larval life. **(B)** Synaptic (HRP stained) area at muscle 4 NMJs on day 6 and day 16 (D6: orange, 169.5 ± 16.03 , $n=8$ NMJs from 6 animals; D16: green, 316.9 ± 13.64 , $n=8$ NMJs from 6 animals, $p < 0.0001$). **(C)** BRP-positive AZ number at muscle 4 NMJs on day 6 and day 16 (D6: orange, 261.6 ± 20.02 , D16: green, 504.8 ± 25.86 , $p < 0.0001$). **(D, E)** Average

Figure 2 continued on next page

Figure 2 continued

EJC traces and representative mEJC traces at muscle 6 NMJs on day 6 and day 16. **(F)** Average evoked amplitudes (peak current, nA) (D6: orange, 38.27 ± 4.421 , $n=8$ NMJs from 6 animals; D16: green, 78.35 ± 5.476 , $n=8$ NMJs from 6 animals, $p < 0.0001$). **(G)** Average mEJC peak amplitude (nA) (D6: 0.4862 ± 0.01891 ; D16: 0.6843 ± 0.9284 , $p < 0.0001$). **(H)** Quantal content (D6: 78.41 ± 8.012 ; D16: 116.4 ± 10.35 , $p = 0.0116$). **(I)** Average mini frequency (D6: 1.617 ± 0.2448 , D16: 2.748 ± 0.3335 , $p = 0.0161$). **(J)** Representative synaptic boutons with endogenously tagged Cac-GFP (green) and BRP (magenta). **(K)** Sum Cac abundance per NMJ (D6: $30,486,042 \pm 2,547,718$, $n=8$ NMJs from 6 animals; D16: $59,296,888 \pm 3,909,993$, $n=8$ NMJs from 6 animals, $p < 0.0001$). **(L)** Average AZ Cac-GFP signal intensity at NMJs on day 6 and day 16 (D6: $15,058 \pm 746.1$; D16: $16,296 \pm 290.9$). **(M)** Histogram showing distribution of Cac-GFP intensities across the AZ population at day 6 and day 16 NMJs. **(N)** Sum BRP abundance per NMJ (D6: $27,664,071 \pm 4,206,865$; D16: $87,502,172 \pm 6,434,001$, $p < 0.0001$). **(O)** Average AZ BRP abundance per NMJ (D6: $11,132 \pm 1350$; D16: $17,985 \pm 1178$, $p < 0.01$). **(P)** Histogram showing distribution of BRP intensities across the AZ population at day 6 and day 16 NMJs. **(Q)** Representative images of muscle 4 lb NMJs showing Cac-GFP (green) and BRP (magenta). The white bracket marks the terminal bouton. **(R)** AZ Cac abundance at inner boutons versus terminal boutons, with each point representing the maximum fluorescent pixel intensity for one AZ (Inner: $15,879 \pm 213$, $n=1951$ AZs; Terminal: $19,617 \pm 415.1$, $n=612$ AZs, $p < 0.0001$). **(S)** Distribution of AZ Cac-GFP intensities across the AZ population in inner boutons versus terminal boutons. **(T)** Average AZ Cac intensity for inner boutons versus terminal boutons. Inner boutons and terminal boutons from a single NMJ are connected with a line. **(U)** BRP abundance at AZs of inner versus terminal boutons (Inner: $23,009 \pm 262.8$, $n=1917$ AZs; Terminal: $24,210 \pm 504.1$, $n=602$ AZs). **(V, W)** BRP intensity distributions and pairwise comparisons of inner versus terminal boutons.

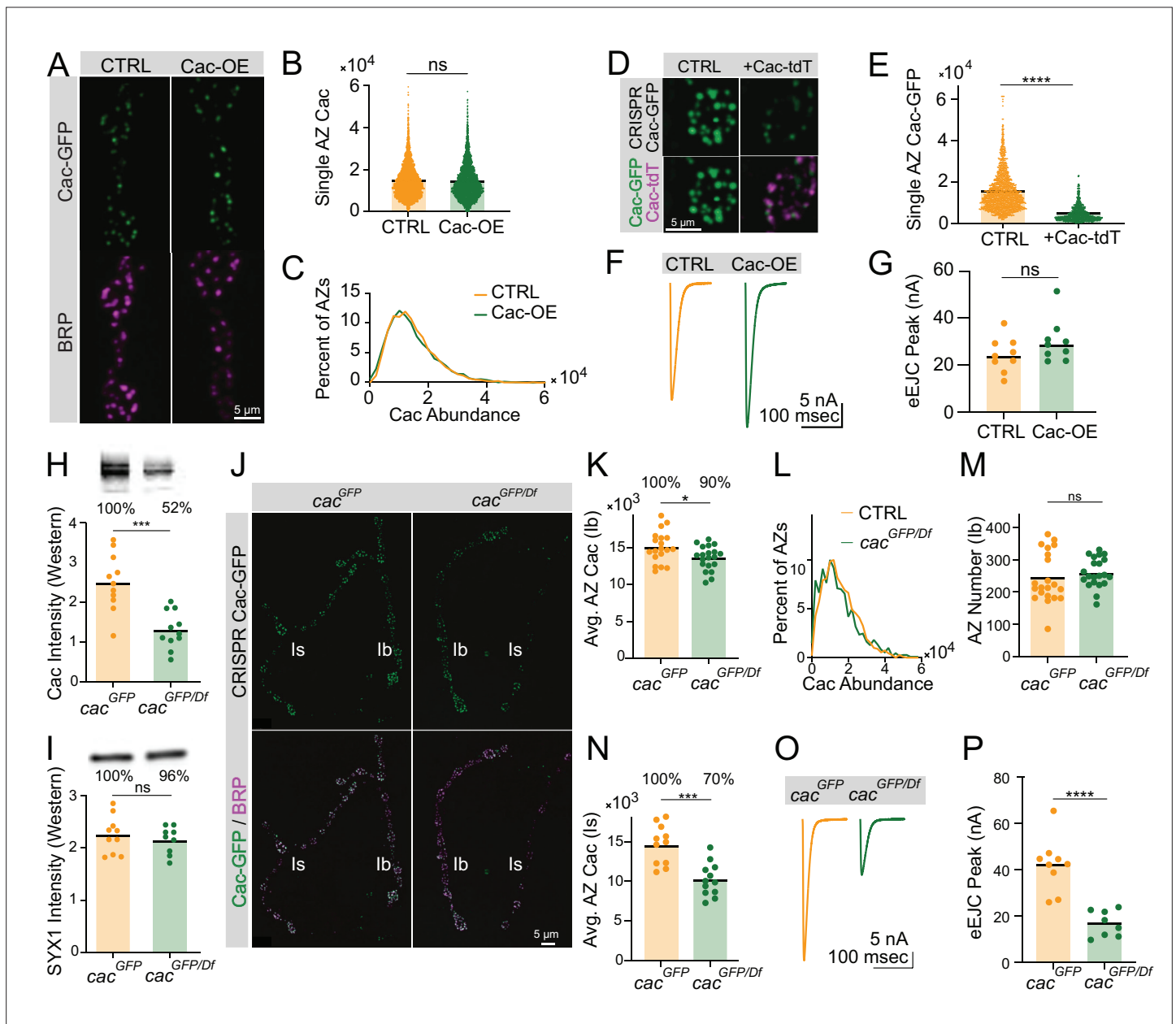


Figure 3. Active zone (AZ) Cac accumulation is regulated downstream of Cac biosynthesis. **(A)** Representative images of Cac-GFP (green) and Bruchpilot (BRP) (magenta) at muscle 4 for endogenously C-terminally tagged Cac-GFP controls (*cac^{GFP(C)}*, *C155/cac^{GFP(C)}*) and Cac overexpression animals (*cac^{GFP(C)}*, *C155/cac^{GFP(C)}*, *UAS-Cac-GFP*). **(B)** Quantification of AZ Cac intensity in control versus Cac overexpression neuromuscular junctions (NMJs). Each point represents the maximum Cac-GFP pixel intensity of a single AZ (control: 14617 ± 130.8 , $n=3663$ AZs from 10 NMJs from 6 animals; Cac OE: $14,383 \pm 148.2$, $n=3145$ AZs from 10 NMJs from 6 animals). **(C)** Distribution of AZ Cac-GFP abundance across the AZ population in control versus Cac overexpression NMJs. **(D)** Representative images of endogenously tagged Cac-GFP (green) and overexpressed Cac-tdTomato (magenta) at AZs in control (*cac^{GFP}*, *C155*) versus Cac-tdTomato overexpression (*cac^{GFP}*, *C155*; *UAS-Cac-tdT*). **(E)** Quantification of AZ Cac-GFP intensity with and without Cac-tdTomato overexpression (control: $15,339 \pm 232$, $n=1613$ AZs, Cac-tdT: 4477 ± 123.9 , $n=850$ AZs, $p < 0.0001$). **(F, G)** Average traces and evoked peak currents (nA) at muscle 6 in Cac overexpression and control animals (control: 24.45 ± 2.433 , $n=9$ NMJs from 5 animals; Cac OE: 30.11 ± 3.046 , $n=9$ NMJs from 5 animals). **(H, I)** Quantifications and representative images of Western blots of adult head extracts from *cac^{GFP/Df}* heterozygotes and *cac^{GFP}* controls ($n=11$ samples, extracts from 5 adult heads per sample). Each point in **H** represents Cac intensity in one lane (*cac^{GFP}*: $224,900 \pm 11,239$; *cac^{GFP/Df}*: $13,055 \pm 1403$, $p < 0.001$). Each point in **I** represents syntaxin 1 (SYX1) intensity in one lane (*cac^{GFP}*: $224,900 \pm 11,239$; *cac^{GFP/Df}*: $214,889 \pm 86,96$). Representative images for Cac and SYX are shown above each quantification. **(J)** Representative images of endogenous Cac-GFP (green) and BRP (magenta) at muscle 4 AZs in *cac^{GFP/Df}* heterozygotes and *cac^{GFP}* controls. lb and ls terminals are labeled in white. **(K)** Quantification of average Cac-GFP AZ abundance per MN4-lb NMJs (*cac^{GFP}*: $15,105 \pm 486.3$, $n=19$ NMJs from 7 animals; *cac^{GFP/Df}*: $13,617 \pm 365.9$, $n=21$ NMJs from 7 animals, $p < 0.05$). **(L)** Histogram of Cac-GFP intensity across the AZ population in *cac^{GFP/Df}* heterozygotes and *cac^{GFP}* controls at MN4-lb NMJs. **(M)** BRP-positive AZ number per MN4-lb NMJ (*cac^{GFP}*: $25,092 \pm 2146$; *cac^{GFP/Df}*: $13,055 \pm 1403$, $p < 0.001$). **(N)** Average AZ Cac (ls) for *cac^{GFP}* and *cac^{GFP/Df}*. 100% and 70% quantification shown. **(O)** Average traces and evoked peak currents (nA) at muscle 6 in *cac^{GFP}* and *cac^{GFP/Df}* animals. Scale bar: 5 nA, 100 msec. **(P)** eEJC Peak (nA) for *cac^{GFP}* and *cac^{GFP/Df}*. ****: p < 0.0001.

Figure 3 continued on next page

Figure 3 continued

243.4±17.05; $cac^{GFP/Df}$: 260.3±9.963). **(N)** Quantification of average AZ Cac-GFP intensity per Is innervation of muscle 4 NMJs (cac^{GFP} : 14,621±747.5, n=11 NMJs from 7 animals; $cac^{GFP/Df}$: 10,219±601 n=12 NMJs from 7 animals, p<0.001). **(O, P)** Average traces and evoked peak currents (nA) at muscle 6 in $cac^{GFP/Df}$ heterozygotes and cac^{GFP} controls (cac^{GFP} : 41.96±3.879, n=9 NMJs from 5 animals; $cac^{GFP/Df}$: 16.7±1.984, n=8 NMJs from 7 animals, p<0.0001).

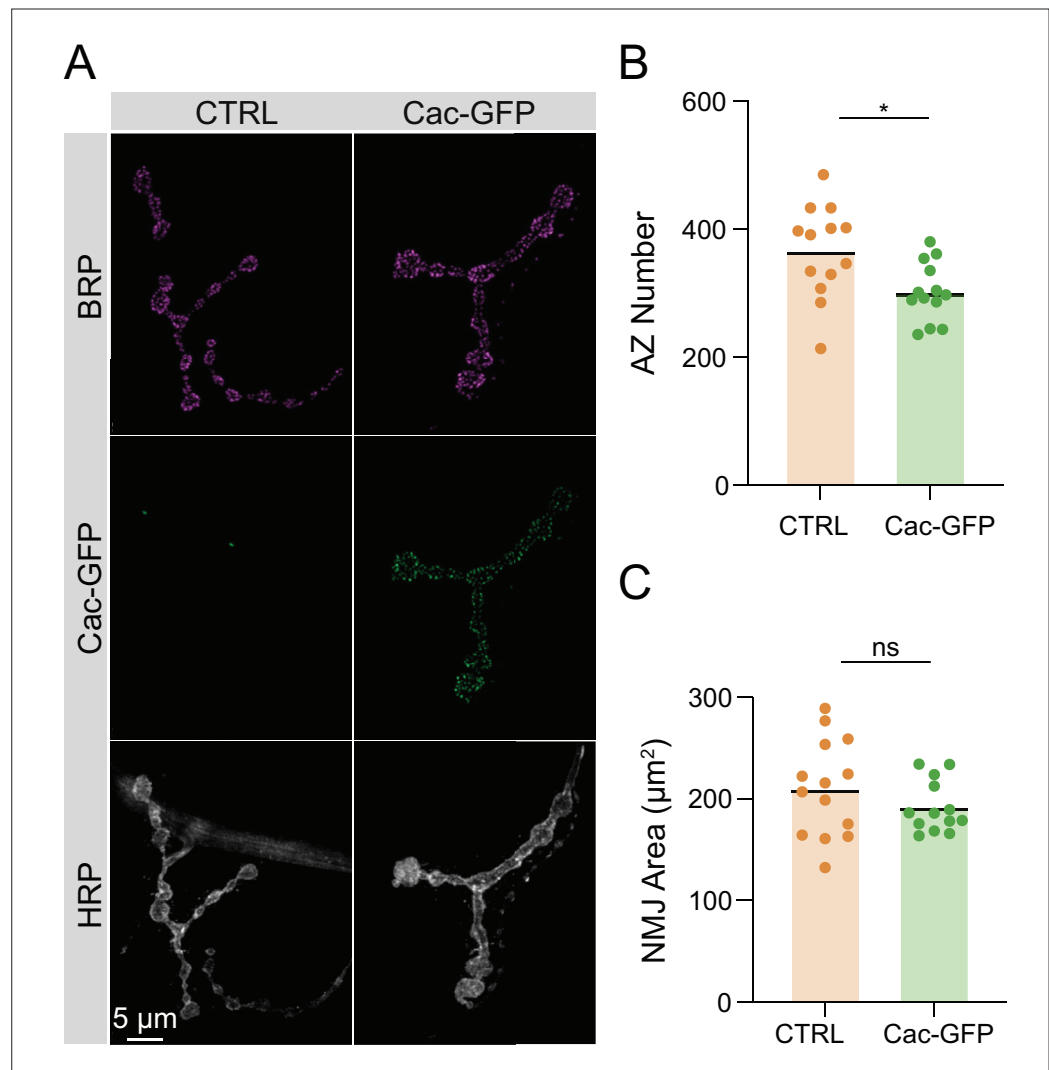


Figure 3—figure supplement 1. Synaptic morphology of Cac-GFP C-terminal CRISPR-tagged larvae. **(A)** Representative images of muscle 4 neuromuscular junctions (NMJs) stained for Bruchpilot (BRP) and HRP in control animals and animals expressing endogenously C-terminally tagged Cac-GFP ($cac^{GFP(C)}$). **(B)** Active zone (AZ) number in control and $cac^{GFP(C)}$ muscle 4 NMJs (control: 365.8 ± 20.17 , $n=13$ NMJs; $cac^{GFP(C)}$: 301.6 ± 12.72 , $n=13$ NMJs, $p=0.0127$). **(C)** NMJ area at control and $cac^{GFP(C)}$ muscle 4 NMJs (control: 207.1 ± 12.54 ; $cac^{GFP(C)}$: 189.2 ± 6.94).

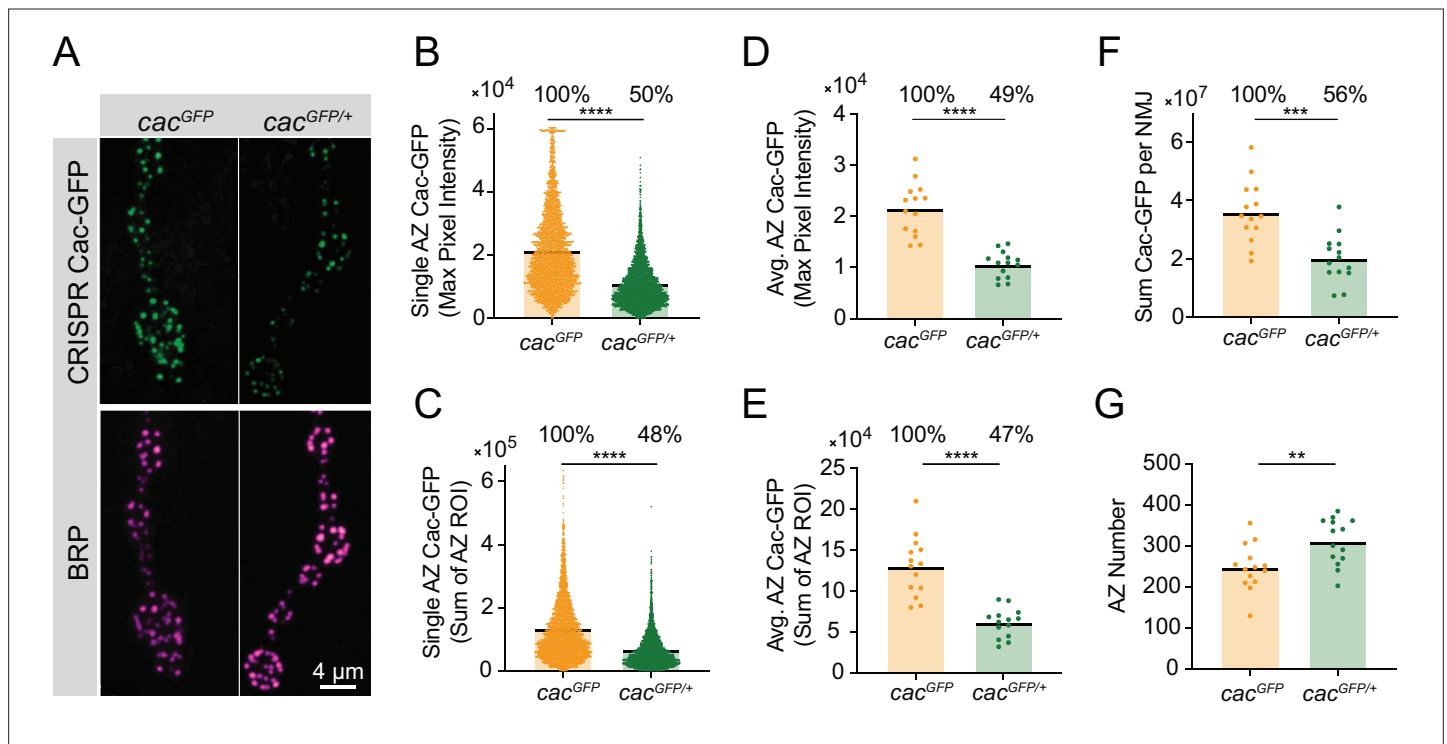


Figure 3—figure supplement 2. Quantitative imaging control. **(A)** Representative images of Cac-GFP at active zones (AZs) in female larvae homozygous for CRISPR-tagged Cac-GFP (*cac^{GFP}*, left) and heterozygous for CRISPR-tagged Cac-GFP (*cac^{GFP/+}*, right). Bruchpilot (BRP) immunostaining was used to identify AZs (magenta). **(B)** Quantification of single AZ Cac abundance using max pixel intensity per AZ (*cac^{GFP}*: 21,181±218.3, n=3452 AZs; *cac^{GFP/Df}*: 10,505±111.5, n=3,976 AZs, p<0.0001). **(C)** Sum AZ Cac abundance, with each point representing the sum of Cac-GFP fluorescence in an ROI encompassing a single AZ (*cac^{GFP}*: 127,105±172, n=3157 AZs; *cac^{GFP/Df}*: 60,865±859.1, n=3818 AZs, p<0.0001). **(D)** Average AZ Cac abundance per NMJ, with each point representing the average of max pixel intensities of the population of AZs at one NMJ (*cac^{GFP}*: 21,434±1366, n=14 NMJs; *cac^{GFP/Df}*: 10,552±686.2, n=14 NMJs, p<0.0001). **(E)** Average AZ Cac per NMJ, with each point representing the average of sum pixel intensities of the population of AZs at a single NMJ (*cac^{GFP}*: 129,806±9724; *cac^{GFP/Df}*: 60,724±4723, p<0.0001). **(F)** Total Cac at each NMJ (*cac^{GFP}*: 36,003,272±2,818,383; *cac^{GFP/Df}*: 20,063,946±2175784, p<0.001). **(G)** AZ number at each NMJ (*cac^{GFP}*: 246.6±14.82; *cac^{GFP/Df}*: 309.8±15.02, p<0.006).

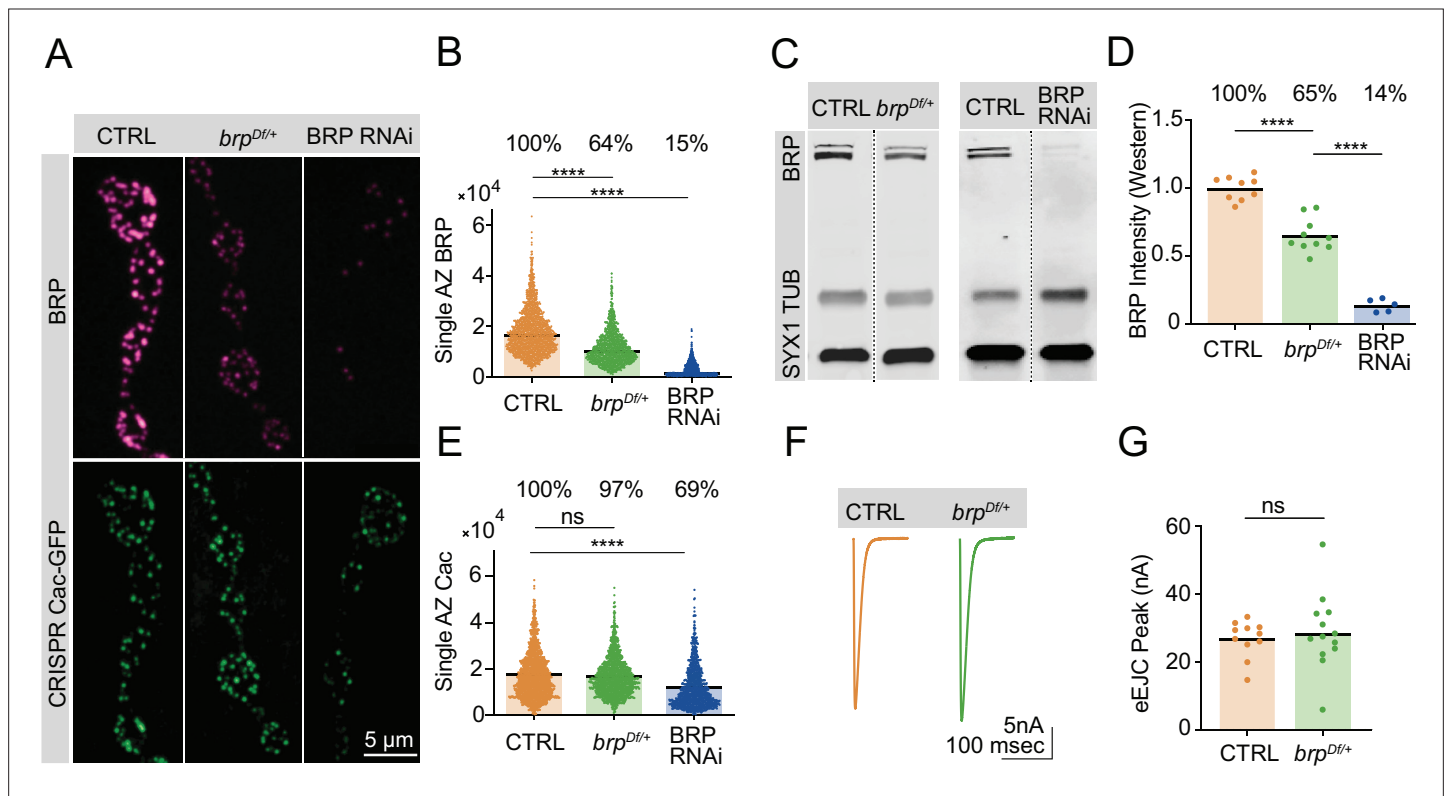


Figure 4. Bruchpilot (BRP) biosynthesis rate-limits active zone (AZ) BRP incorporation. **(A)** Representative images of BRP and endogenously tagged Cac-GFP at AZs in controls, *brp^{Df/+}* heterozygotes and pan-neuronally (*elav-GAL4*) expressed BRP RNAi. **(B)** Quantification of single AZ BRP intensity, with average AZ BRP intensity listed as a percent of control above each genotype (control: $18,161 \pm 210.7$, $n=1779$ AZs; *brp^{Df/+}*: $11,534 \pm 176.7$, $n=1350$ AZs, $p < 0.0001$; BRP RNAi: 2806 ± 79.91 , $n=1140$ AZs, $p < 0.0001$). **(C)** Representative image of Western blots of adult head extracts from control and *brp^{Df/+}* heterozygotes (left panel), and control and pan-neuronally expressed BRP RNAi animals (right panel) stained for syntaxin 1 (SYX1) (loading control), Tubulin, and BRP. **(D)** Quantification of BRP intensity in Western blots of the indicated genotypes. Each point represents BRP intensity in one lane, with BRP intensity normalized to the SYX1 loading control. Percent of protein abundance compared to control (100%) is shown above each genotype (control: 1.0 ± 0.02912 , $n=9$ lanes; *brp^{Df/+}*: 0.6518 ± 0.03862 , $n=10$ lanes, $p < 0.0001$; BRP RNAi: 0.1366 ± 0.02117 , $n=5$ lanes, $p < 0.0001$). **(E)** Quantification of endogenously tagged Cac-GFP intensity at single AZs in controls, *brp^{Df/+}* heterozygotes, and pan-neuronally expressed BRP RNAi (control: $17,268 \pm 232.4$, $n=1757$ AZs; *brp^{Df/+}*: $16,788 \pm 217$, $n=1403$ AZs; BRP RNAi: $11,959 \pm 259$, $n=1140$ AZs, $p < 0.0001$). **(F, G)** Average traces and quantified evoked peak currents (nA) in control and *brp^{Df/+}* heterozygotes at muscle 6 (control: 26.78 ± 1.632 , $n=11$ neuromuscular junctions (NMJs); *brp^{Df/+}*: 28.71 ± 3.105 , $n=13$ NMJs).

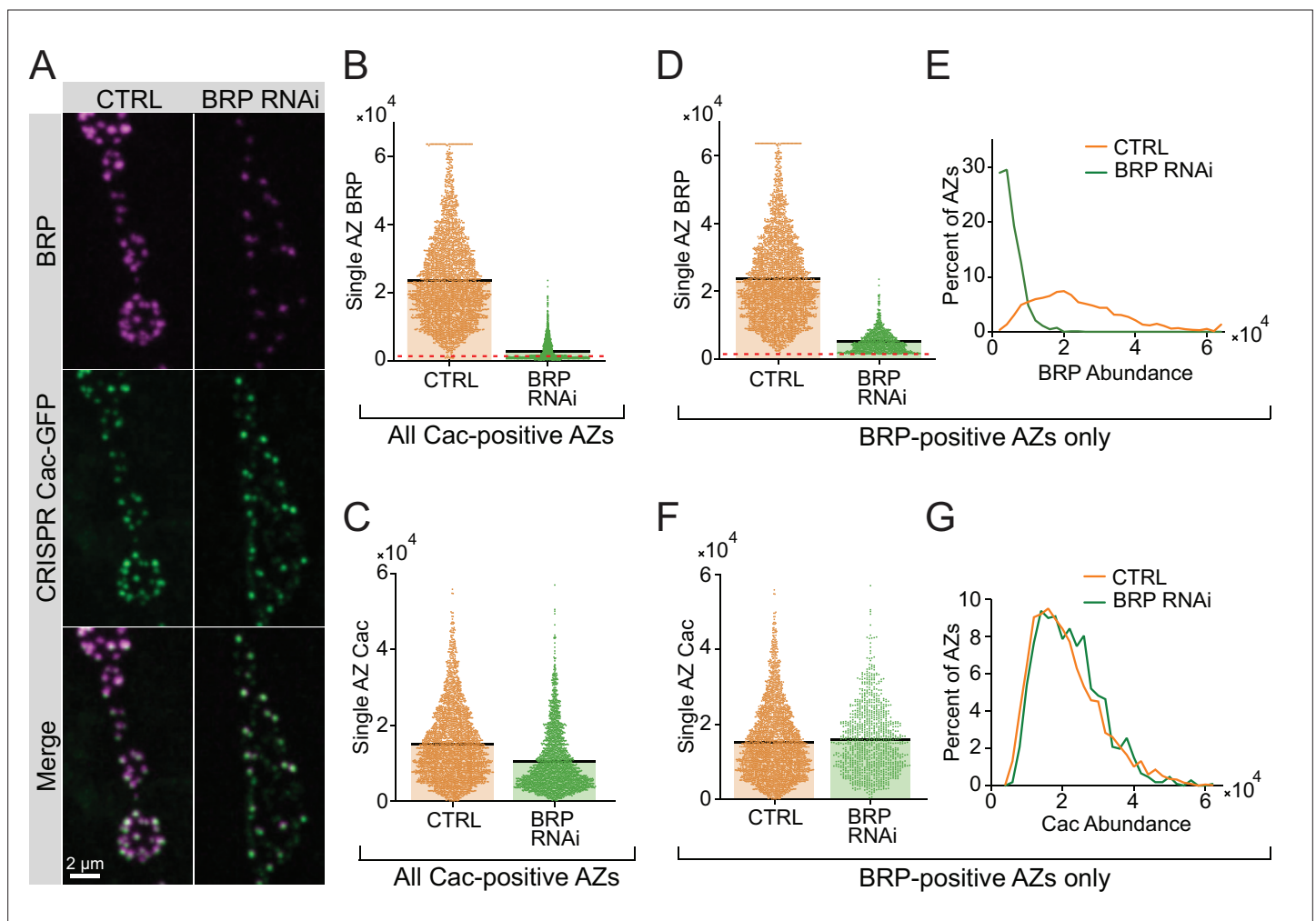


Figure 4—figure supplement 1. Single active zone (AZ) analysis of Cac and Bruchpilot (BRP) following BRP RNAi knockdown. **(A)** Representative images of endogenously tagged Cac-GFP (green) and BRP (magenta) in control (*C155, cac^{GFP}*) and BRP RNAi (*C155, cac^{GFP}; UAS-BRP-RNAi*) neuromuscular junctions (NMJs). **(B)** Quantification of single AZ BRP abundance (max pixel intensity per AZ) at control and BRP RNAi NMJs. AZs are defined by Cac-positive puncta. AZs below the red dotted line have zero measurable BRP (control: 23,623±230.1, n=3037 AZs; BRP RNAi: 2742±61.27, n=2363 AZs). **(C)** Quantification of single AZ Cac abundance (max pixel intensity per AZ) at all Cac-positive sites at control and BRP RNAi NMJs (control: 15,059±172.6; BRP RNAi: 10,592±165.9). **(D, E)** Quantification and histogram of single AZ BRP abundance (max pixel intensity) for all BRP-positive AZs (control: 23,691±229.7, n=3028 AZs; BRP RNAi: 5093±96.25, n=1055 AZs). **(F, G)** Quantification and histogram of single AZ Cac abundance (max pixel intensity) for all BRP-positive AZs (control: 15,090±172.8; BRP RNAi: 15,933±269.8).

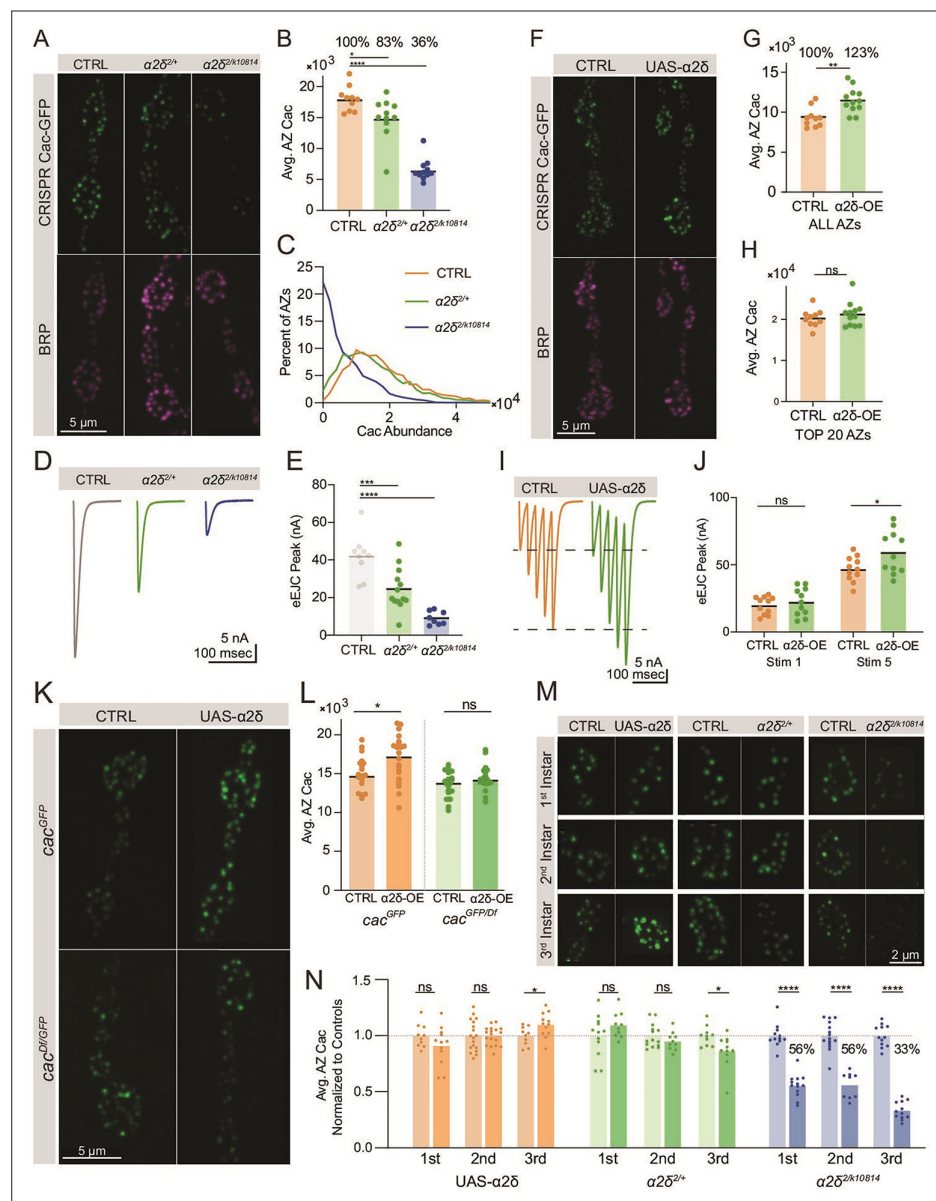


Figure 5. Cac accumulation at active zones (AZs) is dosage sensitive to the $\alpha 2\delta$ subunit. **(A)** Representative images of endogenously tagged Cac-GFP (green) and Bruchpilot (BRP) (magenta) in controls (cac^{GFP}), $\alpha 2\delta$ null heterozygotes ($cac^{GFP}; \alpha 2\delta^{2/+}$) and $\alpha 2\delta^{2/k10814}$ transheterozygotes ($cac^{GFP}; \alpha 2\delta^{2/k10814}$). **(B)** Quantification of average AZ Cac-GFP fluorescence of neuromuscular junctions (NMJs) in each genotype. Cac abundance as a percent of control levels is shown above each genotype (control: $18,007 \pm 641.1$, $n=10$ NMJs from 5 animals; $\alpha 2\delta^{2/+}$: $14,926 \pm 1014$, $n=11$ NMJs from 6 animals, $p=0.0174$; $\alpha 2\delta^{2/k10814}$: 6542 ± 541.3 , $n=11$ NMJs from 6 animals, $p<0.0001$). **(C)** Frequency distribution of single AZ Cac-GFP intensity across the AZ population in each genotype. **(D, E)** Average traces and quantified evoked peak current (nA) at muscle 6 for each genotype. Recordings were collected in combination with $cac^{GFP/Df}$ heterozygotes (**Figure 3P**) and the control is replicated here in gray for ease of comparison (control: 41.96 ± 3.879 , $n=9$ NMJs; $\alpha 2\delta^{2/+}$: 24.53 ± 3.133 , $n=13$ NMJs, $p<0.001$; $\alpha 2\delta^{2/k10814}$: 9.161 ± 1.268 , $n=8$ NMJs, $p<0.0001$). **(F)** Representative images of endogenously tagged Cac-GFP (green) and BRP (magenta) in control ($cac^{GFP}; C155$) and $\alpha 2\delta$ overexpression animals ($cac^{GFP}; C155; UAS-\alpha 2\delta$). **(G)** Average AZ Cac abundance per NMJ (control: 9332 ± 388.6 , $n=10$ NMJs from 5 animals; $\alpha 2\delta$ OE: 11497 ± 449.8 , $n=12$ NMJs from 6 animals, $p=0.0019$). **(H)** Average of top 20 brightest AZs per NMJ (control: $22,996 \pm 752.5$; $\alpha 2\delta$ OE: $24,823 \pm 1011$). **(I, J)** Average traces and quantified 1st and 5th stimulus evoked peak current at muscle 6 in 0.25 mM external Ca^{2+} for controls and $\alpha 2\delta$ overexpression animals (control 1st: 19.87 ± 1.98 , $n=11$ NMJs; $\alpha 2\delta$ OE 1st: 22.45 ± 3.127 , $n=11$ NMJs; control 5th: 46.82 ± 2.794 ; $\alpha 2\delta$ OE 5th: 59.21 ± 4.839 , $p=0.0249$). **(K, L)** Representative images and quantification of endogenously tagged Cac-GFP with (right) and without (left) $\alpha 2\delta$ overexpression in either control **Figure 5 continued on next page**

Figure 5 continued

(top) or $cac^{GFP/Df}$ heterozygous (bottom) NMJs ($cac^{GFP}, C155$: 15,105±486.3, n=19 NMJs; $cac^{GFP}, C155; UAS-\alpha 2\delta/+$: 17,142±814.4, n=15 NMJs, $p < 0.0225$; $cac^{Df}/cac^{GFP}, C155$: 13,617±365.9, n=20 NMJs; $cac^{Df}/cac^{GFP}, C155; UAS-\alpha 2\delta/+$: 14,895±587, n=12 NMJs). **(M, N)** Representative images and quantification of average AZ Cac intensity per NMJ of endogenously tagged Cac-GFP in 1st, 2nd, and 3rd instar muscle 4 lb NMJs in $\alpha 2\delta$ overexpression, $\alpha 2\delta^{2/+}$, and $\alpha 2\delta^{2/k10814}$ animals. Each pairwise comparison was normalized so that the control average is 1.0 ($\alpha 2\delta$ -OE 1st: 0.9125±0.0496, n=12 NMJs; $\alpha 2\delta$ -OE 2nd: 1±0.019, n=18 NMJs; $\alpha 2\delta$ -OE 3rd: 1.098±0.03132, n=12 NMJs, $p = 0.0296$; $\alpha 2\delta^{2/+}$ 1st: 1.096±0.0361, n=10 NMJs; $\alpha 2\delta^{2/+}$ 2nd: 0.9525±0.02574, n=10 NMJs; $\alpha 2\delta^{2/+}$ 3rd, $p = 0.0213$; 0.8661±0.04408, n=11 NMJs; $\alpha 2\delta^{2/k10814}$ 1st: 0.5569±0.02853, n=15 NMJs, $p < 0.0001$; $\alpha 2\delta^{2/k10814}$ 2nd: 0.5619±0.03902, n=9 NMJs, $p < 0.0001$; $\alpha 2\delta^{2/k10814}$ 3rd: 0.3344±0.02298, n=12 NMJs, $p < 0.0001$).

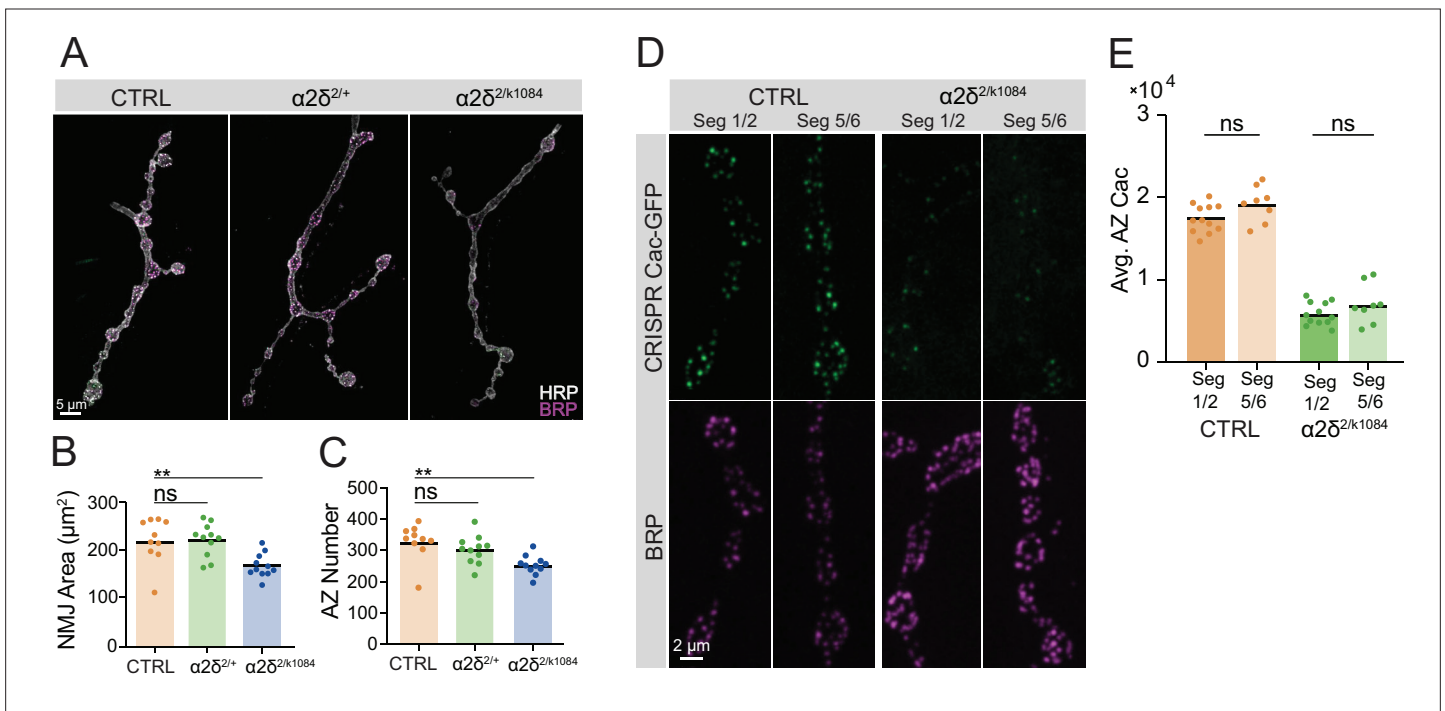


Figure 5—figure supplement 1. $\alpha 2\delta$'s role in regulating neuromuscular junction (NMJ) morphology is not dosage-sensitive and its Cac localization phenotype is independent of axon length. **(A)** Representative images of MN4-Ib synapses stained for HRP (white) and Bruchpilot (BRP) (magenta) in control, $\alpha 2\delta^{2/+}$ and $\alpha 2\delta^{2/k1084}$ NMJs. **(B)** NMJ area quantified for each genotype (control: 218 ± 14.65 , $n=10$ NMJs from 5 animals; $\alpha 2\delta^{2/+}$: 218.6 ± 10.23 , $n=11$ NMJs from 6 animals, $\alpha 2\delta^{2/k1084}$: 166 ± 7.378 , $n=11$ NMJs from 6 animals, $p < 0.01$). **(C)** Active zone (AZ) number quantified for each genotype (control: 328 ± 18.27 ; $\alpha 2\delta^{2/+}$: 302.2 ± 13.68 ; $\alpha 2\delta^{2/k1084}$: 253 ± 9.159 , $p < 0.01$). **(D)** Representative images of muscle 4 NMJs expressing endogenously tagged Cac-GFP and stained for BRP in control and $\alpha 2\delta^{2/k1084}$ animals in segment 1 or 2 (left panels) and segment 5 or 6 (right panels). **(E)** Quantification of average AZ Cac abundance per NMJ (control 1/2: $17,447 \pm 492.9$, $n=12$ NMJs; control 5/6: $19,189 \pm 767.7$, $n=8$ NMJs; $\alpha 2\delta^{2/k1084}$ 1/2: 5834 ± 401 , $n=12$ NMJs; $\alpha 2\delta^{2/k1084}$ 5/6: 6996 ± 844.1 , $n=8$ NMJs).

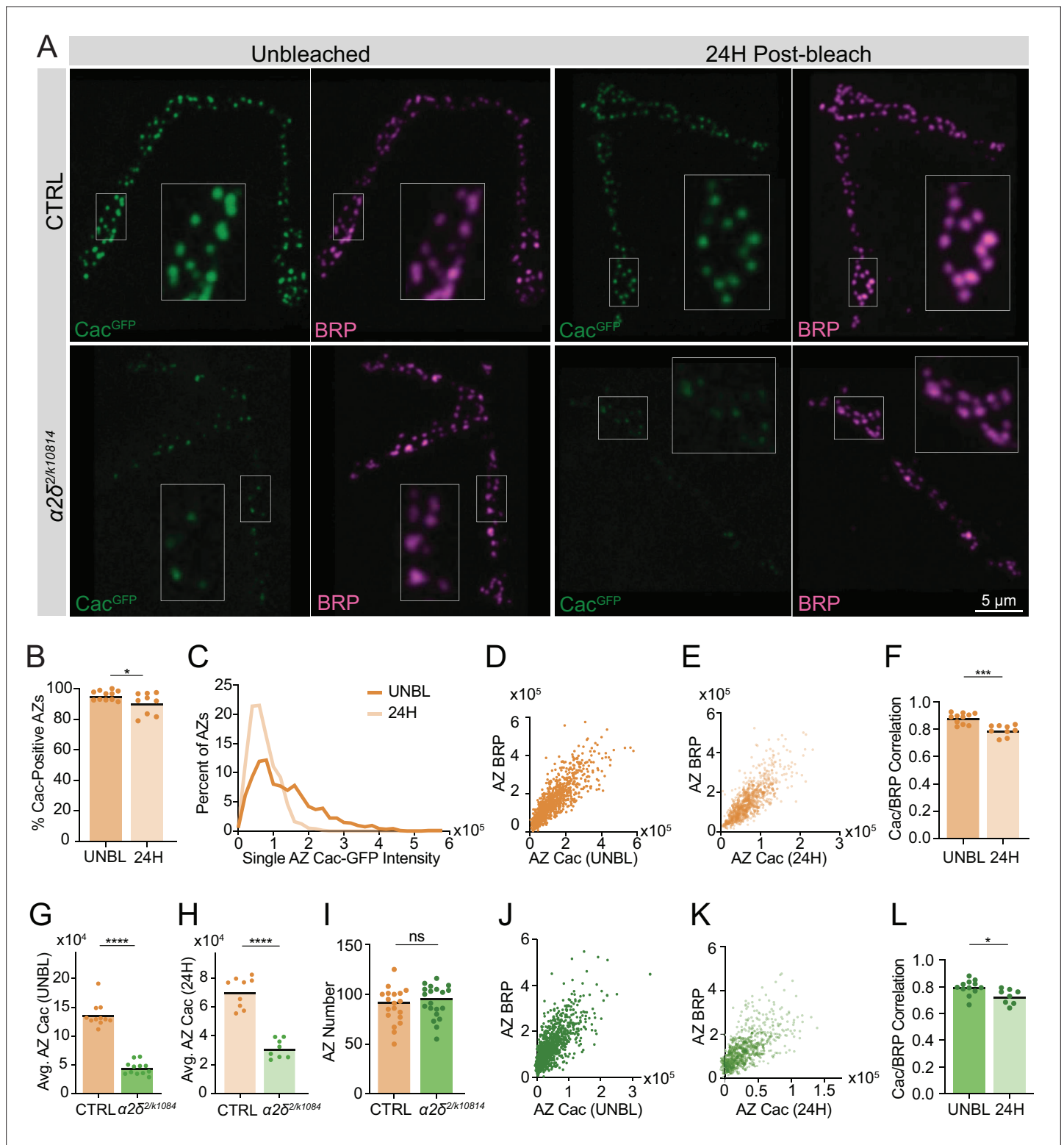


Figure 6. Cac delivery to active zones (AZs) correlates with AZ size and is regulated by $\alpha 2\delta$. **(A)** Representative images of FRAP experiments in CTRL (cac^{GFP}) and $\alpha 2\delta$ mutant ($cac^{GFP}; \alpha 2\delta^{2/k10814}$) neuromuscular junctions (NMJs). Fixed and Bruchpilot (BRP)-immunostained (magenta) NMJs are shown 24 hr post-bleaching, with unbleached NMJs as a control. Boutons inside white boxes are enlarged. **(B)** Percent of BRP-positive AZs with Cac-GFP max pixel intensity greater than 150% of average background fluorescence (pre: 95.56 ± 0.9347 ; 0H: 90.37 ± 2.347 , $p=0.0422$). **(C)** Distribution of single AZ Cac-GFP intensity (sum Cac-GFP fluorescence within an ROI encompassing each BRP-positive AZ) in unbleached NMJs (UNBL) and 24 hr after bleaching (pre: $13,6052 \pm 3018$, $n=946$ AZs; 24H: $72,261 \pm 1389$, $n=804$ AZs). **(D, E)** Correlations of Cac-GFP and BRP at individual AZs in unbleached controls **(D)** and

Figure 6 continued on next page

Figure 6 continued

NMJs 24 hr post-bleach (**E**). (**F**) Pearson r value for the correlation of Cac-GFP and BRP intensity across the AZ population at each NMJ in unbleached control NMJs (UNBL) and 24 hr post-bleach (pre: 0.8801 ± 0.01191 ; 24H: 0.7913 ± 0.01348 , $p < 0.001$). (**G**) Average AZ Cac-GFP intensity in unbleached segments in cac^{GFP} and $\alpha 2\delta^{2/k10814}$ NMJs (cac^{GFP} : $136,462 \pm 6346$, $n = 11$ NMJs; $\alpha 2\delta^{2/k10814}$: $44,340 \pm 3252$, $n = 12$ NMJs, $p < 0.0001$). (**H**) Average AZ Cac-GFP intensity 24 hr post-bleach (cac^{GFP} : $70,528 \pm 3508$, $n = 9$ NMJs; $\alpha 2\delta^{2/k10814}$: $31,086 \pm 2326$, $n = 8$ NMJs, $p < 0.0001$). (**I**) AZ number at NMJs (cac^{GFP} : 88.26 ± 4.13 , $n = 19$ NMJs; $\alpha 2\delta^{2/k10814}$: 92.45 ± 3.689 , $n = 20$ NMJs). (**J, K**) Correlation of Cac-GFP and BRP at individual AZs in unbleached $\alpha 2\delta^{2/k10814}$ mutants (**J**) and $\alpha 2\delta^{2/k10814}$ NMJs 24 hr post-bleach (**K**). (**L**) Pearson r value for the correlation of Cac-GFP and BRP intensity across the AZ population in unbleached NMJs (UNBL) and NMJs 24 hr post-bleach in $\alpha 2\delta^{2/k10814}$ mutants (UNBL: 0.7952 ± 0.01635 ; 24H: 0.7285 ± 0.01955 , $p = 0.018$).

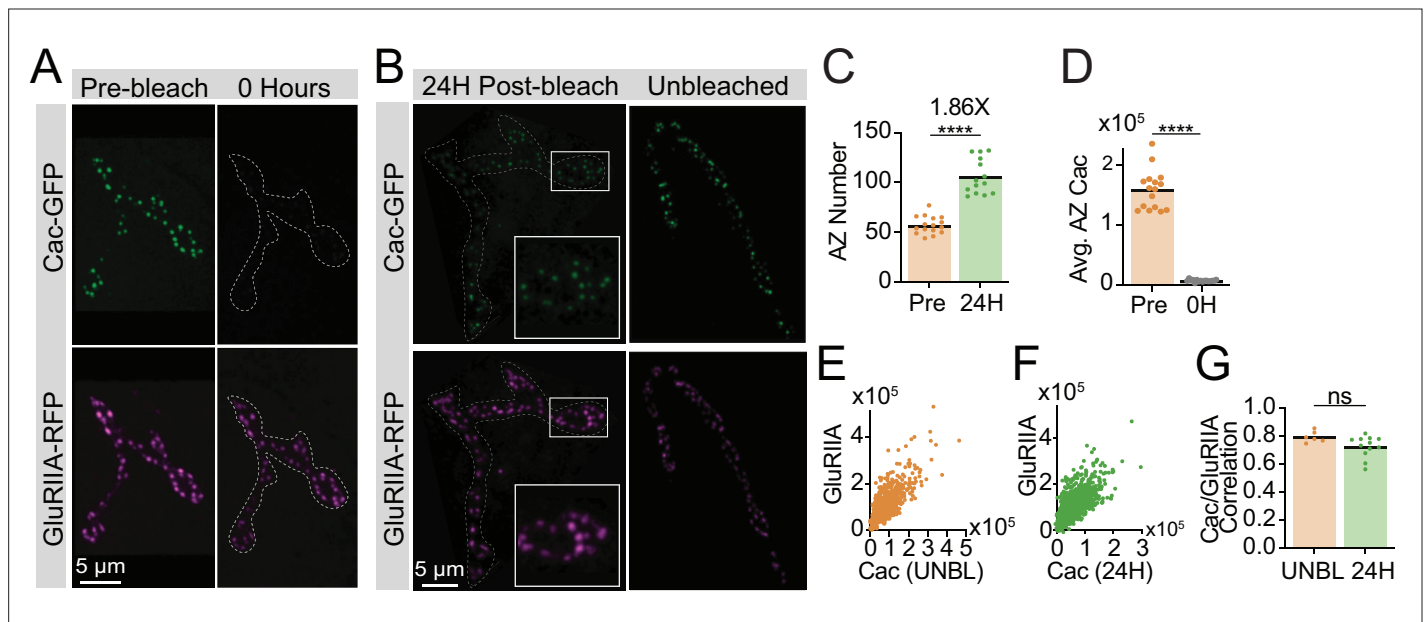


Figure 6—figure supplement 1. Photobleaching validation and GluRIIA correlations. **(A)** Representative images of muscle 26 in intravitaly imaged late 2nd instar larvae expressing endogenously tagged Cac-GFP (green) and GluRIIA-RFP (magenta) before (left column; pre-bleach) and immediately after (right column; 0 hr) Cac-GFP photobleaching. In the 0 hr timepoint, the neuromuscular junction (NMJ) is outlined with a white dotted line. **(B)** Representative images of the NMJ shown in panel A (left column) after fixation – NMJ area outlined in white. Right column is an NMJ from an unbleached segment of the same animal, used as a control. **(C)** Active zone (AZ) number (number of GluRIIA-RFP puncta) in pre-bleach and 24 hr post-bleach NMJs, with fold-increase in AZ number shown above (pre: 57.31 ± 2.198 , $n=16$ NMJs; 24H: 106 ± 4.716 , $n=14$ NMJs, $p < 0.0001$). **(D)** Average AZ Cac fluorescence (intravital) for each NMJ pre-bleach and immediately after bleaching (0H), measured as sum pixel intensity of an ROI encompassing each GluRIIA-positive receptor field (pre: $158,514 \pm 8197$; 0H: 7609 ± 446.8 , $p < 0.0001$). **(E, F)** Correlations of Cac-GFP and GluRIIA-RFP at individual AZs in unbleached controls **(E)** and 24 hr post-bleach **(F)**. **(G)** Pearson r value for the correlation of Cac-GFP and GluRIIA intensity across the AZ population at each NMJ in control segments (unbleached; UNBL) and 24 hr post-bleach (UNBL: 0.792 ± 0.01618 , $n=6$ NMJs; 24H: 0.7222 ± 0.02212 , $n=12$ NMJs).

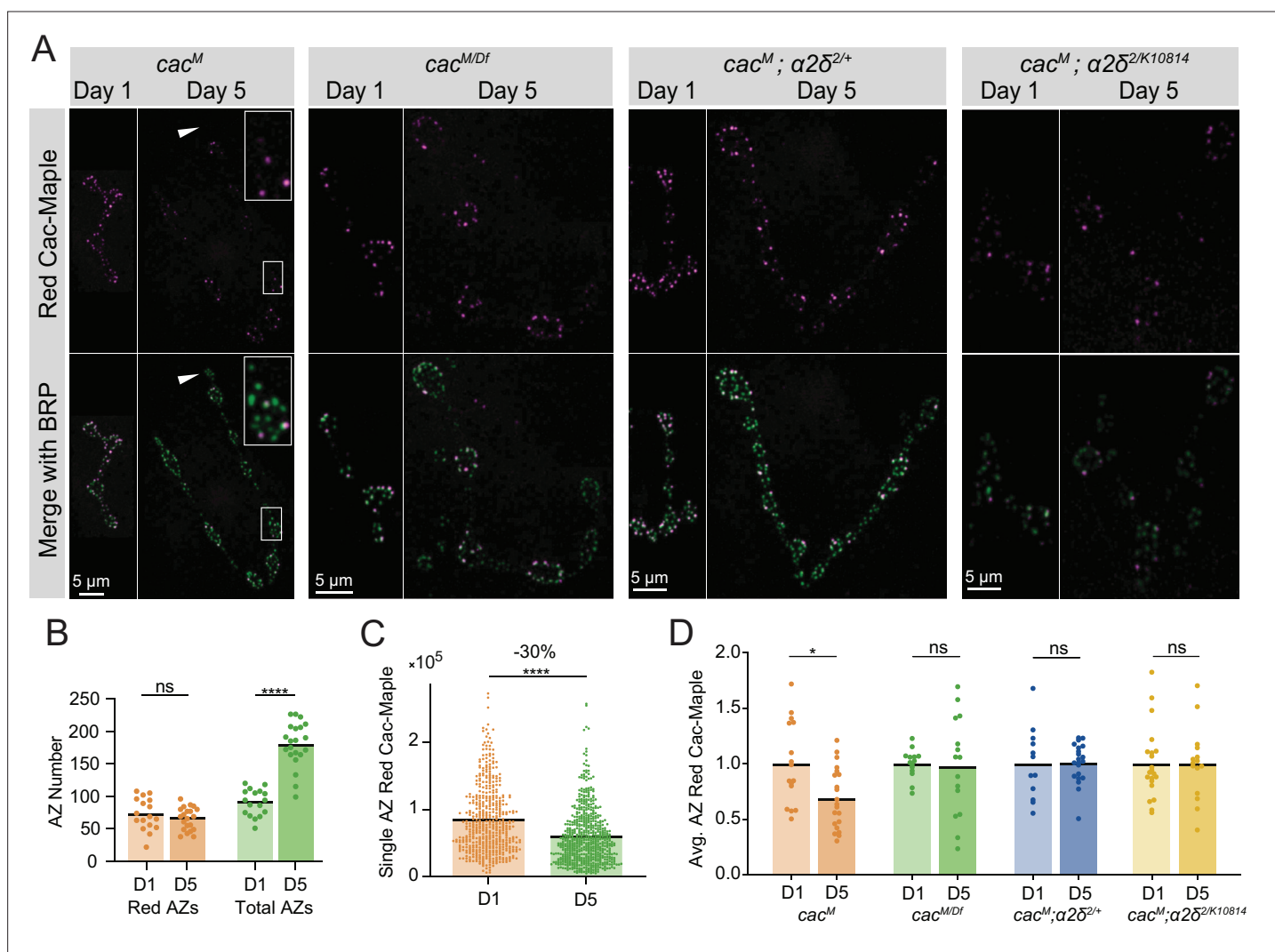


Figure 7. Cac turnover at active zones (AZs) is abolished by reductions in either Cac or $\alpha 2\delta$ expression. **(A)** Representative images of endogenously tagged photoconverted Cac-Maple (magenta) and Bruchpilot (BRP) (green, overlapping with green unconverted Cac-Maple for reliable AZ identification) in controls (*cac^M*), *cac^{M/Df}* heterozygotes, $\alpha 2\delta^{2/+}$ heterozygotes (*cac^M; \alpha 2\delta^{2/+}*), and $\alpha 2\delta^{2/K10814}$ mutants (*cac^M; \alpha 2\delta^{2/K10814}*) at 1 and 5 days after photoconversion. Boutons in white box are enlarged in control panel, and white arrows mark a bouton with no red Cac-Maple fluorescence. **(B)** Number of red-marked AZs (photoconverted Cac-Maple) and total AZs (identified using BRP immunostain) quantified 1 and 5 days post-conversion (red D1: 72.59±5.921, n=17 NMJs; red D5: 65.57±3.789, n=21 NMJs; total D1: 90.65±4.948; total D5: 179.5±7.502, p<0.0001). **(C)** Red Cac-Maple fluorescence at individual AZs (30 brightest AZs per NMJ pooled from 16 to 21 NMJs) at 1 and 5 days post-photoconversion. Percent reduction in brightness at day 5 compared to day 1 is shown above (day 1: 84,672±2258, n=502 AZs; day 5: 59,383±1598, n=630 AZs, p<0.0001). **(D)** Average Cac-Maple fluorescence of the 30 brightest AZs per NMJ at indicated genotypes at 1 and 5 days post-conversion. For each genotype, average Cac-Maple intensity at day 1 was normalized to 1.0 (*Cac^M* D5: 0.6868±0.05975, p=0.0103; *cac^{M/Df}* D5: 0.9746±0.1154; *Cac^M; \alpha 2\delta^{2/+}* D5: 1.006±0.03891; *Cac^M; \alpha 2\delta^{2/K10814}* D5: 1±0.08489).

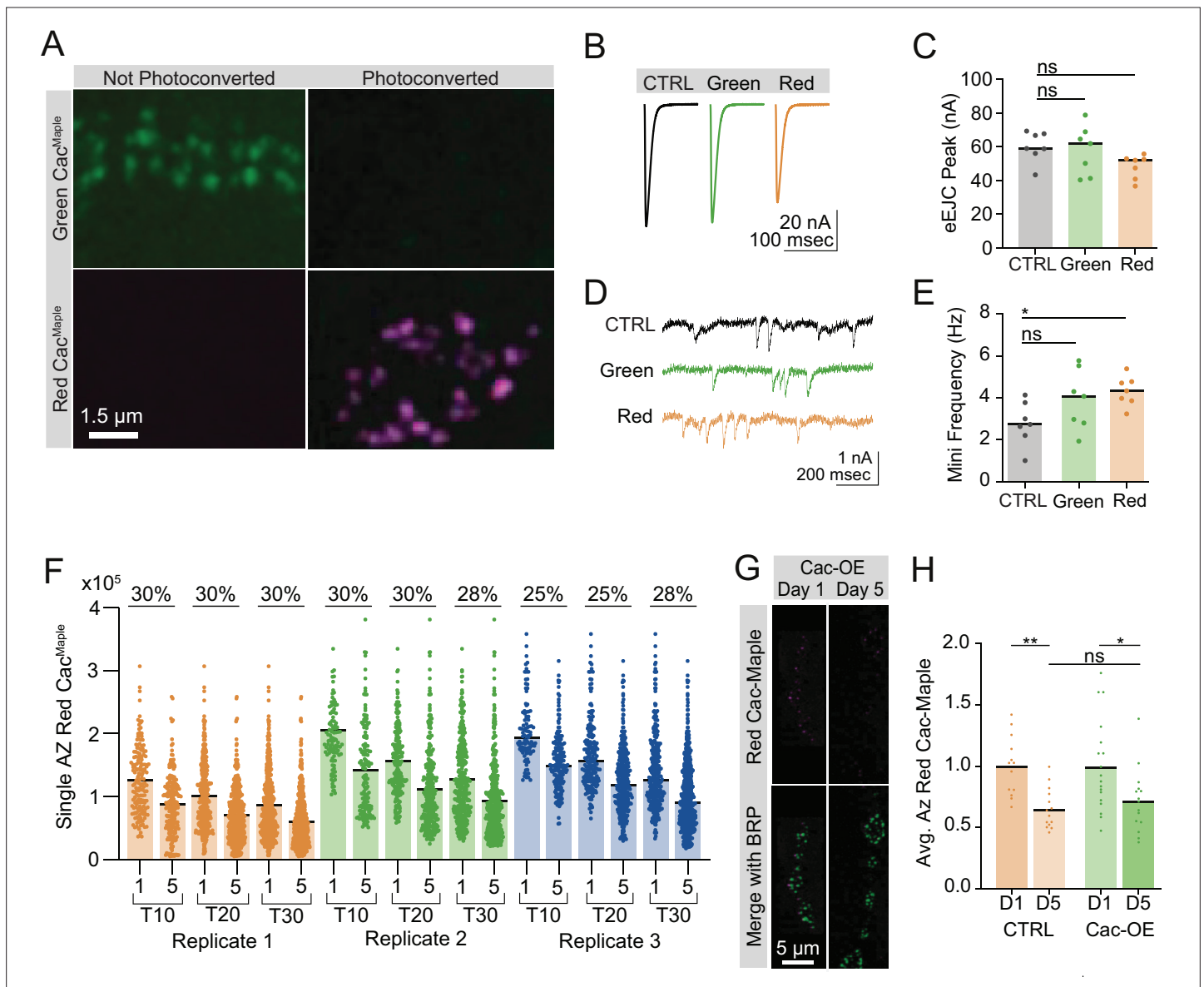


Figure 7—figure supplement 1. Cac-Maple localizes to active zones (AZs), photoconverts fully, and has normal function. **(A)** Representative images of green (unconverted) and red (fully photoconverted, magenta) Cac-Maple at AZs. **(B, C)** Average traces and quantified evoked peak current from control, unconverted Cac-Maple (green), and converted Cac-Maple (red) neuromuscular junctions (NMJs) at muscle 6 (control: 60.21 ± 3.413 , $n=7$ NMJs; Maple [green]: 58.04 ± 5.489 , $n=7$ NMJs; Maple [red]: 48.32 ± 2.674 , $n=7$ NMJs). **(D, E)** Representative traces and quantified mini frequencies (control: 2.781 ± 30.3898 ; Maple [green]: 3.91 ± 0.5409 ; Maple [red]: 4.32 ± 0.2671 , $p=0.0316$). **(F)** Red Cac-Maple fluorescence quantified for three separate experimental replicates at control NMJs on day 1 versus day 5 post-conversion, with three analysis protocols performed for each replicate (top 10 AZs analyzed, top 20 analyzed, and top 30 analyzed). Percent reduction in average red Cac-Maple intensity on day 5 compared to day 1 is shown above for each analysis pair. Replicate 1: (D1 [top 10]: $12,6178 \pm 4049$, $n=170$ AZs; D5 [top 10]: $88,135 \pm 3325$, $n=210$ AZs; D1 [top 20]: $99,885 \pm 2834$, $n=340$ AZs; D5 [top 20]: $69,939 \pm 2076$, $n=420$ AZs; D1 [top 30]: $84,672 \pm 2258$, $n=502$ AZs; D5 [top 30]: $59,383 \pm 1598$, $n=630$ AZs). Replicate 2: (D1 [top 10]: $203,159 \pm 7377$, $n=110$ AZs; D5 [top 10]: $141,260 \pm 5687$, $n=150$ AZs; D1 [top 20]: $15,7051 \pm 4935$, $n=217$ AZs; D5 [top 20]: $110,796 \pm 3637$, $n=300$ AZs; D1 [top 30]: $128,356 \pm 4122$, $n=330$ AZs; D5 [top 30]: $93,117 \pm 2806$, $n=450$ AZs). Replicate 3: (D1 [top 10]: $204,651 \pm 5068$, $n=100$ AZs; D5 [top 10]: $154,834 \pm 3370$, $n=190$ AZs; D1 [top 20]: $165,709 \pm 3918$, $n=200$ AZs; D5 [top 20]: $124,524 \pm 2715$, $n=359$ AZs; D1 [top 30]: $139,113 \pm 3466$, $n=300$ AZs; D5 [top 30]: $99,899 \pm 2261$, $n=570$ AZs). **(G, H)** Representative images and quantifications of red Cac-Maple on day 1 versus day 5 post-conversion in control (*cac^M, C155*) and Cac overexpression (*cac^M, C155; UAS-Cac-GFP*) NMJs ($n=13-18$ NMJs). Bruchpilot (BRP) immunostaining was used to label AZs and red fluorescence in each genotype was normalized to day 1 (*cac^M, C155* D5: 0.6533 ± 0.04386 , $p < 0.01$; *cac^M, C155; UAS-Cac-GFP* D5: 0.07159 ± 0.06665 , $p=0.0152$).

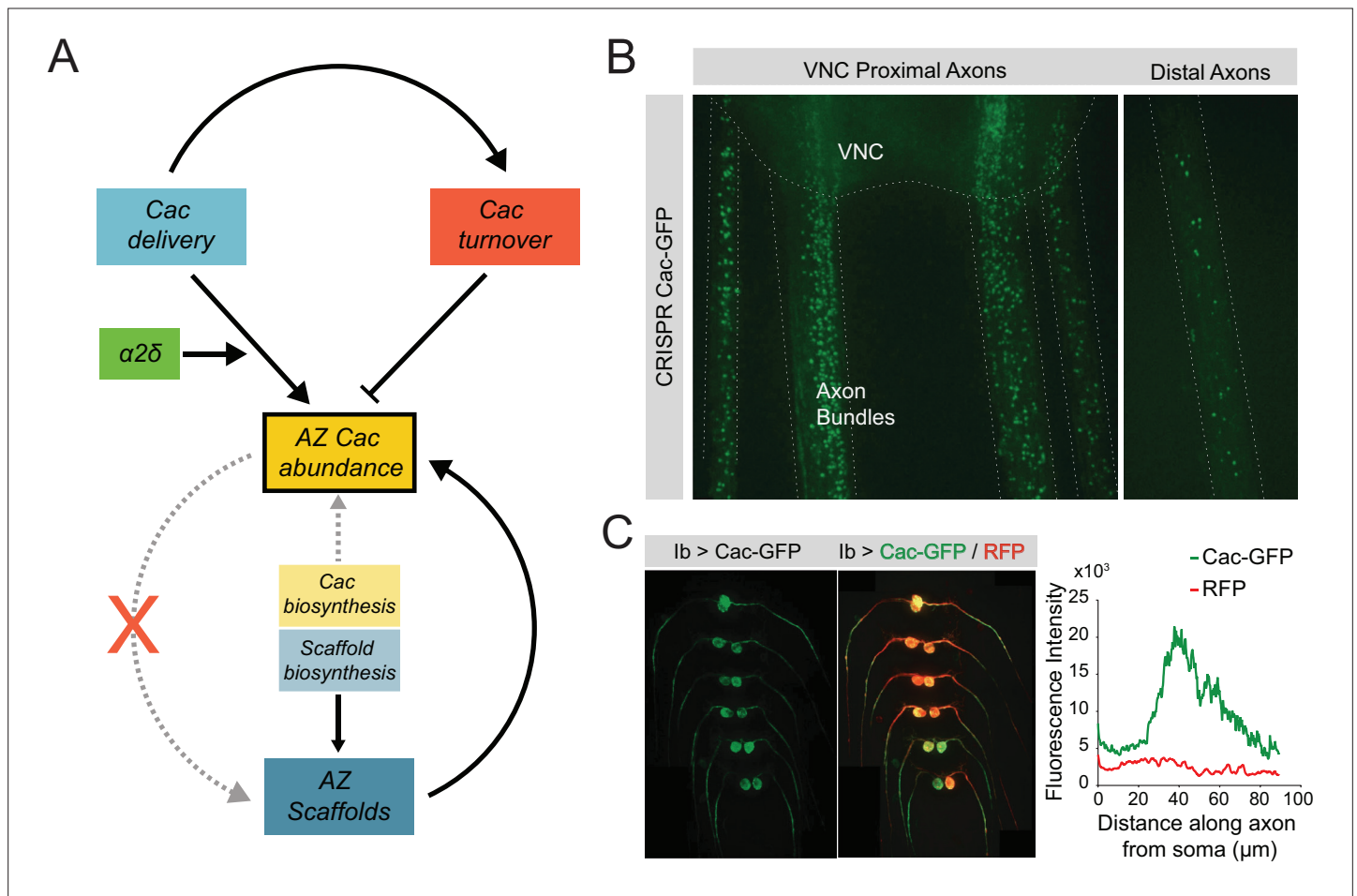


Figure 8. Model of Cac and active zone (AZ) scaffold regulation at the *Drosophila* neuromuscular junction (NMJ). **(A)** AZ Cac abundance (yellow box) is regulated by both new Cac delivery (blue box) and Cac turnover from AZs (red box). Cac delivery is positively regulated by $\alpha 2\delta$, and new delivery promotes turnover of existing channels. Cac biosynthesis (light yellow box) weakly regulates AZ Cac abundance, as AZ abundance is buffered against moderate changes in biosynthesis. In contrast, scaffold biosynthesis is a strong regulator of AZ scaffold abundance. The dependence relationship between AZ Cac abundance and AZ scaffold abundance is unidirectional: AZ scaffolds regulate Cac accumulation, but Cac is dispensable for AZ scaffold formation. **(B)** Left – representative image of endogenously tagged Cac-GFP puncta in axon bundles proximal to the ventral nerve cord (VNC). Right – representative image of Cac-GFP in distal axons. These axon puncta are immobile over a period of 30 min. **(C)** Left – representative image of a VNC with Cac-GFP (green) and RFP (red) expressed exclusively in MN1-Ib neurons. Right – quantification of Cac-GFP and RFP signal intensity as a function of distance along the axon from the soma. Plotted signal intensity was averaged across eight axons. RFP intensity is constant throughout the first 100 μm , while Cac-GFP intensity is elevated in the 30–60 μm range.